Cranfield

College of Aeronautics Report No. 8713
December 1987

TECHNISCHE UNIVERSITEIT DELFT
LUCHTVAART- EN RUIMTEVAARTTECHNIEK
BIBLIOTHEEK
Kluyverweg 1 - 2629 HS DELFT

The Determination of the Aerodynamic Characteristics of an Ogive-cylinder Body in Subsonic, Curved, Incompressible Flow, and an Assessment of the Effect of Flow Curvature

D.I.T.P. Llewelyn-Davies

College of Aeronautics
Cranfield Institute of Technology
Cranfield, Bedford MK43 0AL, England

Cranfield

College of Aeronautics Report No. 8713
December 1987

The Determination of the Aerodynamic Characteristics of an Ogive-cylinder Body in Subsonic, Curved, Incompressible Flow, and an Assessment of the Effect of Flow Curvature

D.I.T.P. Llewelyn-Davies

College of Aeronautics
Cranfield Institute of Technology
Cranfield, Bedford MK43 0AL, England

ISBN 0 947767 90 8

£7.50

SUMMARY

Tests on a 6:1 fineness ratio ogive-cylinder body have been made in the curved flow provided by the CoA Whirling Arm facility. The model size was such that there was a difference in flow direction of 10 degrees between the front and rear of the model. Theoretical estimates were made of the aerodynamic characteristics of the model using the SPARV panel method, and slender-body and linear theory.

The pressure distributions over the model were measured over a pitch range of -6.4 to 11.6 degrees measured relative to the nominal flow direction at the centre of the model. The local loadings and overall loads were then obtained by successive integration of the pressures.

The experimental results showed that unexpectedly high loadings were present over the whole of the afterbody and these dominated the aerodynamic characteristics giving high normal-force and a rearward centre of pressure position as compared with the results obtained from tests made in the straight flow provided by a windtunnel.

The SPARV inviscid-flow solution predicted the loading distributions over the nose reasonably well, but did not predict the high loadings over the afterbody. The effect of small changes in flow curvature and of altering the shape of the base closure were also investigated.

Both slender-body and linear inviscid theory predicted the loading distributions much better. In particular, linear theory closely predicted the experimental loadings when the experimental pitch angles were corrected so that the nose was aligned with the incident flow at the angle predicted by the theories.

CONTENTS

FIGURES

45 Variation of dC_A/dx with x/L. Pitch = 1.0 degrees. Comparison of experiment with theory

46 Variation of dC_A/dx with x/L. Pitch = 3.0 degrees. Comparison of experiment with theory

47 Variation of dC_A/dx with x/L. Pitch = 5.0 degrees. Comparison of experiment with theory

48 Variation of dC_A/dx with x/L. Pitch = 7.0 degrees. Comparison of experiment with theory

49 Variation of dC_A/dx with x/L. Pitch = 8.0 degrees. Comparison of experiment with theory

50 Variation of dC_A/dx with x/L. Pitch = 10.0 degrees. Comparison of experiment with theory

51 Variation of C_N with adjusted pitch angle

52 Variation of C_m with adjusted pitch angle

53 Variation of centre of normal-force with adjusted pitch angle

54 Variation of forebody axial-force with adjusted pitch angle

NOTATION

A	Maximum body cross-sectional area
C_A	Axial-force coefficient $(= -C_x = -X/qA)$
C_m	pitching-moment coefficient (M/qAL)
C_N	normal-force coefficient $(= -C_z = -Z/qA)$
C_p	pressure coefficient $(p-p_\infty/q)$
dC_A/dx	local axial-force loading
dC_N/dx	local normal-force loading
dC_m/dx	local pitching-moment loading
D	maximum body diameter
L	length of model
M	pitching moment on the body measured about the nose
p	local static pressure on the surface of the body
p_∞	free-stream static pressure
q	free-stream dynamic pressure
R	free-stream Reynolds number based on D
T	absolute temperature
T_∞	free-stream temperature
x	distance from nose of model
X	force along the x-axis
Y	force along the y-axis
Z	force along the z-axis
θ	pitch (incidence) angle
ϕ	roll angle
ρ	free-stream density

1.0 INTRODUCTION

When stores are located in close proximity to an aircraft, they may be in a region where the local airflow has considerable nonuniformities. In these conditions it is usual to assume that an uniform flow exists over the store corresponding to that at a particular point on the store (generally the centre of gravity) and using these conditions to estimate the store loads assuming that the variation of the store loads with attitude relative to the mean flow is the same as that in a free uniform stream.

The purpose of the tests reported here is to determine the pressure distribution over an ogive-cylinder body in the curved flow field provided by the CoA Whirling Arm facility, ref 1 and Figs 1 & 2, where the size of the model is such that there is a 10 degree variation in flow direction between the nose and tail of the model. This facility is unique in that it provides the means of doing steady-state testing in a curved flow field. The pressure distributions are integrated to obtain the local loadings over the body and then, by further integration, the overall loads and moments on the body are obtained. The results are then compared with similar data already obtained from testing the same model in uniform straight flow at the same Reynolds number in the CoA 8ft x 6ft low-speed windtunnel, ref 2. Comparisons are also made with theoretical estimates for corresponding conditions.

2.0 EXPERIMENTAL DETAILS

2.1 The model and support

The model tested, Figs 3 & 4, was an ogive-cylinder of overall fineness ratio 6:1 with a nose fineness ratio of 2:1. The maximum diameter ($D_{max.}$) was 9.50 inches (241.3 mm) thus giving an overall length, (L), of 57.00 inches (1447.8 mm) and a nose length of 19.00 inches (482.6 mm).

As the model was subjected to radial accelerations of up to 6g when being tested in the Whirling Arm, it was important to keep the weight as low as possible to minimise the deflection of the sting support, ref 1, as it was difficult to measure the angular deflection accurately when the model was rotating as the deflection was in the horizontal plane. The model was designed accordingly as a relatively thin balsa-wood shell which, except for a short hardwood nose cone, was split longitudinally to facilitate the installation of the pressure plotting tubes and allow easy access to the instrumentation, Fig 4. In order to obtain a detailed pressure distribution over the body, it was decided to incorporate a large number of pressure tappings along a body generator and then rotate the body about its axis to obtain the pressure distribution along the generator at a number of roll angles relative to the datum position.

The model was pressure plotted along two generators 180 degrees apart which were at 90 degrees to the splitline so as to minimise any errors due to any flow disturbances coming from any discontinuities etc. at the split lines which were sealed by thin plastic tape. The generator on the main part of the body was pressure plotted at intervals of 0.02L from 0.01L to 0.99L. The opposite generator had pressure tappings at 0.1L intervals from 0.01L to 0.91L together with additional tappings at 0.33L, 0.335L, 0.34L and 0.345L. In order to achieve an acceptable standard of pressure hole, narrow strips of a light hardwood, gelutong, were incorporated into the balsa-wood shell

along the pressure plotting generators (and also the split lines). The primary purpose of this auxiliary line of pressure tappings was to counterbalance the weight of the main pressure plotting generator to minimise the torque needed to rotate the model when the arm was rotating. However the pressure data from these holes would be available for checking purposes and also to determine whether any separations were present at the beginning of the parallel afterbody as a result of the discontinuity in curvature at the junction of the ogive and cylinder.

The nose cone ended at 0.02L from the nose and therefore already incorporated the pressure points at 0.01L on both the main and auxiliary lines of holes. By incorporating two additional holes at 90 degrees to these together with a pitot hole at the apex, the nose cone became a 5-hole yawmeter that could be used to determine the approach speed and the alignment of the model to the incident flow.

The model was mounted on its support sting by two needle-roller bearings and was rotated about its axis by a high torque rotary solenoid stepper drive mounted on the sting inside the model and rotating the model by means of a 6:1 stepdown toothed belt drive, Fig 4. As the rotary solenoid rotated through 15 degrees each time it was energised, the model could be rotated in 2.5 degree steps. A rotary solenoid drive was chosen in preference to the more usual stepper motor because the torque required was larger than that provided by the available stepper motors without excessive gearing-down and, even so, the weight of the stepper motor was considerably greater than that of the rotary solenoid, this being of importance as usual to minimise deflections of the model under the 6g operating conditions. This system replaced the rotary-solenoid/gearbox system that had failed in the previous tests in the CoA 8ft x 6ft lowspeed wind tunnel, ref 2.

The model was mounted on a parallel support sting of 3.00 inches (76.2 mm) diameter (d), so that the mid point of the model was at the virtual centre of rotation of the model-support linkage which was at a radial distance of 327 inches (8306 mm) from the centre of

rotation of the arm. The centre of rotation of the model was 58.5 inches (1486 mm) in front of the leading edge of the fairing over the pitch-change linkage, Fig1. Thus the ratio of sting diameter/maximum body diameter (d/D_{max}) was 0.316 and the distance between the base of the model and the leading edge of the fairing was 30.0 inches (762 mm) or 3.16 D_{max}.

The model and support system are described in more detail in references 1 and 2.

2.2 Transition fixing

As the Reynolds number of the tests was only 330,000 based on body diameter (1,980,000 based on body length), it was decided to ensure turbulent flow over the model by fixing transition by a band of roughness 0.1 inch (2.5 mm) wide located 1.00 inches (25.4 mm) behind the nose of the model. This meant that the four yawmeter holes were in natural flow (probably laminar). As in the tests in the CoA lowspeed windtunnel, the roughness consisted of a sparse distribution of spherical glass balls (ballottini) of 0.023 inches (0.06 mm) mean diameter which gave a roughness Reynolds number of 800 under test conditions as recommended by Braslow, reference 3.

2.3 Instrumentation

The individual pressure taps in the model were connected by short lengths of plastic tubing to two 48 port "D" type Scanivalve pressure switches mounted symmetrically inside the model, Fig 4. The pressures were then measured by Setra +/- 0.1 psi differential pressure transducers.

The static pressure in the test chamber was obtained from a standard pitot-static head mounted at the test radius. 327 inches (8306 mm) from the fairing at the end of the arm remote from the model-support system, (Fig 1 and ref 1). This static pressure source was also

used as a reference pressure for the Setra transducers mounted in the pressure switches and, in addition, were connected to the first port of each pressure switch so as to provide a zero-error reading for each transducer at the beginning of each scan.

The test was controlled and the data was collected by a Sirton "MIDAS" microcomputer mounted on the arm, ref 1. As the computer rotated with the arm, it was considered inadvisable for it to have components sensitive to vibration or centrifugal force and so the MIDAS did not include a visual display unit (VDU) or disc drives. The MIDAS controlled the test by means of a program in the XYBasic language developed on a "Superbrain" microcomputer and transferred to it via a link through the sliprings on the Whirling Arm. When the Whirling Arm was operating at the correct speed, the program was initiated via the link and proceeded to scan the ports in turn before rolling the model through 10 degrees and repeating the procedure until the range 0 to 360 degrees of roll had been covered. Besides the two Scanivalve transducer readings, the MIDAS also recorded the dynamic pressure as obtained from the pitot-static probe and measured by the Celesco +/-50 mm transducer. Hence it was possible to work out the fully corrected pressure coefficient, C_p, at each port as the test proceeded. These Cp values were displayed on the VDU of the Superbrain computer as the test proceeded so as to check the progress of the test and the serviceability of the instrumentation. The test could be interrupted, if required, at the conclusion of any scan of the pressures. Both the raw data and the computed C_p values were stored in array form in the solid state memory of the MIDAS as the test proceeded, to be transferred by the Linkcom file transfer package to the Superbrain when the test was completed and the arm was at rest. As the XYBasic system stored the array data in a parallel format that was the inverse of that used by the Superbrain MBasic interpreter for the initial analysis of results, a format conversion program was written which not only did the required conversion, but also produced the data in serial format suitable for transmission to the CoA VAX 750 computer for the final analysis and plotting of results.

3.0 TEST PROGRAMME

The test programme proposed consisted of measuring the pressure distribution over the body in 2 degree intervals of pitch over the range -4 to 14 degrees relative to the datum direction, this being when the axis of the model was tangential to the radius to the centre of the model. In addition the model was tested at an angle of 5 degrees when the nose of the model should be aligned with the oncoming flow. The pitch angle was defined as positive when the nose of the model had moved towards the centre of the arm, Fig 6. The asymmetric range was chosen to be representative of the practical case where an aircraft has to fly at a considerable incidence in order to produce the necessary forces to enable it to fly in the curved path.

The pressure distributions were determined over the whole body were determined by rotating the main pressure plotted generator through 360 degrees in 10 degree intervals from the roll datum position. This was when the generator was in the plane of rotation of the arm (horizontal) with the holes facing the centre of the arm. The direction of rotation was clockwise when viewed from the rear.

In addition to the main tests, a small number of additional tests were made to determine the accuracy of pressure measurement and the determination of the best means of determining the approach speed of the model to the air in the test chamber. The results of the tests are reported in ref 1.

Although this test programme is relatively modest and would normally be completed in about a week in a lowspeed windtunnel, the programme fully occupied the Whirling Arm for a considerably longer period due mainly to the unexpected effects of centrifugal force on the items of equipment located in the model where they were subjected to centrifugal accelerations of 6g. The occurrence of the faults and the cure is reported in ref 1.

4.0 TEST TECHNIQUES AND ACCURACY OF MEASUREMENT

Testing in the Whirling arm presents additional problems to those encountered in testing in a normal windtunnel. These are due to three main reasons:-

a) The difficulty of measuring angles in the horizontal plane

As the plane of rotation, and therefore the main test plane, is horizontal, the model pitch has to be measured in this plane. Unfortunately there is no simple device, such as a spirit level, that can be used to set or measure the model attitude in this plane either when the arm is at rest or when it is rotating. Thus these angular settings have to be determined by measurement and/or calculation which is both more difficult and less accurate than measurements in the vertical plane made relative to gravity.

b) Centrifugal effects

As the required test conditions are obtained by rotating the arm, the arm structure and all items on it are subjected to accelerations up to 6g. Not only may this cause problems with the operation of mechanical devices, but the centrifugal loads cause the model and its support system to deflect.

For normal aerodynamic tests, the generally accepted standard of accuracy for angular measurement is 0.1 degree and thus comparable accuracy should be achieved in the Whirling Arm. Where the centrifugal forces act along the axis of a structural member, the resultant tension or compression stress is small resulting in negligible deflection of the structure. However when the centrifugal loads act normally to the major axis of a long component such as the model support sting and carrier beam or the pitch-control beam, Fig 5, then the angular deflections of these members, although small, are significant in relation to the required accuracy.

In measuring the forces and moments acting on a model by means of strain gauge balances etc the tare loads in the vertical plane due to the weight of the model etc do not alter and therefore can be zeroed-out as in a wind tunnel. In the horizontal plane however, although any tare load can be zeroed-out when the arm is at rest, this

tare load will change due to the effects of centrifugal acceleration as the speed of rotation alters. Thus at the normal operating speed, the tare loads are large and may be significantly larger the the aerodynamic quantities, leading to reduced accuracy of measurement unless some means of reducing or counterbalancing the tare loads can be found.

In measuring pressures, the centrifugal accelerations also cause problems in that corrections have to be applied for its effect on the mass of air in the pressure leads connecting the pressure tappings to the measuring transducers, this correction varying not only with the speed of rotation of the arm, but also with the radial distance of the pressure tapping. In addition the centrifugal force may have an effect on the zero reading of the pressure transducers.

c) Effect of swirl

When the Whirling Arm is rotating there is a transfer of energy from the aerodynamic drag of the rotating parts to the mass of air in the test chamber causing it to rotate in the same sense as the arm, thus reducing the approach speed of the air to the model. As it is easiest to use the speed of rotation as the primary variable in tests because it is both easy to set accurately and varies little with time, the approach speed must be known for that particular test condition in order to non-dimensionalise the measurements into the normal aerodynamic coefficients. In addition, as both pressures and forces vary as (approach speed)^2 and the corrections vary as (rotational speed)^2, it is necessary not only to know the approach speed, but also to ensure that it is as close to the rotational speed as possible so as to maximise the quantities being measured at that particular rotational speed.

Another disadvantage of swirl is that the mechanics of energy transfer to the air in the test chamber and the partial absorption of this energy by porous screens has resulted in the swirl flow being essentially a confused eddying flow which not only made measurements of its magnitude difficult, but also presented additional uncertainties in determining the attitude of the model to the incident flow as this cannot be assumed to be accurately circumferential.

4.1 Measurement of pitch in the horizontal plane

The location of the centre of rotation of the model support system was determined by the location of the centre of rotation of the control beam and the geometry of the system. Thus once the model support system was installed, no means was available of altering the virtual centre of rotation. The datum pitch angle was defined to be when the sting centreline was perpendicular to the radius through the virtual centre. This was set by stretching a string between the centre of rotation of the arm and the virtual centre of rotation on a parallel sting and using a large, accurate set-square to set the datum position. In addition a check was made by positioning a dial gauge against the sting at the virtual centre and then moving the arm by a fixed distance in either direction. If the sting was tangential to the radius, then the variation of the dial gauge reading would be the same in both directions. By this means the datum position of the sting was estimated to be tangential to within less than 0.1 degree.

The pitch angle relative to the datum position was measured by a linear potentiometer attached to the control beam near its pivot point and to a beam which ran between the inboard diagonal bracing on the side of the arm. Initially the limits of travel were set to +/- 10 degrees as the support system fouled the internal structure of the fairing, but for the latter part of the tests the obstruction was removed and the pitch range was increased to -15 → +14 degrees. The potentiometer output was calibrated by setting the sting to a series of pitch angles determined by measuring the sting displacement from the datum position along the leading edge of the fairing, the displacement for a given pitch angle having been calculated from the geometry of the system. The discrimination of the measuring system was approximately +/- 0.03 degrees, but as the control of the pitch-changing jack was relatively coarse under some conditions, it took a little time to obtain the required setting within the above discrimination.

When the arm is rotating, further corrections have to be applied to allow for the deflection of the control beam, the sting carrier beam and the sting itself. These corrections are discussed later.

4.2 Pressure measurement

The accuracy of pressure measurement in the Whirling Arm can be considered in three parts. Firstly the basic discrimination of the transducer/signal conditioning equipment. Secondly the corrections that have to be applied due to the centrifugal accelerations that are present when the arm is rotating. Thirdly the experimental scatter that occurs due to flow unsteadiness etc when the arm is rotating.

4.2.1 Basic discrimination

The discrimination of the pressure measurements depends on the magnitude of the output of the pressure transducers and the voltage discrimination of the analogue/digital converter (ADC) used. At the normal operating speed of the arm (c 25.5 rpm) the maximum pressure that has to be measured is the dynamic head (q) which, due to swirl cannot exceed 30 mm H_2O. Using the static pressure as the reference pressure, the Setra transducers will therefore give a maximum output of approximately 1.2 V. As the operating range of the ADC is +/- 10 V, ref 1, an additional amplifier is required to increase the transducer output to match. The ADC has a full-range discrimination of 4096 counts, thus the discrimination of the system is approximately 0.0146 mm H_2O.

The Celesco transducer used for measuring the dynamic head present at the pitot-static probe has a basic output of +/- 10V for pressure differences of +/- 50 mm H_2O and therefore has a discrimination of 0.0224 mm H_2O.

If it is assumed that the dynamic head to be measured is approximately 24 mm H_2O due to the presence of swirl, then the

pressure coefficients measured will have a basic discrimination of approximately $C_{p_1} = 0.00058$.

4.2.2. Effects of centrifugal force on pressure measurement

Centrifugal accelerations affect the pressure transducers in two ways. Firstly, the transducer diaphragms, although small, thin and light, have a finite mass and so deflect when subjected to centrifugal acceleration and this deflection is seen as a zero-drift. High accuracy transducers are designed as far as possible to ensure that the zero-drift due to acceleration is small. This effect can be eliminated by keeping the plane of the diaphragm in the plane of the acceleration, but where the transducer is mounted in a model which can be pitched, this is not possible under all test conditions. In the case of the Setra transducers mounted in the pressure switches, the zero-drift due to centrifugal acceleration was also eliminated by the method previously described to eliminate transducer temperature drift, (section 2.3).

This means of zero correction could not be applied to the Celesco pressure transducer that measured q. However this transducer was mounted on the instrumentation platform near the central tower where the centrifugal acceleration was only about 1g. Experience at the School of Aviation Medicine, Farnborough, had indicated that these transducers were almost insensitive to centrifugal accelerations, and as a rapid check showed that rotating the plane of the diaphragm of the transducer from vertical to horizontal caused only a small difference in reading which was negligible in comparison with that normally occurred when measuring q, no corrections for centrifugal accelerations were applied. It was found that, provided a ½ hour warming-up period was allowed before a run, the transducer drift was also negligible compared with the dynamic pressure output over the 1½ → 2hour period of the test. In fact, even with the deliberately large pneumatic damping inserted in the pressure leads, the unsteadiness of the transducer readings due to the unsteadiness in the approach flow to the pitot-static probe, (ref 1),

was many times greater than the errors to be expected from the combined effects of centrifugal acceleration and temperature drift.

The second effect of centrifugal acceleration on the measurement of pressure is due to the mass of air in the pressure leads.

The centrifugal force on a small element of air of length dr in a tube of cross-sectional area A at a distance of r from the centre of rotation is

$$\rho A dr * \Omega^2 r$$

where Ω is the rotational speed of the arm

ρ is the density of air

Thus, if the tube connects two points at radii of R_1 and R_2, there is a pressure difference between these two points due to centrifugal force of

$$\int_{R_1}^{R_2} \rho \Omega^2 r dr$$

$$\text{or } \tfrac{1}{2}\rho(R_2^2 - R_1^2)\Omega^2$$

$$\text{or } \tfrac{1}{2}\rho(V_2^2 - V_1^2)$$

where V_2 and V_1 are the translational speed (or "speed over the ground") at the two radii.

Thus if the pressures at two points at different radii are to be compared by using a differential transducer, a correction has to be applied to the measurement to allow for the centrifugal force on the air in the pressure tubes. It should be pointed out that the correction depends solely on the radii of the actual pressure tappings and is completely independent of the radial position of the transducer as the additional correction is the same for both connecting tubes. The correction depends only on the geometry of the system and thus can be accurately calculated.

For the present ogive-cylinder model the maximum radius is 4.75 inches (120.7 mm) and so at a rotational speed of 25.45 rpm with the centre of the section at the datum radius of 327 inches (8306 mm), the correction between one side of the body and the other is approximately 0.18 mm H_2O which is equivalent to $C_{p_0} \simeq 0.070$ with a swirl of 8.9%. When the model is pitched 10 degrees about its midpoint, the centre of rotation, the radial distance of the nose, or centre of the base, alters by 4.98 inches (127 mm) giving a correction of $C_{p_0} = 0.037$.

4.2.3 Experimental scatter

Under actual test conditions, the repeatability and accuracy of measurement may be appreciably worse than the ideal values discussed above due to a variety of causes such as unsteady flow, vibration and electrical noise. In order to get an indication of the repeatability of the pressure measurements, a normal test run was made without rotating the model. Thus each pressure tapping was sampled 37 times and each sample was the mean of 25 individual readings taken at a rate of about 200 Hz. These results are discussed in detail in reference 1 and the main points are summarised below:-

a) The standard deviation of the readings varies with the magnitude of the pressure measured and can be expressed in the form

$$\Delta C_{p_0} = 0.0025 + 0.0166|C_{p_0}|$$

b) The increasing error with increase in C_{p_0} was shown to be dependent primarily on the forward inclination of the body surface relative to the oncoming flow at the pressure hole.

c) The maximum scatter is about three times the value of the standard deviation.

The minimum standard deviation was therefore some four times the discrimination of the pressure measuring system.

Static tests were made with one side of the transducer vented to atmospheric pressure and the other side sucked-down so that the pressure difference across the diaphragm was approximately 24 mm H_2O. These showed that the readings as sampled by the recording system were unsteady and had a standard deviation of 0.08 mm H_2O for sample sizes of 25. This standard deviation translates into a standard deviation of C_p = 0.0025 which is the constant in the equation in a) above. It would therefore appear that the maximum accuracy of measurement is controlled by electrical noise and interference in the recording system rather than aerodynamic unsteadiness.

A similar test done using the Celesco transducer showed that the output of the transducer was also unsteady, but the measurement showed only half the standard deviation of the Setra transducers even though its sensitivity was only about half that of the Setras.

When the gain of the instrumentation amplifier in the multiplexed ADC board was set using a precision DC source, the output of the ADC was steady and could be easily set to 1 count (in 4096) and did not vary by more than one count over a considerable period. It would thus appear than the Setra transducer/amplifier system were the source of the basic unsteadiness in the pressure readings.

5.0 EXPERIMENTAL RESULTS

As the model was the first to be tested in the Whirling Arm after it had been redesigned, some initial analysis was necessary to determine the direction of the approach flow, its magnitude and whether varying the pitch angle altered these quantities.

5.1 Determination of the inclination of the model to the oncoming flow

5.1.1 Measurements in the horizontal (pitch) plane

The pitch angle of the model was set by the pitch potentiometer reading once the arm was at the test speed. This was done because it was known that there was an alteration in the apparent angle as the arm was run up to speed. As the potentiometer reading returned to its original value when the arm returned to rest, it was thought that this movement was due to air trapped in the hydraulic system being compressed when the centrifugal loads were applied to the double-acting jack and thus allowing the jack to lengthen under load. However after the tests were completed, it was found that the apparent movement was due to the distortion of the structure supporting the the control beam pivot and the potentiometer. Although it was known that the deflection was about 0.6 degrees in the initial case and 1.2 degrees when the pitch travel was increased, these values were obtained from readings on another model which differed appreciably in weight and configuration from the present model and so were not necessarily representative. It was therefore necessary to obtain a correlation between the attitude of the model to the oncoming airflow and the attitude indicated by the pitch potentiometer.

As the variation of static pressure reading with flow indication had been obtained for all four static holes at 0.1L from the tests in tests in the CoA 8ft x 6ft lowspeed windtunnel, see ref 2, four measurements of the direction of the oncoming flow could be obtained at

each pitch angle tested by analysis of the pressure readings at roll angles of 0, 90, 180, 270 and 360 degrees. The means of the values at each "set" pitch angle are plotted against the "set" angle in Fig 7. Although there is some scatter in the results, it can be seen that the data lie along two parallel lines corresponding to the two pitch range conditions and the 45 degree slope of the lines indicates that there is a direct 1:1 correspondence between the "set" incidence and that of the oncoming flow, with the nose aligned to the oncoming flow at a "set" pitch angle of 7.4 degrees in the initial tests with the restricted pitch range and 8.4 degrees in the later tests with the extended pitch range. The difference between the test series, (1.0 degrees), is rather greater than that obtained in the tests previously referred to. It should be noted that the 5 degree setting was done with the "full range" travel and gives almost exactly the same inclination as the 4 degree setting done in the "restricted travel" condition, thus confirming directly the difference in indicated angle between the two cases. Unfortunately this meant repeated rather than additional data.

Knowing the centre of gravity position and weight of the sting and the model with its instrumentation and the inside and outside diameters of the sting, the loads on the sting, sting carrier beam and control beam can be calculated for the test speed and hence the angular and linear deflections of the model can be calculated as described in ref 1.

The results at the datum pitch angle are as follows:-

Control beam

1) Angular displacement at pivot point = 0.093 degrees
2) Displacement of front support pivot = 0.041 inches (1 mm)
3) Displacement of rear support pivot = -0.031 inches(-0.8 mm)
4) Angular deflection of sting carrier = -0.031 degrees

Sting deflections relative to sting clamps

5) Outward deflection of centre of model = 0.229 inches (5.8 mm)
6) Outward angular deflection at model = 0.172 degrees

Sting carrier beam

7) Angular deflection of sting clamps = 0.116 degrees

Thus the total angular deflection due to the deflection of the model, sting, sting carrier beam and control beam is 0.41 degrees. As the maximum lift from the body is very small, about 1 lb (0.5 kg), the extra loads applied to the control beam as the structure moves in and out are due entirely to the centrifugal loads on the moving components. These have been calculated throughout the extended pitch range and do not vary from the design case by more than 10%.

When the model yawmeter nose is aligned with the oncoming flow, the "set" incidence should be 5.00 degrees. The deflection of the support structure has been shown to be about 0.4 degrees so there is approximately 2.0 degrees to be accounted for in the "restricted travel" case and 3.0 degrees in the "full travel" case. The unaccounted amount is the sum of the inflow or outflow of the oncoming stream and the deflection of the potentiometer mounting, both of which are unknown. As previously noted, for a different model the deflection in the "full travel" case was double the "restricted travel" case when accelerating from rest to the test speed. If it is assumed that a similar relationship applies for the present model, then the apparent outflow angle (1 degree) is the same in both cases as would be expected. Thus

the actual geometric pitch angles tested are -6.4, -4.4, -2.4, 2.6, 4.6, 6.6, 8.6, 9.6 and 11.6 degrees. The nominal +2 degrees pitch case has been omitted because the readings of one transducer were found to be erratic. The cause probably being the incipient failure of one of the tabs in a connector which failed completely at the beginning of the next test.

5.1.2 Measurements in the vertical plane

The axis of the model had been set, using its built-in spirit level, so that it was horizontal. The yawmeter measurements were analysed to determine the direction of the oncoming flow in the vertical plane. The accuracy of measurement is not very high because the standard deviation of the yawmeter pressure readings is high due to the high surface slope as explained previously. An error in the differential pressure between opposite holes equal to the expected standard deviation, C_p = 0.01, results in an error in flow direction of about 1/4 degree. As isolated readings may be in error by up to three times the standard deviation, even by averaging the four values of the flow direction in each plane obtainable at each pitch angle, it is unlikely that accuracies of better than +/- 1/4 degree are obtainable. After critical examination of the available data, it was concluded that the mean yaw of the oncoming flow was zero to within about +/- 1/4 degree.

5.2 Linear displacement of the model.

The displacement of the model from the datum radius comes from two sources, first the bending of the model support system under centrifugal loads, and secondly the geometric changes that occur with pitch changes as the model does not rotate about the nominal virtual centre.

The main contributions to the displacement of the model due to centrifugal loads come from the bending of the support sting (0.23 inches (5.8 mm)), and the angular displacement of the sting

carrier beam between the sting clamps (0.116 degrees) which results in a further 0.11 inches (3.4 mm) deflection at the model.

As the pitch angle is altered, the centre of the model moves backwards and inwards or outwards depending on the direction of pitching. Although the tangential movement is large, up to 3.3 inches (84 mm), the radial movement is quite small. up to +/- 0.60 inches (15 mm). In addition there is an inwards movement of up to 0.09 inches (2.3 mm) due to the foreshortening of the parallelogram linkage as the pitch angle is changed.

Thus, at operating speed, the model deflects outwards a distance of 0.35 inches +/- 0.6 inches (9mm +/- 15mm) depending on the pitch angle. As the change in radius at the centre of the model with pitch is only about 5% of that occurring at the extremes of the model, the variation of radius of the model centre with pitch has been ignored.

As the pressure corrections due to centrifugal force depend solely on the radial position of the centre of the model and the actual angular position of the model, these corrections can now be determined for the range of conditions tested.

5.3 Determination of the variation of swirl with pitch angle

In order to calculate the correction for the effect of centrifugal acceleration on the pressures measured in terms of C_p, it is necessary to know the appropriate approach speed to the model. As it has been determined previously that the use of a mean value of the approach speed instead of the instantaneous value had little effect on the accuracy of the measurements, this mean value was obtained for each pitch angle by averaging all 1369 measurements of the approach speed obtained, and then determining the mean swirl. The variation of swirl with pitch angle of the model is shown in Fig 8. From the graph it can be seen that although the swirl remains constant up to about 2 degrees pitch, it then drops rapidly by nearly 2% before partially recovering

and then decreasing slightly with further increase in pitch. This behaviour is somewhat unexpected in that, as the lift on the model is very small at all attitudes, the changes in drag and therefore the energy transmitted to the air stream would not vary greatly. Thus it would not be anticipated that there would be any significant changes in swirl throughout the test range. However some significant change of flow must take place in order to reduce the swirl as observed and it must depend critically on the attitude of the model and its support. The most likely causes were considered to be flow break-aways either over the outer fairing of the model support linkage or in the junction between the inner and outer fairings. Unfortunately time was not available to investigate the matter further

5.4 Experimental determination of the loadings

Using the corrected pressures, the pressure distributions at each longitudinal section were integrated numerically to obtain the local loadings.

5.4.1 Normal-force and pitching moment loadings

The variation of the normal-force loading, dC_N/dx, and the pitching moment loading, dC_m/dx, with axial position and pitch angle is shown in Figs 9 & 10.

Fig 9 shows that there is a considerable normal-force loading over the whole of the parallel afterbody. At a given pitch angle the loading is almost constant between x/L = 0.4 and 0.9 but then increases over the last 10% of the body. The loading between x/L = 0.4 and 0.9 becomes more positive as the pitch angle increases varying from dC_N/dx = 0.2 at -6.4 degrees pitch to 0.35 at 11.6 degrees pitch. The variations have been drawn as smooth curves for this analysis, but in some cases the data has considerable scatter. This is seems to be due to alternate points being derived from different transducers. Each set of data from one transducer generally lies on a smooth curve, but in some

cases the two curves are displaced even though the transducer zero error was eliminated for each set of data. The change in reading was therefore possibly due to an occasional change in the calibration in no.2 transducer (i.e. stations 3, 7, 11% etc) as experience had shown that this transducer occasionally became erratic after several hours of operation although it returned to normal if it was switched off for an hour or so.

The forebody loading distribution shows the usual well-defined peak, but between pitch angles of 2.6 and 6.6 degrees, where the forebody loading changes from being completely negative to being completely positive, the general shape of the distribution alters as the location of the peak loading moves rapidly towards the nose before moving aft to slightly behind the low-attitude position.

When the maximum value of dC_N/dx for each pitch angle (θ) is plotted against pitch angle (Fig 11) it is found that the variation can be represented by two parallel straight lines for $-6<\theta<4$ and $6<\theta<12$ which are considerably displaced. Unfortunately there is less data in the transition region than was intended because of the unexpected structural distortions affecting the pitch indicator measurements. Although the variation in this region is not expected to be linear owing to the irregular movement of the position of the forebody peak loading , the large displacement between the two straight lines was somewhat unexpected. If however the variation of the position of the peak loading is examined in more detail, Fig 12, it is seen that for $\theta > 6.6$ degrees the position of the peak loading is constant at $x/L = 0.19$ while at $\theta < 4.6$ degrees the position of the peak loading is again constant but is considerably nearer the nose at $x/L = 0.11$. When the value of the normal-force loading at $x/L = 0.01$ is plotted against pitch angle, Fig 13, it is seen that the data lie on a straight line except for the point at $\theta = 11.6$ degrees. This was to be expected as this is another form of yawmeter calibration which should be linear in the region where the body is nearly aligned with the oncoming flow.

As the slope of the loading at the nose varies directly with the pitch angle, the separation between the two straight lines representing the variation of $(dC_N/dx)_{max}$ with θ as previously described is explained by the further aft position of the peak loading at the higher pitch angles, although the reason for the farther aft position has yet to be explained.

Fig 13 also shows that the loading at x/L = 0.01 is zero at an angle of 6.0 degrees which confirms that the approach flow to the model is inclined outwards by 1.0 degrees as was previously deduced in Section 5.1.1.

The variation of the pitching moment loading distribution with pitch angle is shown in Fig 10. As the moments are measured about the nose, the large afterbody loadings dominate the graphs, but as the moments are derived directly from the normal-force loadings, the curves do not show any unexpected features.

5.4.2 Axial-force loadings

The pressure distributions have also been analysed to measure the axial pressure drag of the body to which only the forebody contributes as the afterbody is parallel. The results are presented in Fig 14. From this it can be seen that there is a positive loading over the front part of the forebody whilst the rear part has negative loadings.

At the lowest pitch angle the shape of the positive part of the loading curve is almost triangular, but as pitch increases, not only does the maximum value of the loading increase but its peak becomes more rounded and eventually flatter. In addition the position of maximum loading moves aft with the resultant movement aft of the position of zero loading.

At the lowest pitch angle, the shape of the negative part of the curve is almost sinusoidal, but has a distinct kink in it at about x/L = 0.25. The area under the negative part of the curve is considerably greater than that under the positive part of the curve.

As the pitch increases the negative part of the curve becomes smaller, the peak flattens and the shape of the curve eventually becomes almost trapezoidal due to the spread if the kink previously mentioned. The position of the negative peak also moves aft with increase in pitch.

These changes are summarised in Figs 15 & 16 which show the variation of the maximum and minimum values of the axial loading with pitch angle and also the variation with pitch of the axial positions of the peaks and the position of zero loading. The curves indicate a smooth variation with pitch of the various quantities with the exception of the variation of $(dC_A/dx)_{max}$. This varies almost linearly with pitch up to an angle of 6.6 degrees at which angle the loading suddenly decreases, but, as pitch increases farther, the loading begins to increase again at approximately the same rate as the initial part of the curve. Examination of the load distributions, Fig 13, shows that this is the region where the shape of the positive peak of the loading curve is changing rapidly to become flatter.

The position of the maximum, minimum and zero axial loading move rearwards with increasing pitch, Fig 16, the range of movement being as follows, the maximum loading from x/L = 0.03 to 0.075, zero loading from x/L = 0.10 to 0.175 and the minimum loading from x/L = 0.20 to 0.24. However while the positions of the zero and maximum loadings move back linearly with increase in pitch, the position of the minimum loading is the same at high and low pitch angles (at x/L = 0.21) but increases above this value in the range $-4.0 < \theta < 4.0$.

5.4.3 Side force and yawing moment loadings.

These loadings were small in comparison with the normal-force and pitching moment loadings and confirm that the model is closely aligned in yaw to the oncoming flow. These results are not presented as the sole purpose of the analysis was to confirm that the model was aligned accurately to the oncoming flow in the vertical plane..

5.5 Overall forces and moments

The local loadings were numerically integrated to yield the overall forces and moments acting on the model at each pitch angle tested.

The variation of the normal-force coefficient, C_N, with pitch angle is linear up to θ= 4 degrees, Fig 17. Above this angle the curve becomes nonlinear with its slope increasing more rapidly at first before reducing to approximately its initial value. The region of increased slope, $4.6 < \theta < 8.6$ degrees, is the same as that previously described where the position of $(dC_N/dx)_{max}$ moves backwards leading to increased forebody loadings and the observed increase in slope in the normal-force curve.

C_N is positive at zero-pitch angle even though the forebody loading is negative, due to the large positive afterbody loading.

The variation of pitching-moment coefficient, C_m, with pitch angle is shown in Fig 18 and shows no unexpected characteristics.

The variation of the centre of normal-force with pitch angle was derived numerically, Fig 19. At the highest pitch angle, θ = 11.6 degrees, the normal-force centre is at x/L = 0.4390; as pitch is reduced, the centre moves steadily rearwards until, at θ = 2.6 degrees, it is positioned at x/L = 0.8087. Further reduction in pitch causes the

centre to move rapidly rearwards past the base and then move rapidly ahead of the nose. This apparently rapid irregular movement is due to the smallness of C_N in comparison with C_m in this region and the change of sign of C_N.

The total forebody axial-force, C_A, is negative at pitch angles of less than -2 degrees but then becomes positive and increases linearly at an increased rate for $\theta > 4$ degrees, Fig 20.

6.0 THEORETICAL ESTIMATES

Initially there were three theoretical methods available for estimating the pressure distribution over a body in curved flow. These were:-

a) The source-ring method due to Vandrey (ref 4) and developed by Mohammed (ref 5) to deal with more bluff nose shapes.

b) The source-ring solution developed by Deo (ref 6) for determining the pressure distributions over axially symmetric bodies.

c) The Surface Panel And Ring Vortex (SPARV) panel method developed by Petrie (B.Ae Brough), ref 7, as a general method for estimating the pressure distribution and loads on complete aircraft of complicated geometry.

The accuracy of the Mohammed and Deo methods had been checked satisfactorily against Jones' exact method for the prediction of the pressure distribution over a prolate spheroid in curvilinear flow (ref 8). The Deo method had also been shown to agree well with the SPARV method in predicting the pressure distribution over the present ogive-cylinder body in linear flow, and thus to agree closely with the experimental measurements in the CoA lowspeed windtunnel, except in the neighbourhood of the base,(ref 2). It was shown that the theoretical pressure distribution over the rear of the body was affected by the shape of the base closure chosen. Although a suitable base closure was chosen to match the experimental and theoretical pressure distributions at zero pitch angle, the match was not maintained when the pitch was altered. In order to obtain better results over a range of attitude, it was suggested that the shape of the base closure would have to be altered for each attitude, possibly by applying a circular-arc curvature to the centre-line, so that the rear of the closure was tangential to the free-stream direction.

As the SPARV method was the only one not restricted to axi-symmetric bodies and wake closures, this method was chosen to

make the theoretical estimates even though it required considerably more computing power.

6.1 The SPARV panel method

Although the SPARV program had been developed to examine the general effects of rotation, it had been primarily used to examine the effects of rolling an aircraft as this rotation is normally of greater magnitude than rotations about the other axes, and thus is of greater importance.

For rolling about the x-axis, the angle of the helix is normally taken as defining the test condition. This is defined by:-

$$pb/2V_\infty$$

where p = rate of roll about the x-axis

b = wingspan

V_∞= approach velocity

The rotational conditions about the other axes are similarly defined using the wingspan as the unit of length.

In the case of the present tests on the Whirling Arm the effects of rotation about the y-axis are being considered, the corresponding rate of rotation being q. the rate of rotation of the Whirling Arm

As the body has no wings, a length is required to define the flow conditions for SPARV. It would seem that the most appropriate length would be that of the body as the rotation that is being investigated is basically defined by the change in flow direction between the nose and rear of the body.

The other quantity to be considered is V_∞, the approach velocity. In the case of the Whirling Arm, it is not altogether clear whether the approach speed, V_∞, should allow for the swirl in the

test chamber. Eventually it was decided not to make any allowance for swirl in determining the curvature parameter (based on $pb/2V_\infty$) used in the SPARV calculations.

The pitch angles used in the calculations were those previously determined, i.e. with no allowance made for any inflow or outflow that may be present at the position of the model. Thus, by comparison of the experimental and theoretical results, it should be possible to determine the inflow of the approach flow at the model.

The panelling chosen represented the ogive cylinder body by a half body with 51 longitudinal stations (50 panels) and 10 circumferential stations (9 panels), i.e assuming that the body was not yawed. It is usual to close the blunt base of a body by a shape which is meant to represent the dividing streamline between the cavity and free-stream flows. The base closure chosen was an ogive similar to the nose shape as previously used in ref 2. This was represented by a half body with stations spaced at 0.04L longitudinally and again with 10 circumferential points at each station. SPARV calculates the surface pressures at the centroids of the panels and then calculates the local loadings and overall loads by successive integration in the same way as the experimental analysis. As the axial position of the panel centroids are almost identical with the pressure-plotting stations, the loadings are calculated at directly comparable stations. The pressures however are calculated at 20 degree intervals from 10 to 170 degrees roll angle rather than the 10 degree intervals from 0 to 360 degrees as measured.

SPARV calculates the potential flow solution for the flow over the model and then can allow for viscous effects by recalculating the solution with a defined transpiration velocity through the surface of the body. It was found that when using the recommended transpiration condition, the flow separated over most of the body at all the pitch angles that were calculated, presumably because of the large changes of flow direction over the body. Calculating the flow over the body in a straight uniform flow at zero incidence showed a separation-

free flow except for a small region on the forebody near the nose (at x/L = 0.05). As it appeared that considerable experimentation would be required to obtain a suitable transpiration distribution to reproduce the curvilinear boundary layer effects adequately, the potential flow solutions were calculated for the range of experimental conditions tested to see how closely the theoretical solutions agreed with the experimental measurements even though it was anticipated that the agreement would be poor due to the extensive regions of separated flow that were likely to occur.

6.1.1 Analysis of normal-force estimates

The normal-force loading distributions, Fig 21, are rather different from the experimental results, Fig 10. The theoretical loadings over the nose vary in a similar manner to the experimental results, but over the centre part of the body the theoretical loadings are small at all pitch angles instead of having a medium-sized positive value which increases with increase in pitch. The theoretical loadings over the rear of the body become more negative as the pitch angle increases in direct contrast to experiment where the loadings over the rear of the body increase with increase in pitch.

These theoretical loadings have been numerically integrated to give the overall C_N and the results are plotted in Fig 17 together with the experimental results. The variation of C_N with pitch is linear over the whole pitch range in the case of the theoretical estimates and has the same slope as the experimental results at low pitch angles, but is displaced by $\Delta C_N = -0.25$. Above 4 degrees pitch however, the experimental curve becomes non-linear, showing an increased slope initially which gradually reduces with increase of pitch until at the highest angle, it has approximately the original slope.

The characteristics of the forebody loadings have also been investigated. The maximum value of the forebody loading has been plotted against pitch in Fig 11, together with the experimental

variation. The agreement between the two curves is excellent at high and low angles of pitch but less good at intermediate angles because the marked displacement, or joggle, in the curve between 5 and 6 degrees pitch is not so marked in the theoretical estimates. The variation of the position of the peak loading against pitch has been plotted against pitch in Fig 12, again with the experimental results for comparison. Examination of the two curves shows that both curves have the same distinctive shape, but the marked dip on the theoretical curve occurs about a degree earlier and the difference in level between the high and low pitch values is slightly less in the case of the theoretical estimates.

The variation of the normal-force loading at x/L = 0.01 against pitch has been plotted in Fig 13. The theoretical estimates show a linear variation but the slope is considerably greater than the slope of the experimental results. This was to be expected, because as pointed out previously, ref 2, the yawmeter calibration had indicated that the pressure read by that particular tapping was considerably less than other similarly positioned tappings although the pressures varied linearly with pitch in all cases. The reason for this behaviour was found to be because that particular pressure tapping was located in a slight hollow in the surface of the model. However the angle at which the loading was zero will still indicate the angle at which the nose was aligned to the oncoming flow. From geometric considerations this angle should be 5 degrees. The angle at which the theoretical loading is zero is approximately 4.5 degrees. It was originally thought that the difference between the two angles was due to the upwash generated by the body. Upwash will be present even when the nose of the body is aligned with the flow because, experimentally, the curvature of the flow results in considerable positive aerodynamic loading being generated over the parallel afterbody at all pitch angles thus inducing an upwash in the approaching flow. Although this may be true for the Whirling Arm tests, it is unlikely to be true for the SPARV estimates as the theory predicts small negative afterbody loadings and only a small forebody loading resulting in approximately zero overall C_N and thus little induced upwash at a pitch of 4½ degrees.

6.1.2 Analysis of axial-force estimates

The variation of the axial-force loading over the forebody with pitch angle is shown in Fig 22. The distribution has positive and negative parts both of which are sinusoidal in shape with the negative part being dominant at the lowest angle. The positive peak occurs at about $x/L = 0.04$ and the negative peak occurs at approximately $x/L = 0.22$. As the pitch angle is increased the positive peak initially increases steadily in magnitude and moves slightly aft, whilst the negative peak becomes smaller and moves aft. However, at pitch angles greater than 2.6 degrees, there is very little further change with increase in pitch. Comparing these distributions with the experimental ones, Fig 14, it can be seen immediately that the theoretical curves are much smoother and that in the experimental distributions, the magnitude of the peaks continue to change steadily with increase in pitch even though the shape of the curves become more irregular as pitch increases. Analysis of the magnitude and position of the loading peaks, Figs 15 & 16, show reasonable agreement between theory and experiment at the lower pitch angles but some divergence at the higher angles where the theory predicts little change with increase in pitch.

The variation of the overall forebody axial-force with pitch for both theory and experiment is shown in Fig 20. The experimental values increase steadily, but non-linearly, with pitch throughout the range. The theoretical variation, however, is rather different. At negative pitch, the theoretical values are slightly below the experimental values, but at positive angles of pitch the slope of the theoretical curve reduces rapidly with increase in pitch until the curve reaches a peak value at 6 degrees pitch, and then falls away with further increase in pitch until the forebody axial-force becomes zero at an angle of 11 degrees. The reason for this behaviour of the theoretical estimates can be seen from Fig 22. As already noticed, in contrast to the experimental results, Fig 14, the magnitude of the maximum and minimum axial-force loadings vary relatively little above a pitch angle

of 2.6 degrees and so, in this region, the variation of total axial-force with pitch would be expected to be relatively small, as is the case.

It is interesting that the initial distortions in the shape of the axial-force loading distributions occur at the forward positive peak which occurs at about x/L = 0.04. It will be remembered that the theoretical estimates are based on potential flow as it was found that the viscous flow calculations for curvilinear flow indicated extensive flow separations over the whole of the body originating from near the nose, and that even for linear flow the theory indicated a local separation near the nose at zero pitch. These viscous calculations were re-examined and in all cases the initial separation occurred at x/L = 0.05 which is approximately the position of the positive peak in the axial-force loading curve at the lower pitch angles or where the distortion occurs at the higher angles when the peak continues to increase experimentally although not in the theoretical estimates.

6.2 Investigation of the differences between the SPARV estimates and the experimental loadings

As there was considerable disagreement between the SPARV estimates and the experimental measurements of the normal-force loadings over the parallel afterbody in curvilinear flow in contrast to the close agreement between the theoretical and experimental loadings present in linear flow, it was important to see if an explanation could be found for the differences.

6.2.1 Effect of the centrifugal corrections

Although the necessity for applying the centrifugal corrections and the method of estimation were fully established, it was decided to recalculate the loadings using the uncorrected pressure measurements to see how the corrections, ΔC_p = 0.070 applied across the parallel afterbody and ΔC_p up to +/- 0.03 due to pitch, translated into changes in normal-force loading. The resultant loadings at pitch angles

of 11.6 and -6.4 degres are compared with the corresponding fully corrected results in Fig 23. For all stations aft of x/L = 0.4, the uncorrected afterbody loadings are less than the fully corrected results by about 0.035 at both pitch angles. Thus the uncorrected afterbody loadings agree reasonably well with the SPARV estimates but, however, they still show a greater variation with pitch and the loadings still increase aft of x/L = 0.90 rather than decrease as the SPARV estimates do. On the other hand, the forebody loading peaks now occur at about x/L = 0.03 further aft and are about 0.2 less than the corrected results. As the corrected forebody loading peaks agreed well with the SPARV estimates, the effect of removing the centrifugal correction was to make the agreement between the theoretical and experimental forebody normal-force loadings worse.

As Jones's experiment on a prolate spheroid, ref 8, had shown that the experimental results with the centrifugal correction applied had agreed well with the theoretical estimates obtained from the exact theory except over the rear of the body where flow separation took place in the experiment, it would appear that the fully corrected results are to be relied upon and thus the SPARV predictions are in serious error over the parallel afterbody although they are in reasonable agreement over the first 20% or so of the body length.

Other possible causes for the disagreement between the experimental results and the SPARV estimates are the arbitrary decision to ignore the effect of swirl in calculating the rotational parameter used in the SPARV calculations and the arbitrary base closure used to close the bluff base of the body.

6.2.2 The effect of small changes in the flow curvature parameter

The curvature parameter ,q_∞, used in the SPARV calculations had a (rounded) value of -0.175. The calculations were repeated for pitch angles of -6.4, 2.6 and 11.6 degrees with values of

the curvature parameter of -0.150 and -0.200. The normal-force loading distributions are presented in Figs 24 - 26 together with the corresponding results from the initial calculations. The results show that as q_∞ becomes more negative (corresponding to an increase in flow curvature), so do the loadings become more negative over the whole length of the body. The greatest percentage effect will occur at the extreme nose and tail of the body where the flow deflections from the nominal pitch angle (measured at the centre of the model) are greatest, but the greatest observable effect is at the peak forebody loading. Here the increment in loading varies linearly with q_∞ and is 0.08 for q_∞ = 0.025. If the measured swirl is allowed for, the SPARV parameter, q_∞, is altered from -0.175 to -0.193, resuting in a change in the maximum forebody loading of -0.054 which gives closer agreement between the experimental and theoretical values. However the change in curvature parameter makes little difference to the afterbody loadings and thus the value of the flow parameter is not responsible for the large diferences between the theoretical and experimental normal-force loadings over the afterbody.

6.2.3 The effect of changes in closure shape

Considerable differences in opinion exist as to how accurately the flow over the rear of the body needs to be estimated.

One school of thought maintains that the most important region for prediction purposes is near the nose and other regions of high curvature where the velocity perturbations are high and that the effects of the base are relatively unimportant as they will only affect a small region near the base of the body where the velocity perturbations are generally small. Thus no accurate representation of the flow behind the base is required for the calculations and so the body either can be terminated at the base or, in the case of a cylindrical afterbody, the body can be extended a small distance behind it. This school of thought points out that both the viscid and inviscid calculations can only be expected to be accurate near zero pitch as, in

practice, the complex flow patterns and separations that exist over the body at relatively small pitch angles cannot be modelled at present.

The other school of thought acknowledges that the above reasoning is correct, but, as bodies are liable to have to operate at considerable pitch angles in practice, believes that the calculations should be extended over a considerable pitch range to see how well the admittedly inadequate theoretical estimates compare with experimental data. By this means the regions of agreement and disagreement can be determined and, if desired, empirical modifications or corrections be devised. Even if the base effects only cause minor variations in the pressure distribution over the base of the body, the resultant loading changes may not be negligible, ref 2.

When a body is in curvilinear flow the direction of flow at the rear of the body will be generally at a considerable angle to the axis of the body thus making it probable that appreciable afterbody loadings are present as shown experimentally. Even though SPARV did not predict these loadings, it was decided to see what effect was predicted for two base-closure modifications. Firstly to determine the effect of applying a circular arc camber of 5 degrees subtended angle to the existing base-closure so that the tip of the closure was approximately aligned with the undisturbed free-stream flow at zero pitch and secondly the effect of removing the base-closure completely. The loadings were therefore calculated for these two cases at pitch angles of -6.4, 2.6 and 11.6 degrees, and the results are presented in Figs 27 - 29.

Examination of the results shows that the effect of adding camber to the closure can be detected for about 20% of the body length upstream of the base at all pitch angles. The normal-force loadings are decreased over the same region with the magnitude of the decrease becoming progressively greater as the base is approached. However there is little change in the effect of the camber with change of pitch.

The effect of removing the base closure is also shown in Figs 27 - 29. At a pitch of -6.4 degrees, the removal of the closure causes a gradual increase in normal-force loading aft of x/L = 0.8 similar in character to that present in the experimental results. However, by 2.6 degrees pitch, the loading distribution has changed completely. The loadings now begin to diverge aft of x/L = 0.5 with the loading at the base becoming more negative and considerably greater in magnitude than the maximum value of the forebody loading peak. Further increase in pitch to 11.6 degrees results in the loading at the base becoming even more negative resulting in its magnitude now being approximately four times the peak forebody loading at this pitch angle with the distributions starting to diverge at x/L = 0.4

In view of the failure of SPARV to predict the general level of the afterbody loadings that were obtained experimentally and there being no obvious reason to explain the significance of the pitch angle at which the removal of the base closure has no effect, the SPARV predictions should be viewed with considerable scepticism and should be rechecked when the discrepancies between the experimental results and the SPARV estimates have been resolved.

6.3 Theoretical estimates using slender-body and linear theory.

In order to avoid confusion, for the rest of this report what previously has been described as linear flow, i.e. the straight uniform flow usually assumed to exist in wind tunnels or steady-state flight, will be called "straight " flow. Similarly what has previously described as curvilinear flow, i.e. a flow with uniform curvature and speed as assumed to exist in the Whirling Arm or in a steady turning flight, will be called "curved" flow.

The conclusion from the above analysis must be that the agreement between the experimental results and the SPARV estimates whilst good in straight flow is very poor in curved flow as the SPARV

calculations do not predict the high positive afterbody loadings that dominate the curved flow results but instead predict the low negative loadings as previously obtained in straight flow. The effects of small alterations of flow curvature and modifying the base representation although noticeable, have been shown to be small in comparison to the differences between the experimental results and the SPARV estimates.

In the course of discussing these results with D. Isaacs of RAE Bedford, it became clear that he was also dubious of the results obtained from the application of SPARV to curved flow. Isaacs is involved in the prediction of store carriage loads, ref 9, and so is also interested in the effects of flow curvature. He had found that for a 4:1 prolate spheroid in curved flow, the SPARV solution did not agree with the exact solution as described by Jones, ref 8. The comparison is shown in Fig 30. It shows that the agreement between the two methods is poor throughout and that the difference increases progressively as x/L increases towards x/L = 0.5, the position of maximum thickness and also the origin of the axis system.

Isaacs had therefore developed his slender-body and linear theory code that he had been using so that it could be applied to curved flow and used the resultant code to obtain the solution of the spheroid case. The resultant loadings are plotted in Fig 30. From these results it can be seen that both the slender-body and linear theory estimates are in much closer agreement with the exact solution than SPARV. In particular the linear theory results agree almost exactly.

Accordingly Isaacs programmed the ogive-cylinder body shape into his code and calculated the loading distributions for the range of pitch angles tested using both slender-body and linear theory. These loadings are shown in Figs 31 - 32. It should be noted that the theories are for inviscid flow and that no base closure has been included in the definition of the body geometry.

From these graphs it can be seen that:-

a) both theories predict loadings of about 0.35 over the whole of the parallel afterbody, this value agreeing with the lowest values measured experimentally, Fig 9.

b) as was to be expected, the slender-body loading estimates are constant over the parallel afterbody and do not vary with pitch.

c) the linear theory estimates show the carryover of the forebody loadings onto the front of the parallel afterbody and a diminution of loading aft of x/L = 0.90. There is little effect of pitch variation aft of x/L = 0.60.

The derived forebody normal-force loading characteristics obtained from Figs 31 - 32 are plotted in Figs 11 - 13 for comparison with the experimental results and SPARV estimates.

The forebody peak loading is plotted against pitch in Fig 11. The shape of the curve derived from the experimental results is similar to that obtained from the linear theory estimates but displaced by slightly more than +1.5 degrees. The curve obtained from the slender-body estimates is generally similar in character in that the peak loadings at high and low pitch angles fall on parallel straight lines which are joined by a joggle between 1 and 5 degrees pitch, however the joggle is much more pronounced as the peak values predicted by the slender-body theory are more negative than the "linear theory" values at low pitch angles and more positive at the high pitch angles. The "experimental", "slender-body" and "linear theory" curves all have this pronounced joggle, but it is much less pronounced in the "SPARV" curve.

The slender-body and linear theory predictions of the variation of the position of the forebody loading peak with pitch are very similar, Fig 12. The rapid aft movement of the peak loading between 3 and 4½ degrees is the same in both magnitude and extent, but outside this range, the linear theory predicts a peak position slightly further aft than that predicted by slender-body theory . The "SPARV" curve is generally similar to the "slender-body" curve at low pitch angles, but is

displaced by about +1 degree. However the rapid rearwards movement is considerably less in magnitude and occurs about 1 degree later than the "slender-body" curve. There is little variation of the position of the peak loading at the higher pitch angles. In the case of the experimental results, there is little movement of the loading peak at low or high pitch angles and the rapid aft movement of the peak with increase in pitch is slightly (0.03L) less than that predicted by the slender-body and linear theories and is displaced by about +2 degrees of pitch.

The variation of loading at x/L = 0.01 with pitch is plotted in Fig 13. In all cases the variation is linear but the slopes differ appreciably, especially that predicted by slender-body theory. All the theories predict a zero loading at pitch angles between 4.4 and 4.5 degrees while the experimental loading is zero at a pitch angle of 6 degrees.

The pitch datum of the experimental data is somewhat uncertain for two main reasons. First there is the uncertainty due to the flexing of the pitch measuring system with centrifugal force which was not anticipated at the time the tests were done. Secondly there has been no allowance made for any outflow that may be present at the model position when the arm is rotating. As there is such good agreement between the various theoretical methods as to the angle at which the loading at x/L = 0.01 is zero, it would seem logical to accept this value as a proper datum and apply a correction of -1.6 degrees to the experimental angles in order to get a direct comparison between the experimental data and the theoretical estimates. If this was to be done, it can be seen from figs 11 and 12 that there now would be very close agreement between experiment and linear theory in the magnitude of the peak in the forebody loading distribution and reasonable agreement in the variation of the position of the peak with pitch. The agreement with slender-body theory is not quite so good, but is better than the agreement with SPARV.

7.0 DISCUSSION

The application of the above correction to the pitch datum meant that the pitch angles at which the experimental data was obtained were therefore -8.0, -6.0, -4.0, 1.0, 3.0, 5.0, 7.0, 8.0 and 10.0 degrees. The theoretical estimates were then re-computed for these angles by the SPARV, slender body and linear theories. The estimated normal-foce loading distributions are plotted in Figs 33 - 41 together with the experimental results. The experimental axial-force loading distributions are plotted in Figs 42 - 50 together with the SPARV estimates, the slender-body and linear theory estimates not being available.

It had been noted in section 5.4 that, as the experimental normal-force loadings showed considerable scatter over most of the afterbody, the initial analysis was done using smoothed curves. Therefore in this section the experimental loading results will be examined in more detail to see if a reason for the scatter can be found. In addition the experimental loading distributions in the neighourhood of the junction between the forebody and the parallel afterbody will be examined for any signs of a local region of constant loading, and finally a comparison will be made between the corrected experimental results and the various theoretical estimates and between the overall forces etc in curved and straight flow.

7.1 The scatter in the loading measurements

7.1.1 Normal-force loadings

The variation of dC_N/dx along the body has been plotted separately for each pitch angle in Figs 33 - 41. Both the "mainline" and "auxiliary-line" data are shown.

Examination of the data obtained from the "mainline" tappings shows that although there is some scatter in the forebody loadings, in general there is considerable scatter in the loadings

between x/L = 0.5 and 0.90. In particular, the scatter is very regular in this region in that alternate readings form two curves, one which is a natural extension of the curve up to x/L = 0.5 and the other which diverges rapidly from the original in a positive direction, then runs parallel to it before rejoining it rapidly aft of x/L = 0.8. It should be noted that this scatter seems to be a maximum at pitch angles near 0 degrees and decreases as the pitch angle moves away from this region. In particular there is very little scatter in the results at pitch angles of 8.0 and 10.0 degrees, Figs 40 & 41.

The fact that the scatter is of this form indicates that the cause is an instrumentation problem. This is because the pressure tappings were connected alternately to the two pressure switches. When the scatter was first noticed during the tests, it was assumed that a particular transducer was at fault because it was giving problems if it was used continuously for long periods. It was decided not to investigate further at the time because the scatter in the pressure readings, although regular and noticeable, was not large. However, when the pressure readings were corrected for centrifugal effects and integrated to obtain the loadings, the scatter in the loadings became much more noticeable as shown in the graphs. Further examination of the loadings has shown that the data which is suspect was obtained from the pressure tappings connected to the transducer that was thought to be working correctly. It would therefore seem probable that the problem is caused by some effect of centrifugal force which has not been traced so far, as neither the transducer or pressure switch is obviously at fault.

If we now examine the results obtained from the check data from the "auxiliary-line" pressure tappings, it is seen that the loadings are more positive over the whole length of the body, the amount varying somewhat with pitch angle. However, the loadings agree closely at a pitch angle of 10.0 degrees, the same angle at which the scatter of the loadings over the afterbody is a minimum. Ignoring for the present the stations near the forebody/afterbody junction, the "auxiliary line"

results vary relatively smoothly along the length of the body and do not show the excessive scatter noticed in the "mainline" results even though the tappings are also connected alternately to the two pressure switches. This difference between the "main" and "auxiliary" sets of data had also occurred in the tests in straight flow reported in ref 2 . In these tests, the differences were not only equally large but were bi-directional in that while the afterbody loadings measured by the auxiliary tappings were always more positive than those obtained from the main tappings, the loadings over the nose section as measured by the auxiliary tappings were more negative than the "mainline" loadings at low pitch angles, more positive at intermediate angles and almost identical at the highest angles. No satisfactory explanation of this behaviour has been found so far.

7.1.2 Axial-force loadings.

The scatter in the results could only be examined over the forebody, (Figs 42-50), because the loadings over the afterbody were automatically zero as a result of resolving the pressures. There was some scatter in the "mainline" results which showed evidence of being transducer dependent, but the scatter was not sufficient to make it difficult to draw a mean curve through the data.

The agreement between the "mainline" and "auxiliary line" results was very good except at $x/L = 0.01$ where there was a consistent discrepancy between the loadings due to a consistent error in the "mainline" pressure readings as a result of the location of the pressure tapping as discussed in ref 2.

The alteration of the pitch datum for the experimental measurements has resulted in some changes in the comparison between the experimental results and the SPARV predictions.

At -8 degrees pitch, the agreement between experiment and theory is fair with the magnitude of the rear (suction) loading peak being rather greater than predicted. As pitch is increased, the comparison changes. The forward (drag) peak grows in magnitude faster than predicted and is positioned farther aft. The suction peak decreases in magnitude at a much faster rate than predicted, but remains in the predicted position. Both these differences will result in the forebody pressure drag being greater than predicted.

7.2 Possible region of constant loading near the forebody/afterbody junction

The discontinuity in curvature that occurs at the junction of the forebody and afterbody leads to a sudden relaxation in the pressure gradient and this in turn sometimes results in the pressure distribution around the rear of the forebody persisting over a small region aft of the shoulder. Thus if such a region exists, it shows itself as a small region of constant loading at the forebody/afterbody junction. As the tests in straight flow, ref 2, showed that such a region was present on this particular body, the loading distributions were examined to see whether it was still present in curved flow.

The analysis was rendered more difficult because the results in this region were also affected by the scatter in the results. The differences were not large, but resulted in the closely spaced loadings appearing as a block of points when closer analysis of the pairs of alternate points on the curve showed that they had a common slope and so probably lay on a smooth curve. Bearing this in mind, the loading distributions, Figs 33-41, show clear evidence that a small region of constant loading is present except in the region of zero pitch where the experimental scatter is excessive over much of the body and where the slope of the loading distribution is nearly zero in any case. Thus the curved flow results show the same regions of constant loading just aft of the forebody/afterbody junction that were present in straight flow.

7.3 Comparison of the theoretical loading estimates with the corrected experimental results

7.3.1 Comparison between experiment and linear theory

At a pitch angle of -8.0 degrees, Fig 33, there is close agreement between the experimental normal-force loadings and the linear theory predictions up to x/L = 0.4. Beyond this, the theoretical values increase slowly with x/L whilst the experimental values remain almost constant until the region where the large experimental scatter begins. In this region the theoretical loadings remain constant and the linear theory estimates are roughly the median of all the experimental values. Aft of x/L = 0.85 the excessive scatter of the experimental results is much smaller and the experimental loadings begin to increase with x/L, especially near the base (x/L > 0.95), while the theoretical estimates begin to decrease slowly as x/L increases.

As pitch increases, Figs 34 - 41, the same general pattern is maintained but the position at which the theoretical values begin to become greater than experiment gradually moves towards the nose until at a pitch angle of 1.0 degrees, the divergence begins just aft of the position of the forebody peak loading (x/L = 0.15).

At 3.0 degrees pitch, Fig 37, there is a very considerable scatter in the experimental results over the whole length of the body which makes it difficult to make a precise comparison, but most of the "main-line" loadings are less than those predicted by theory while the check loadings are greater.

With further increase in pitch, the scatter in the experimental results reduces rapidly and the difference between the main and check loadings also decreases until, by 7.0 degrees pitch, all the theoretical and experimental results agree closely except, as usual, over the last 10% of the body length. At higher angles, a slight change in the general features of the comparison becomes apparent. The forebody

loadings predicted by linear theory become appreciably greater than experiment and at the same time, the afterbody loadings become less than the experimental values.

To summarise, except at the highest pitch angles the inviscid linear theory predicts the experimental forebody loadings closely but predicts afterbody loadings that are rather higher than experiment. The divergence between the theoretical and experimental distributions begins over the rear of the forebody and is pitch dependent. The most obvious difference between the results is over the last 5% of the body length when the experimental loadings increase rapidly towards the base whilst the linear theory predicts a gradual decrease. In view of the large variation in flow inclination over the body, it is surprising that an inviscid theory predicts the loadings so closely as it is only at the highest pitch angles that a change in the general balance of the forebody and afterbody loadings become apparent which presumably is due to a fundamental change in the flow over the body due to separations.

7.3.2 Slender-body theory

Examination of the slender-body theory normal-force loading distributions, Figs 33 -41, shows that the slender-body theory consistently overestimates the magnitude of the peak forebody loading by about 10% as compared with the linear theory and experimental distributions and that the peak occurs slightly further aft.

The afterbody loadings do not vary with either axial position or pitch as would be expected from the assumptions of the theory and so there is no "carry-over" from the forebody loadings onto the afterbody or any change in loading near the base.

The afterbody loading is greater than the linear theory predictions at all pitch angles, the difference decreasing with increase in pitch because of the increase in afterbody loading with

pitch that is predicted by linear theory. The experimental afterbody loadings are considerably less at low pitch angles but because of the relatively large increase of loadings with pitch become greater than the slender-body estimate at higher pitch angles.

7.3.3 The SPARV estimates

The agreement of the SPARV estimates with the other results is poor primarily because of its failure to predict the level of the afterbody loadings although, in addition, the forebody peak loadings are consistantly too negative and the position of the peak is not well predicted. The previous conclusion, section 6.1.1, that the experimental and SPARV estimates of the forebody loadings were in good agreement has been altered as a result of the application of the correction to the pitch angle necessary to ensure that the experimental and theoretical loadings at x/L = 0.01 were zero at the same angle.

The variation of the afterbody loadings with pitch is small in the middle of the afterbody, but the loading over the rear of the body gradually becomes more negative with increase in pitch in a similar manner to the linear theory predictions.

7.4 The comparison between the measured overall aerodynamic characteristics and the various theoretical estimates

The comparisons between the theoretical variation of the C_N and C_m with pitch and the fully corrected experimental results are shown in Figs 51 and 52 . The resultant variation of the position of the centre of normal-force is shown in Fig 53. The variations of the total forebody pressure drag, C_A, are shown in Fig 54. It should be noted that the coefficients are obtained by numerical integration of the "main-line" loadings and thus are affected by the scatter in the data. As described previously, the data thought likely to be in error was greater than the preferred data, and so the derived coefficients will be rather

greater than the probable values except at pitch angles $\geq$ 7 degrees where the scatter is small.

7.4.1 Comparison of the variations of C_N with pitch

As a result of the shift in the pitch datum, the experimental variation of C_N with pitch, Fig 51, is now in much closer agreement with the slender-body and linear theory estimates than before with the linear theory estimates being in best agreement. Conversely, the agreement between the the experimental results and the SPARV estimates is worse.

The characteristics of the experimental curve are rather different from the theoretical predictions. All the theories predict a variation that is closely linear. The experimental curve, however, is non-linear. The results are approximately linear betwween -8 and +2 degrees pitch with a slope slightly less than the slender-body and linear estimates but similar to that predicted by SPARV. As pitch is increased, the slope of the experimental curve first increases then decreases until the slope has the original value at 7 degrees pitch and continues to decrease as pitch increases further. As the experimental and linear theory curves have the same value at -6 degrees, the experimental curve oscillates about the theoretical curve, which therefore is a reasonable straight-line approximation to the experimental results.

The agreement with the slender-body estimates is less satisfactory because the slender-body curve, although parallel to the linear theory curve, intercepts the pitch axis at -5 degrees rather than at -4 degrees. As a result the experimental C_N values are always slightly less than the correspomding slender-body estimates although the difference is very small near 7 degrees pitch

As the SPARV curve intercepts the pitch axis at +4½ degrees, its agreement with the experimental results is extremely poor.

The reason for the difference in the initial slopes of the experimental and linear theory curves is the progressive reduction of the experimental normal-force loadings in the region near the forebody/afterbody junction when pitch increases as compared with the theoretical curve. As the pitch increases beyond +2 degrees, the experimental afterbody loadings begin to increase at a faster rate than the theoretical predictions, and the relative reduction in loading that occurs experimentally in the region of the shoulder of the body is gradually eliminated thus increasing to the slope of the experimental curve. With further increase in pitch, the experimental forebody loading peak begins to decrease relative to the theoretical estimate whilst the afterbody loadings stabilise as the effects of the experimental scatter diminish thus leading to the observed decrease in slope of the C_N curve.

7.4.2 Comparison of the variation of C_m with pitch.

As the pitching moments are measured about the nose of the body, the high positive afterbody loadings measured experimentally and predicted by the slender-body and linear theories have a dominant effect in that all values of C_m for these cases are large and negative, Fig 52.

The variation of pitching moment with pitch angle is linear for both the slender-body and linear theory estimates but, in contrast to the normal-force curves, the slopes differ. This is due firstly to the slender-body predictions of afterbody loading being constant with increase in pitch whilst linear theory predicts an increase in the afterbody loadings with increase in pitch and secondly to the carry-over of the forebody normal-force loadings onto the afterbody which is present in linear theory but absent in the slender-body estimates. As would be expected, the shape of the experimental normal-force curve and its relationship to the slender-body and linear theory estimates is mirrored in the experimental curve, but the variation from a straight line are somewhat magnified because of the differences in the normal-force loadings between the experimental and

theoretical results are mainly over the afterbody and thus have a proportionally greater effect on the pitching-moment curve.

As SPARV predicts negative afterbody loadings at all pitch angles, the pitching moment is positive at most pitch angles and it is not until a pitch angle of 10 degrees that the pitching moment contribution from the forebody loading peak is sufficient to reduce the overall pitching moment to zero. The resulting pitching moment curve is linear and its slope is rather less than the other curves. Thus the agreement between the SPARV estimates and the other curves is poor.

7.4.3 Comparison of the positions of the centre of normal-force

The position of the centre of normal-force relative to the nose was obtained by dividing C_m by C_N and is presented on the graph so that distances behind the nose are positive. Thus the variation of the centre of normal force with pitch is discontinuous at the angle that C_N is zero. In the cases where C_m is always negative, i.e. the experimental, slender-body and linear theory cases, the curve goes to infinity behind the nose when approached from the side where C_N is -ve and infinity in front of the nose when approached from the opposite direction. In the case of the SPARV results, C_m is always +ve in the test range so the direction in which the curve goes to infinity is reversed.

At +ve pitch angles, the variation of the centre of normal-force with pitch for the experimental, slender-body and linear theory results, Fig 53, is identical above +1 degree pitch, varying from 0.75L behind the nose at +1 degree pitch to 0.4L behind the nose at 10 degrees pitch. At lower angles the curves diverge as the slopes rapidly increase as the curves go to infinity at slightly different angles between -4 and -5 degrees pitch. Because of the limited pitch range covered at -ve C_N, the curves do not have time to coalesce and the

centre of normal-force position varies between 0.5L and 3L in front of the nose in this pitch range.

In the case of the SPARV estimates the variation of the centre of normal-force with pitch is completely different. At pitch angles from -8 to +1 degree the centre of normal-force is constant at 0.4L behind the nose before moving rapidly rearwards to reach infinity at +4.6 degrees, the angle at which $C_N = 0$. The pitch range covered at positive C_N is barely sufficient for the centre of normal-force position to settle to a constant value, but the load centre has moved rearwards from infinity ahead of the nose to reach the nose at 10 degrees pitch.

7.4.4 Comparison of forebody axial-force

Estimates of the forebody axial-force variation with pitch have only been made using SPARV. Fig 54 shows the comparison between the SPARV estimates and the measured values with the additional pitch correction. This additional correction makes the agreement between the curves worse than previously, but not as bad as the agreement between SPARV and experiment in the cases of normal-force, pitching moment and the position of the centre of normal-force. This is to be expected as the most significant differences between the experimental and SPARV estimates occur over the parallel afterbody and so make no contribution to axial-force.

7.5 The effect of flow curvature on the measured aerodynamic characteristics of the body

The experimental C_N v θ curves for straight and curved flow, (Fig 51), have the same slopes at low pitch angles, but the body develops considerably more normal-force in curved flow as the angle for zero normal-force is -4 degrees in curved flow as against 0 degrees in straight flow. The curves are parallel up to a pitch of about

3 degrees but above this, the two curves diverge. In straight flow the slope of the curve decreases with increase in pitch, but in curved flow, initially the slope increases rapidly with increase in pitch but then gradually reduces with further increase in pitch.

To understand the reasons for these changes it is necessary to look at the loading distributions. In both straight and curved flow the forebody loading distributions are broadly similar in character as there is a pronounced peak whose magnitude varies smoothly with pitch and changes sign with the pitch angle at the nose. The main distinguishing feature between the flows however is the afterbody loadings. In straight flow at positive pitch, the loadings over most of the afterbody are constant, small and negative and vary little with pitch. These loadings are also symmetrical about zero pitch. In curved flow, however, the loadings are again constant over most of the afterbody, but they are much greater in magnitude, are positive in sign regardless of whether the pitch is positive or negative and increase slightly more with increase in pitch. It is these differences in the afterbody loadings that account for the extra normal-force present in curved flow and also for the initial slope of the normal-force curves being basically the same in both straight and curved flow.

No explanation for these features of the normal-force loadings in curved flow has so far been advanced. It is not sufficient to use concepts based on linear flow at the local pitch angle to explain what must be a highly complex flow. For example, when the body is inclined at -5 degrees to datum, the rear of the body is aligned with the undisturbed local flow but it still produces a considerable positive normal-force loading. Now as the local pitch angles over the nose will be considerably negative, by normal "straight-flow" reasoning it would be anticipated that flow breakdown would have occurred leading to a vortex system which would be on the underside of the body and thus induce negative loadings over the afterbody rather than the positive loadings measured. Thus the flow over the body must depart appreciably from that expected in straight flow.

Another feature of the loading distributions that is of interest is the loadings adjacent to the base. In both straight and curved flow the loadings over the extreme rear of the afterbody, (x/L > 0.95), increase rapidly in magnitude as the base is approached, the amount of the increase being slightly pitch dependent in both cases. In straight flow the distribution is symmetrical about zero pitch. However, in curved flow, the increase in loading is always positive regardless of whether the pitch is positive or negative. This increase in loading towards the base does not seem to have been noted in other experiments, e.g refs 10, 11 and 12, because the pressure tappings did not extend far enough aft. As mentioned previously, changes in loading distribution near the base have been predicted theoretically, but they have been in the wrong direction to those measured experimentally.

Because of the large positive loadings over the afterbody, the body pitching moments are considerably more negative in curved flow, Fig 52, and the centre of pressure positions are considerably further aft (0.2L)than in linear flow, Fig 53.

From these results it would seem that the assumption is not justified that it is possible to estimate the aerodynamic loads on a body in a curved flowfield by estimating the flow direction at the centre-of-gravity position and then using this in conjunction with the aerodynamic characteristics of the body in linear flow to estimate the loads. If this method is used then the normal-force will be considerably greater, the pitching moments will be considerably more negative and the position of the centre of normal-force will be considerably farther aft than estimated.

8.0 CONCLUSIONS

The pressure distribution over an ogive-cylinder body has been measured over a wide range of pitch in the curved flowfield provided by the CoA Whirling Arm facility. From these pressure distributions, the loading distributions over the body have been determined as have the aerodynamic characteristics of the complete body.

Analysis of the results have shown that:-

1) Loading distributions

The forebody normal-force loading distributions show that there is a well defined loading peak whose magnitude varies almost linearly with pitch at high positive or low negative values of pitch and whose position is at approximately $x/L = 0.11$ at negative pitch and $x/L = 0.19$ at positive pitch.

In the region where the nose is approximately aligned with the oncoming flow, rapid changes occur in both the position and magnitude of the loading peak as the transition take place from one region to the other.

The afterbody normal-force loadings vary little with position aft of $x/L = 0.45$ until at $x/L > 0.95$ they increase rapidly towards the base of the body.

The afterbody normal-force loadings are always positive regardless of whether the pitch angle is positive or negative and vary relatively little with pitch ($0.3 < dC_N/dx < 0.4$).

The forebody axial-force loadings show that there is a sinusoidal type of loading distribution over the forebody with a positive loading peak occuring near the nose and a negative peak near the rear of the forebody. As pitch becomes more positive the relative

sizes of the peaks change with the positive peak becoming larger and the negative peak smaller.

2) Aerodynamic characteristics of the complete body

Because of the high positive afterbody loadings at all pitch angles, C_N is positive at all pitch angles greater than -5 degrees and varies linearly with increase of pitch until +5 degrees pitch. At higher angles C_N initially increases at a greater rate but the rate of increase begins to fall off at higher pitch angles.

The pitching moment about the nose of the body is negative at all pitch angles because the negative pitching moment contribution from the afterbody varies little with pitch and is sufficient to override the forebody contribution. The variation of C_m with pitch is similar in shape to that of C_N with pitch.

The centre of normal-force, (C_m/C_N), is 0.4L behind the nose at 10 degrees pitch and moves rearwards almost linearly with decrease in pitch to 0.8L behind the nose at +1 degree pitch. At lower pitch angles the position of the centre moves rearwards rapidly as C_N approches zero. When C_N becomes negative, the centre of normal-force goes well forward of the nose, but approaches the nose as pitch decreases until at -8 degrees pitch, it is positioned at 0.4L forward of the nose.

The forebody pressure drag varies almost linearly with pitch, varying between C_A = -0.12 at a pitch of -8 degrees and C_A = 0.11 at 10 degrees pitch.

3) Comparison with theoretical estimates

The experimental results were compared initially with a version of the widely used SPARV panel method which had been modified to allow for the effects of rotational velocity. The forebody loadings

obtained were in good agreement with the experimental results, but the method failed completely to predict the high afterbody loadings present in the experimental results.

Estimates were also made using slender-body and linear theory versions of the widely used NEAR programme which had also been modified to incorporate the effects of rotational velocity. Both methods predicted the experimental afterbody loadings reasonably well, but over estimated the forebody loadings. Analysis of the forebody loads showed that all three estimation methods agreed closely in their estimation of the angle at which the nose was aligned with the oncoming airstream, but this angle was some 1.6 degrees less than that measured experimentally, presumably because of the inflow present in the Whirling Arm at the model position. When this correction was applied to the experimental pitch angles, the experimental results agreed well with the linear theory predictions. The agreement with the slender-body estimates was less good and the agreement with SPARV was poor.

4) The effects of flow curvature

Comparison of the Whirling Arm test results with those of a similar experiment done on the same model in the straight flow provided by a lowspeed windtunnel showed that:-

The normal-force loadings differed appreciably. In straight flow the forebody peak, whilst varying smoothly in magnitude with pitch, did not vary in position and these characteristics were symmmetrical about zero pitch. In curved flow, the forebody loadings also varied relatively smoothly with pitch but there were two distinct longitudinal positions for the loading peak at negative and positive pitch which varied by approximately x/L = 0.08 and which bracketed the position measured in straight flow. The transition region between these two conditions was centered about the angle at which the nose was aligned with the oncoming flow. As the initial slope of the loading distribution varied linearly with pitch, considerably greater peak

loadings were present at high positive pitch angles because of the farther aft position of the peak loading.

In straight flow, the afterbody loadings are constant and slightly negative over most of its length and, in addition, are symmetrical about zero pitch. In curved flow, the afterbody loadings, whilst also constant over most of its length, vary slightly more with pitch and, most importantly, are large and positive at all pitch angles irrespective of sign.

Primarily because of the large positive afterbody loadings present in curved flow, the variations of C_N and C_m with pitch, although similar in slope in straight and curved flow, are displaced considerably. As a result the body in curved flow generates considerably more normal-force and a considerably more negative pitching moment at a given pitch angle resulting in a centre of normal-force which is some 0.2L further aft in curved flow.

For these reasons, the widely used method of estimating the forces and moments on a body in curved flow by estimating the magnitude and direction of the flow at the body centre and then using these conditions combined with the body characteristics obtained in straight flow to estimate the loads etc acting on the body at that position is likely to be considerably in error.

9.0 ACKNOWLEDGEMENTS

The author would like to thank Attack Weapons and Aerodynamics Departments, Royal Aircraft Establishment, Farnborough, Hants, for their financial support for this work which formed part of the work done under Agreement No 2028/131-XRAW.

The author would like to acknowledge the help given to him by:-

a) E.W. Osbourn in the recommissioning of the Whirling Arm, helping with the tests and dealing with the many instrumentation problems that arose.

b) D.Isaacs of Aerodynamics Department, R.A.E. Bedford, for providing the linear and slender-body theory estimates.

REFERENCES

1 Llewelyn-Davies, D.I.T.P — The redesign of the College of Aeronautics Whirling Arm Facility
CoA Report No 8702, March 1987

2 Llewelyn-Davies, D.I.T.P. — The experimental determination of the subsonic aerodynamic characteristics of an ogive-cylinder body including a comparison with theoretical estimates.
CoA Report No 8509, June 1985

3 Braslow, A.L. — A review of factors affecting boundary layer transition
NASA Technical Note NASA TN D-3384, 1966

4 Vandrey, F. — A method of calculating the pressure distribution of a body of revolution moving in a circular path through a perfect incompressible fluid
R&M 3139 1953

5 Mohammed, A. — An integral equation technique for evaluating the aerodynamic characteristics of bodies of revolution in curved flight.
M.Sc Thesis, Cranfield Institute of Technology, 1982

6 Deo, H.S. — Numerical Techniques for predicting Aerodynamic characteristics of bodies
Ph.D Thesis, Cranfield Institute of Technology, 1986

7	Petrie, J.A.H	Development of an efficient and versatile panel method for aerodynamic problems. Ph.D Thesis, University of Leeds, 1979
8	Jones, R.	The distribution of normal pressures on a prolate spheroid R&M 1061, Dec 1925
9	Isaacs, D.	Improvement in store carriage load prediction at subsonic speeds using a development of NEAR trajectory calculation method. Paper 5, AGARD-CP-389
10	Tinling, B.E. Allen, C.Q.	An investigation of the normal-force and vortex-wake characterisrics of an ogive-cylinder body at subsonic speeds. NASA Technical Note NASA TN-D-1297, January 1962.
11	Trebble, W.J.G. Holford, J.F.	Lowspeed windtunnel measurements and estimations of the pitching and yawing moments of tanks mounted on struts under 40 degree swept and straight wings. RAE TN Aero 2394, 1955.
12	Fail, R. Holford, J.F	Preliminary note on the lowspeed tunnel model tests of pressure distribution and jettisoning of strut tanks on a 40 degree swept back wing. RAE TN Aero 2095, 1951.

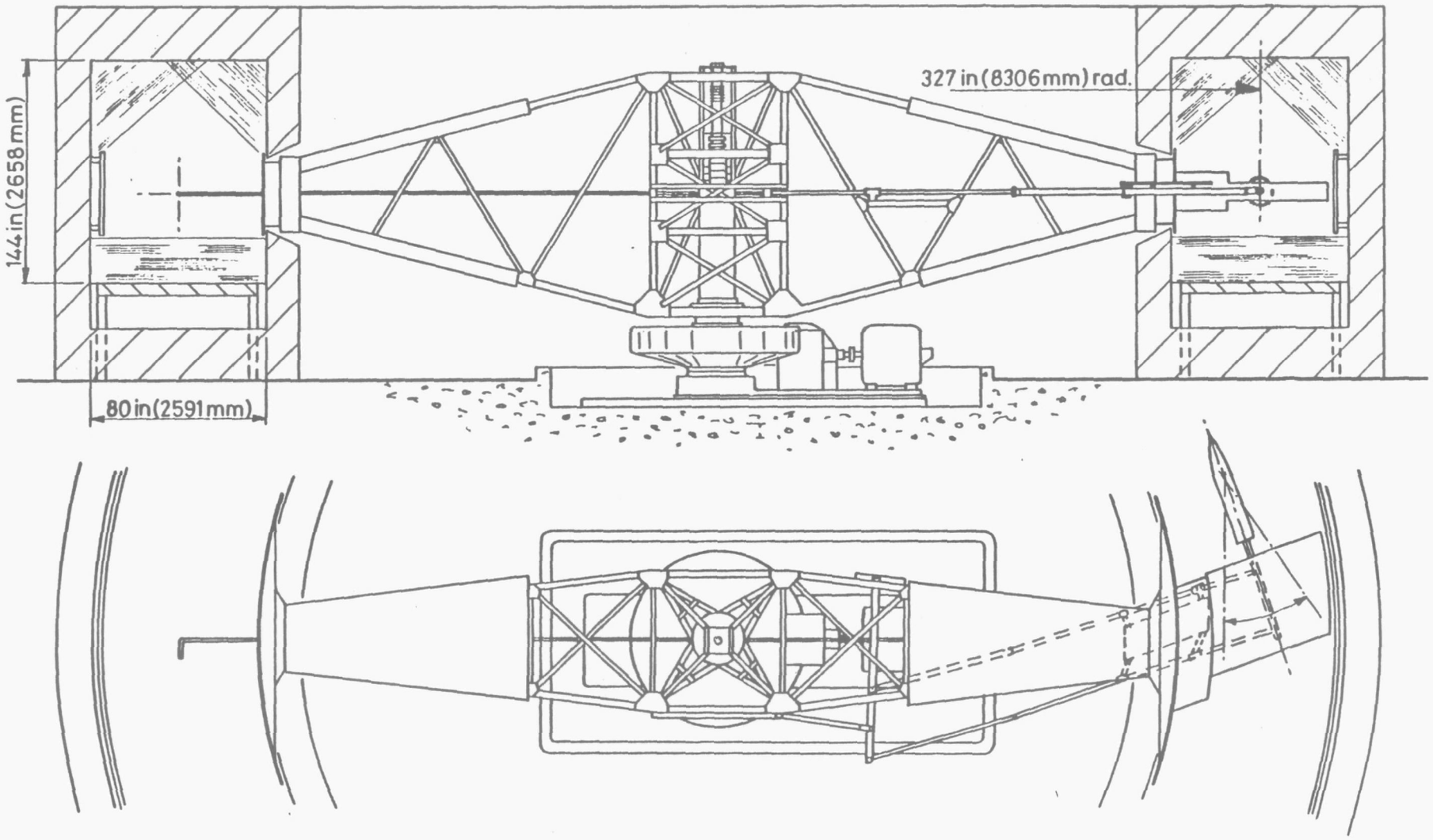

Figure 1. Modified C of A Whirling Arm.

Figure 2. General view, C of A Whirling Arm.

Location of pressure holes, (% of body length)

Main line, ($\phi = 0$) :- 0, 1- 99% in increments of 2%

Auxiliary line, ($\phi = 180$) :- 11, 21, 31, 33, 33.5, 34, 34.5, 41, 51, 61, 71, 81, 91%

Yaw meter, ($\phi = 0, 90, 180, 270$) :- 1%

Figure 3. Ogive-cylinder pressure-plotting body.

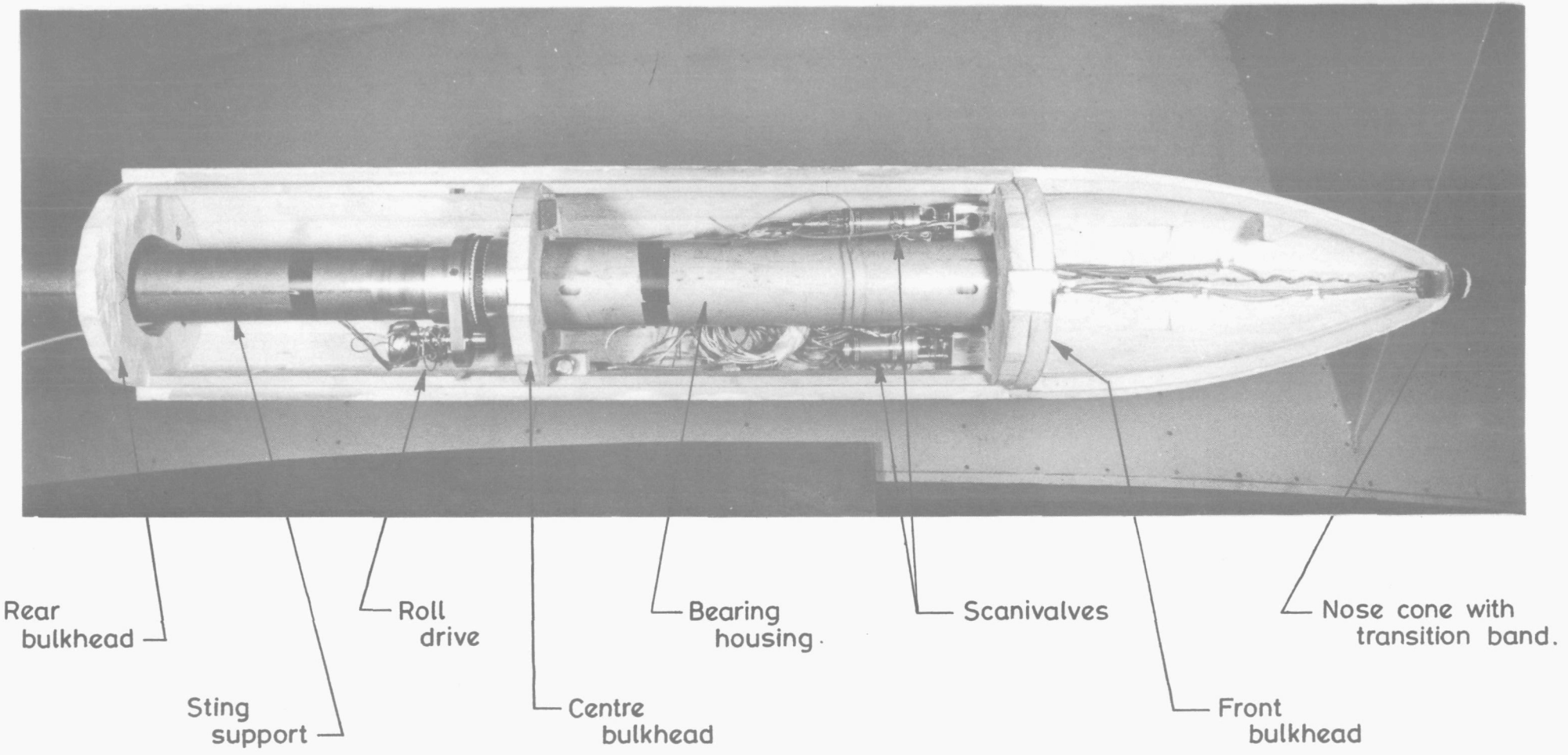

Figure 4. Model details.

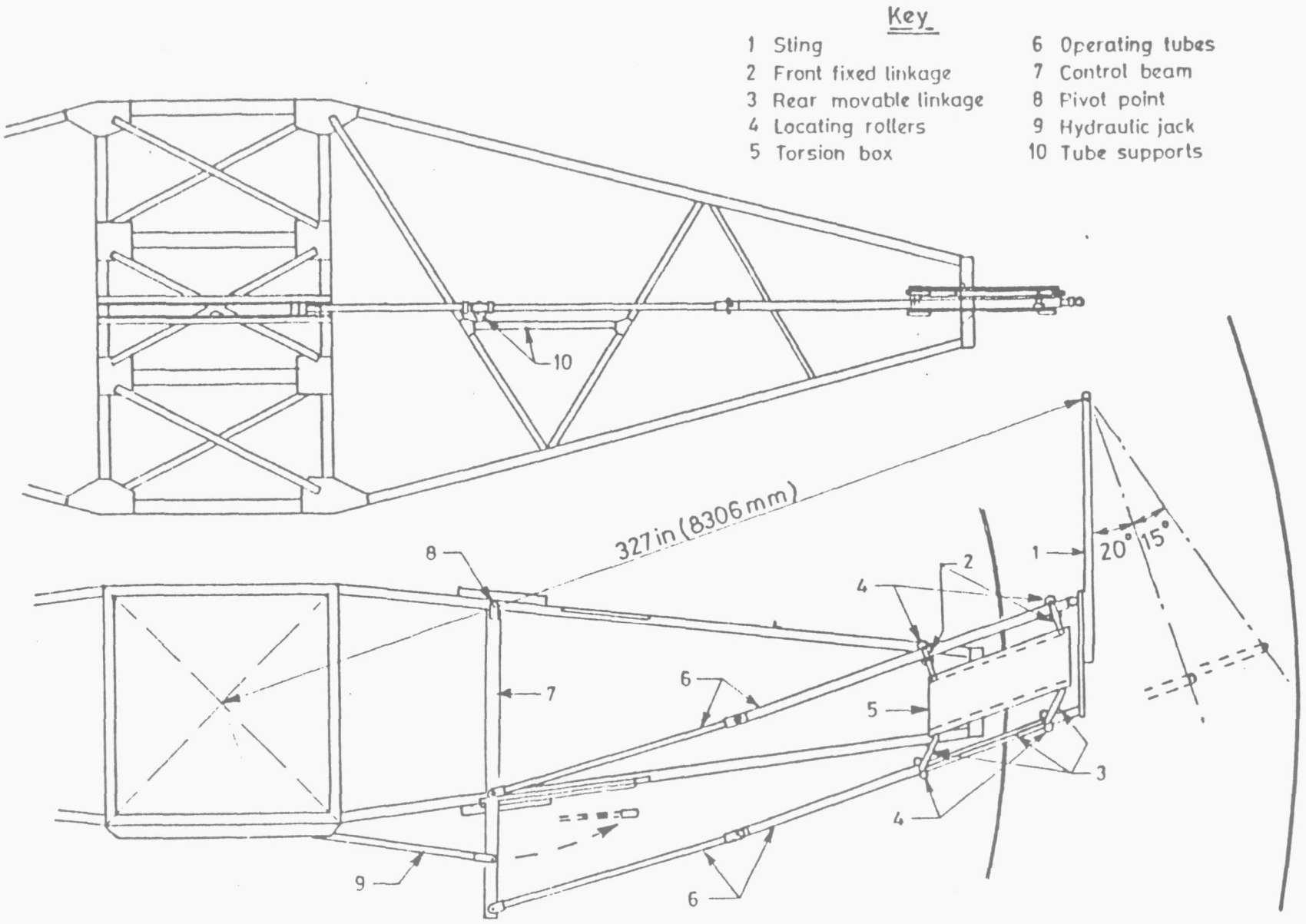

Figure 5. Pitch change linkage

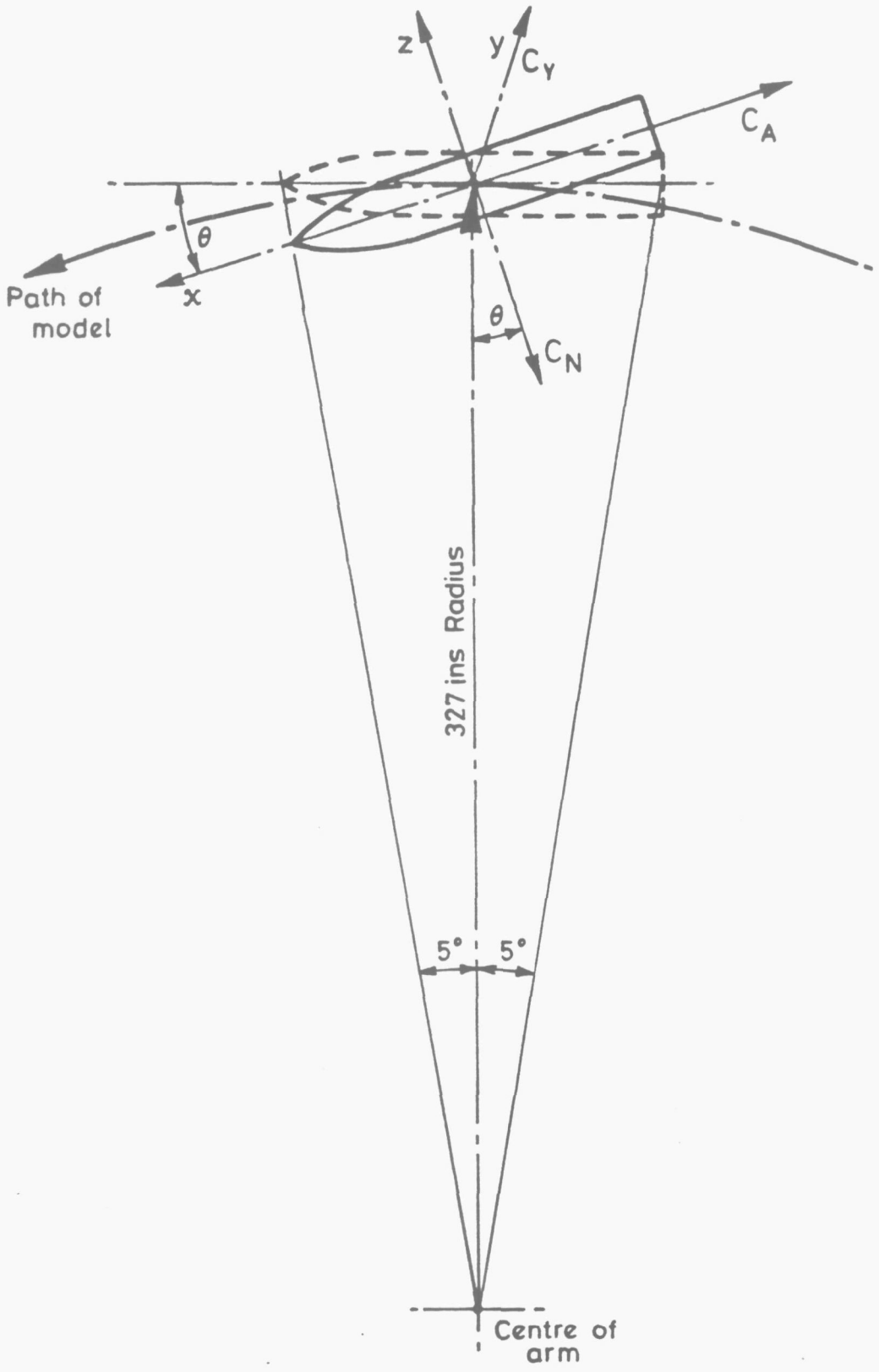

Figure 6. Geometry and system of body axes.

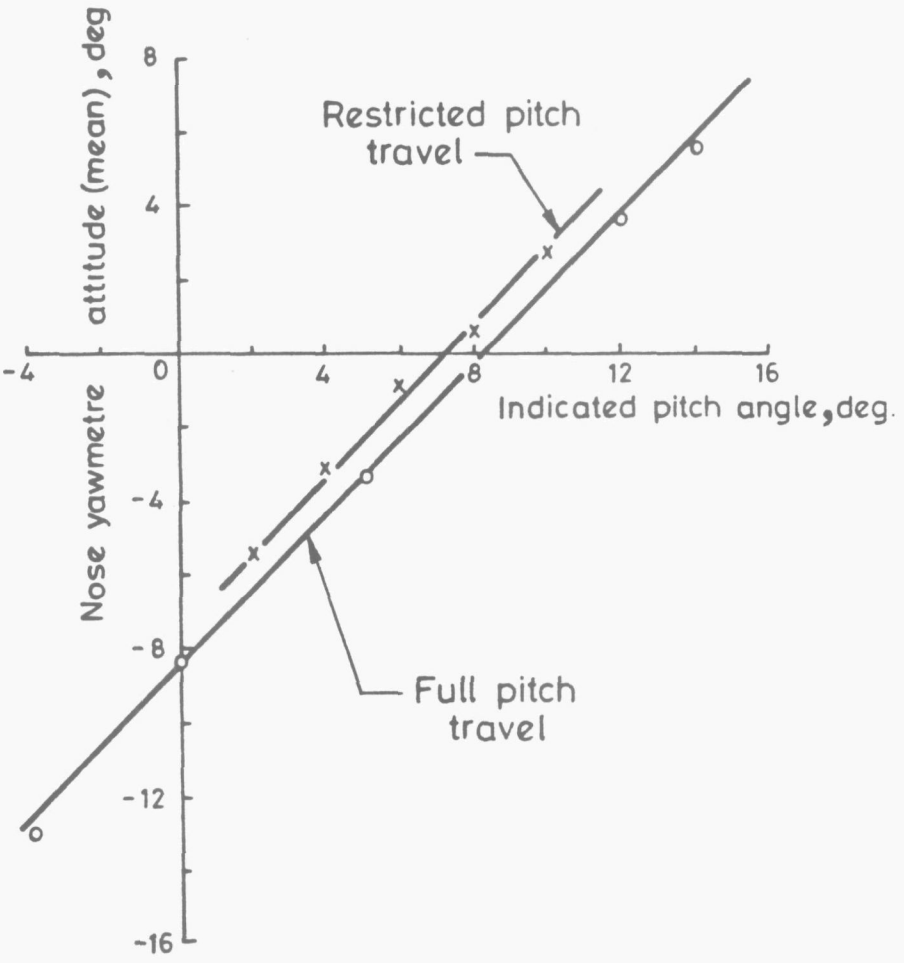

Figure 7. Pitch angle calibration.

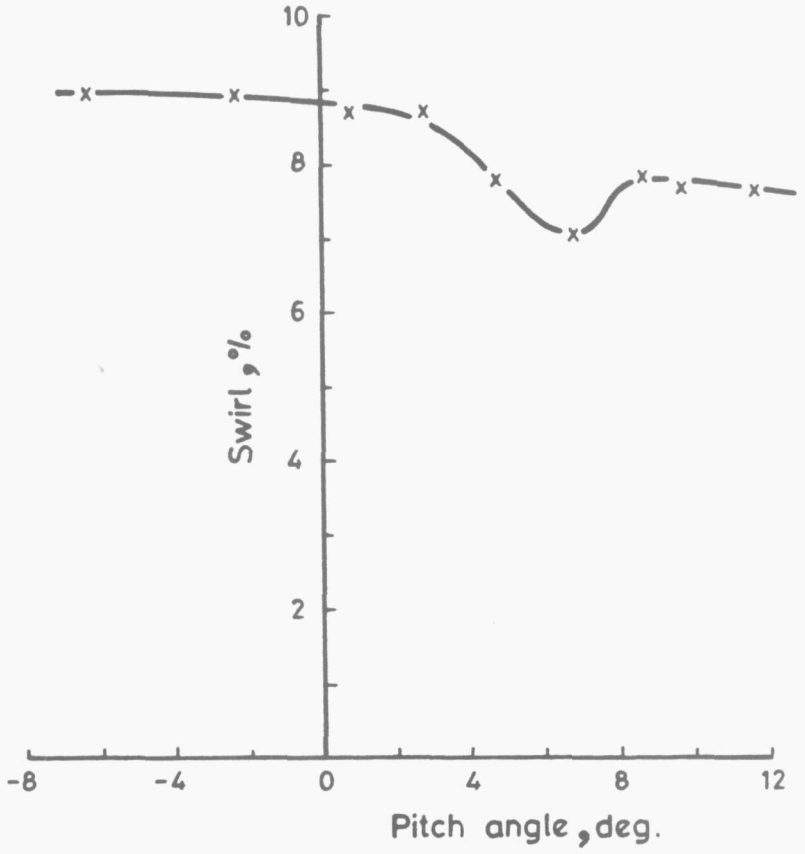

Figure 8. Variation of swirl with model pitch.

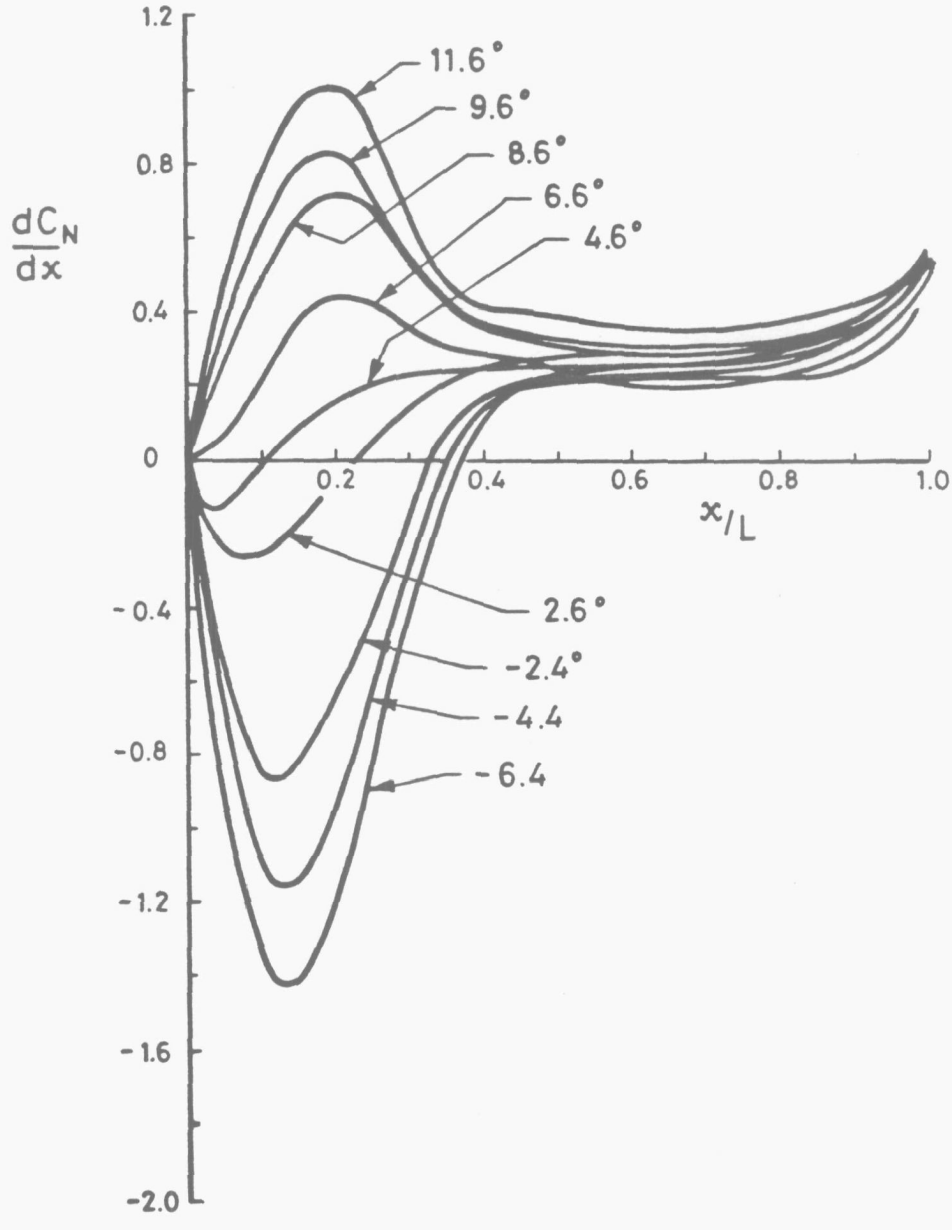

Figure 9. Variation of normal force loading distribution with pitch angle.

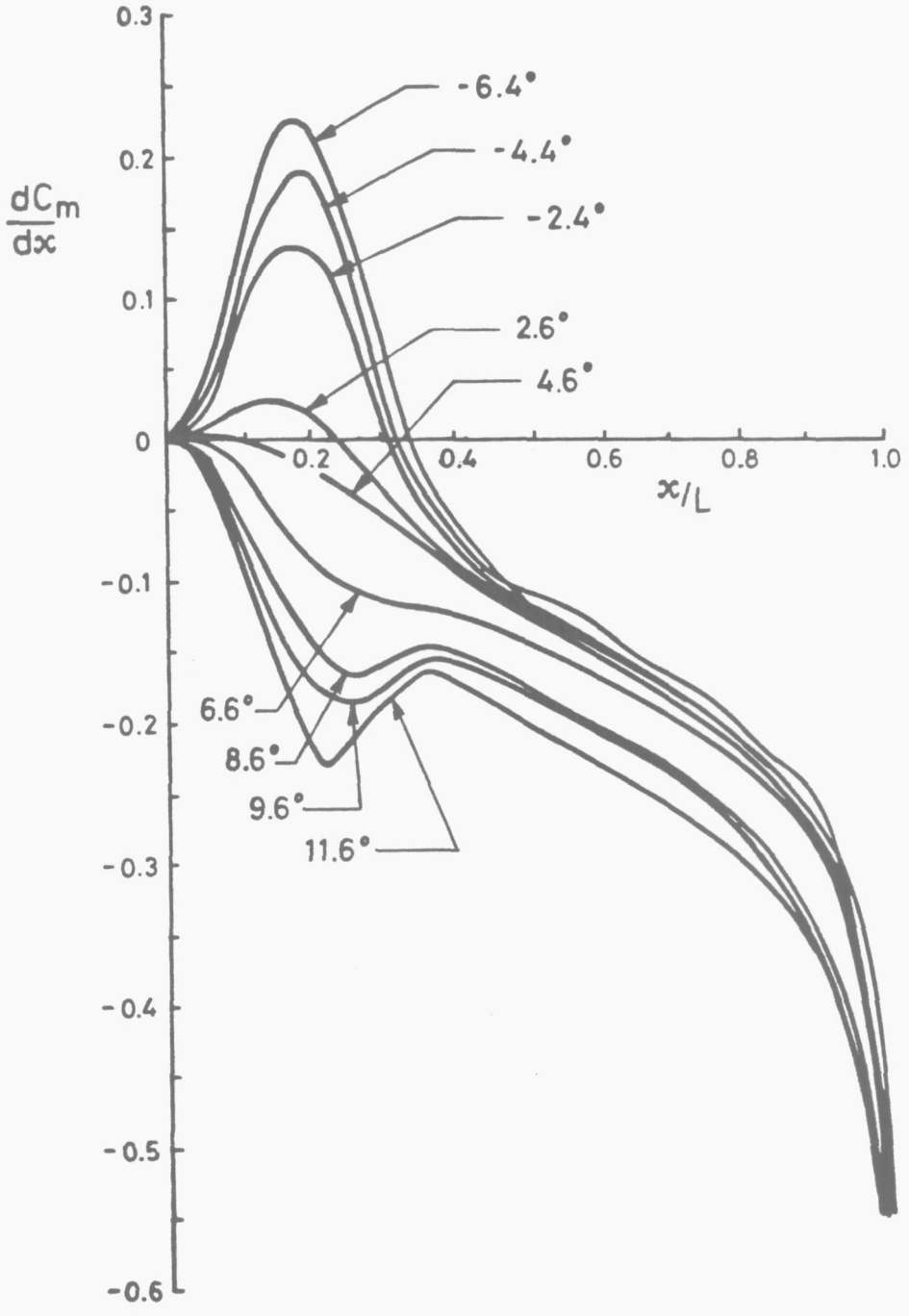

Figure 10. Variation of pitching moment loading with pitch angle.

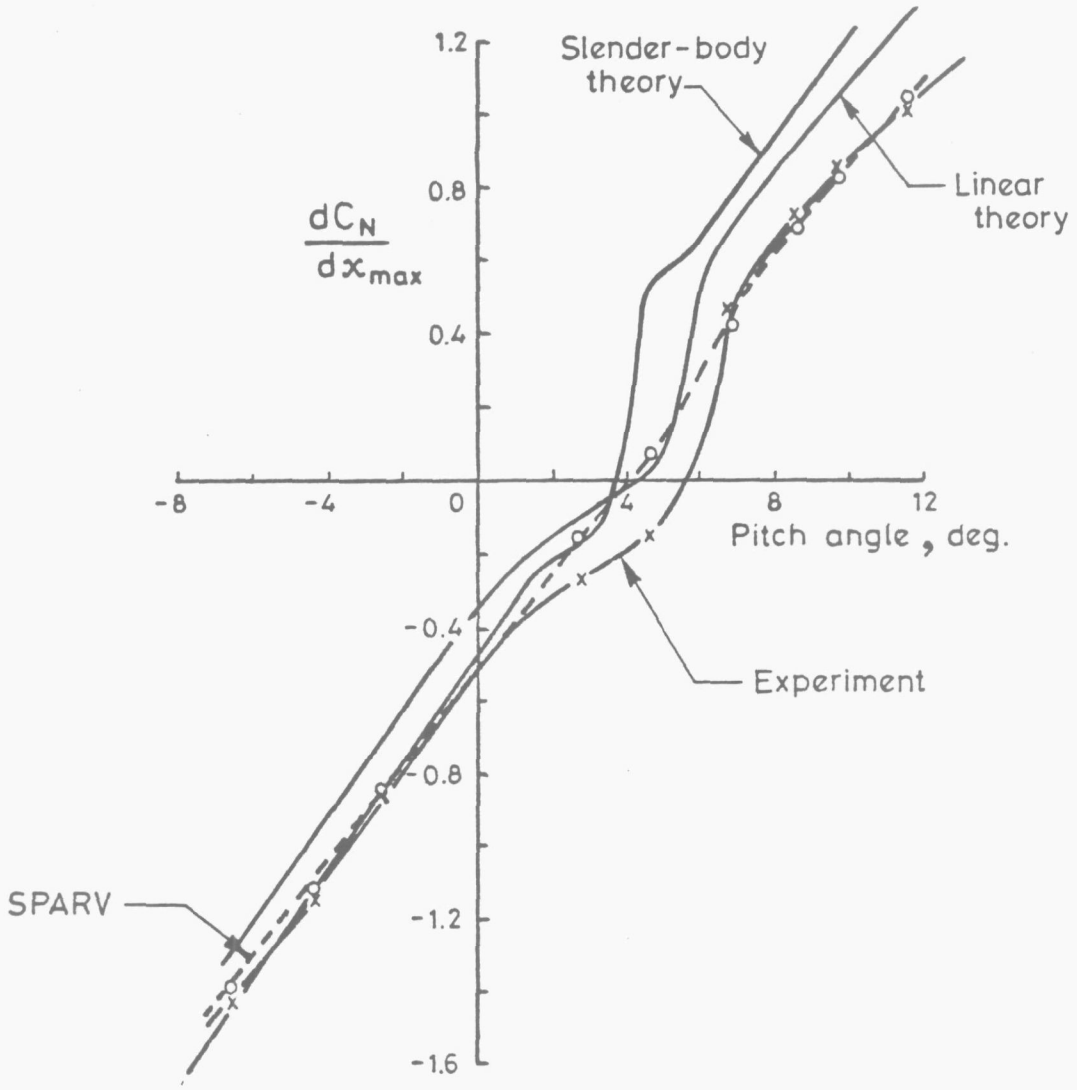

Figure 11. Variation of $\left(\frac{dC_N}{dx}\right)_{max}$ with pitch angle.

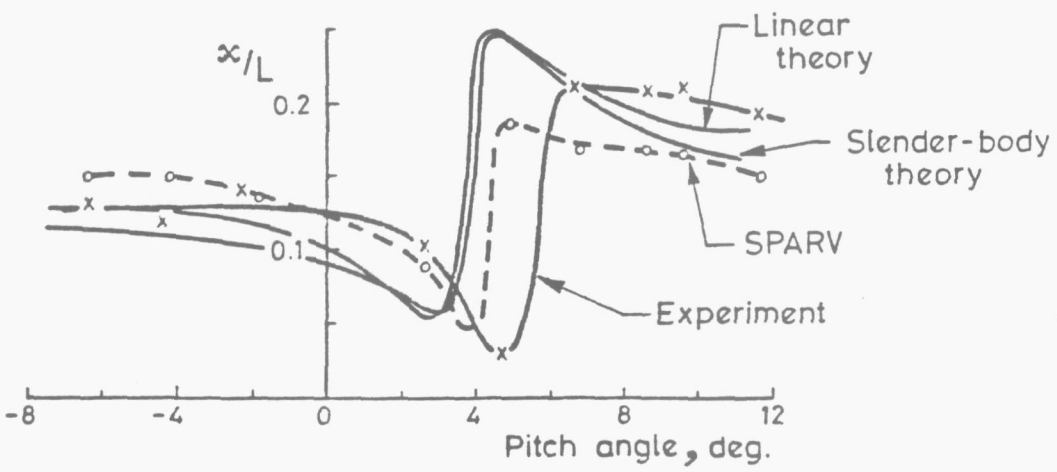

Figure 12. Variation of the position of $\left(\frac{dC_N}{dx}\right)_{max}$ with pitch angle.

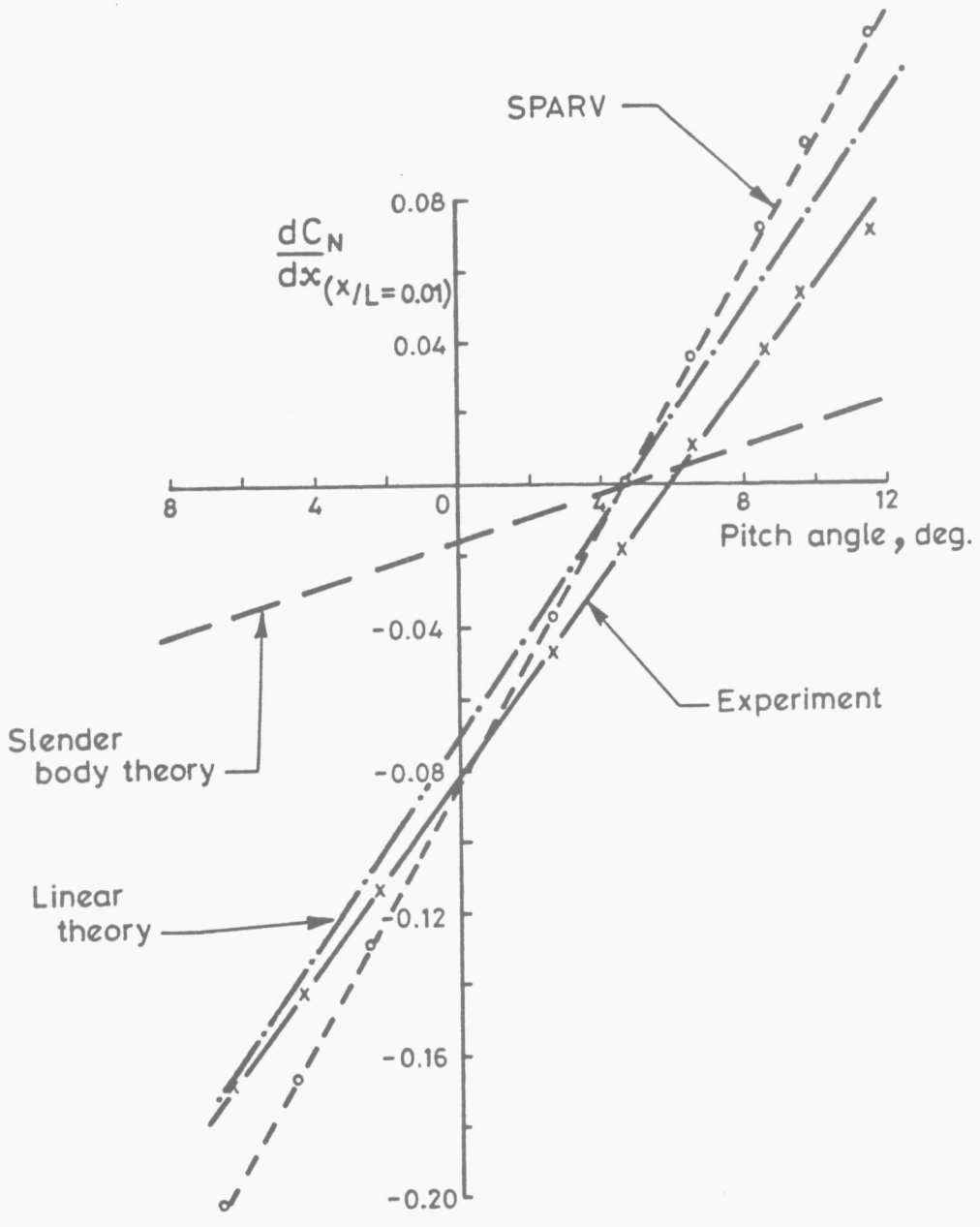

Figure 13. Variation of $\frac{dC_N}{dx}$ at $x/L = 0.01$ with pitch angle.

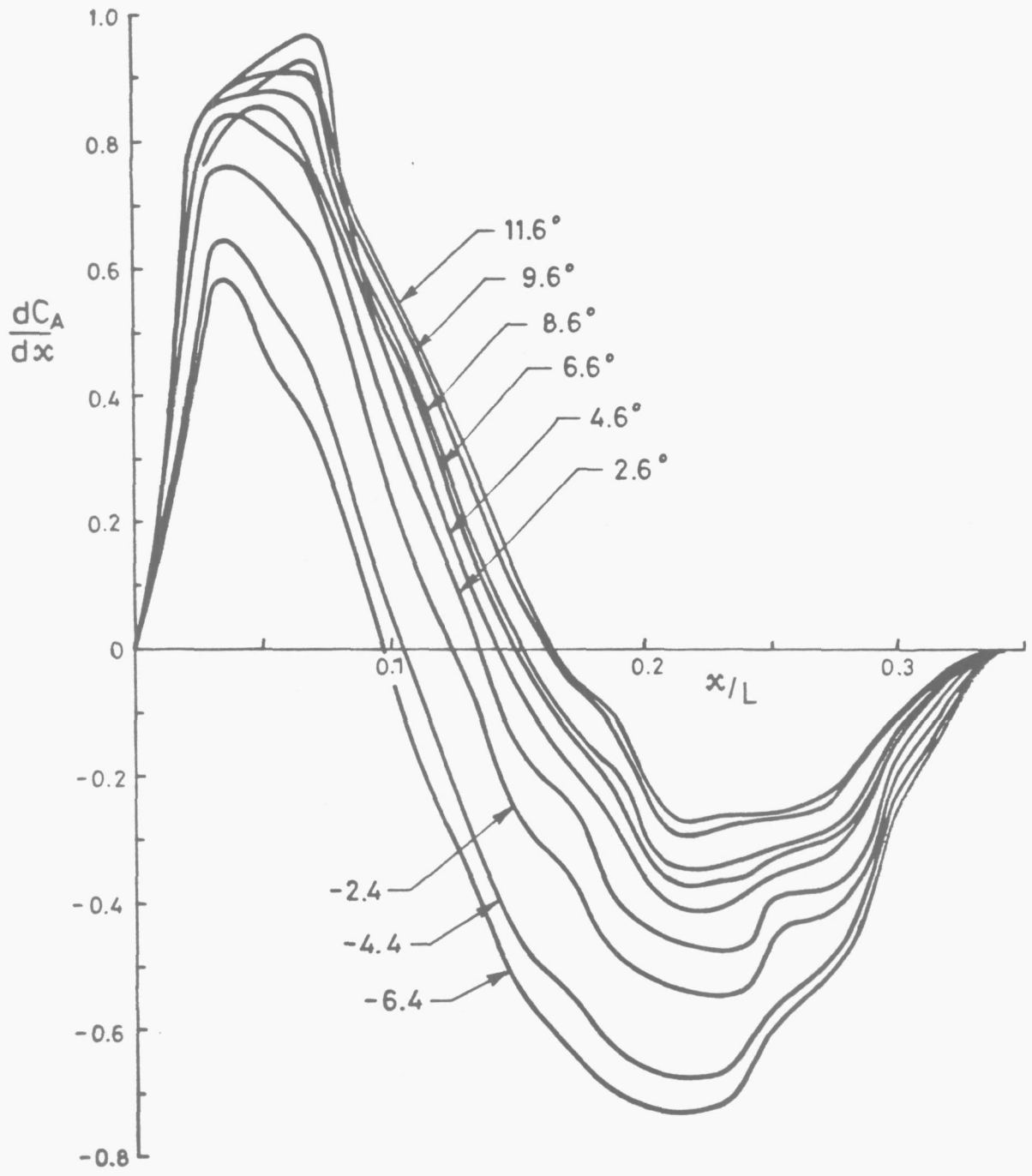

Figure 14. Variation of axial force loading distributio with pitch angle.

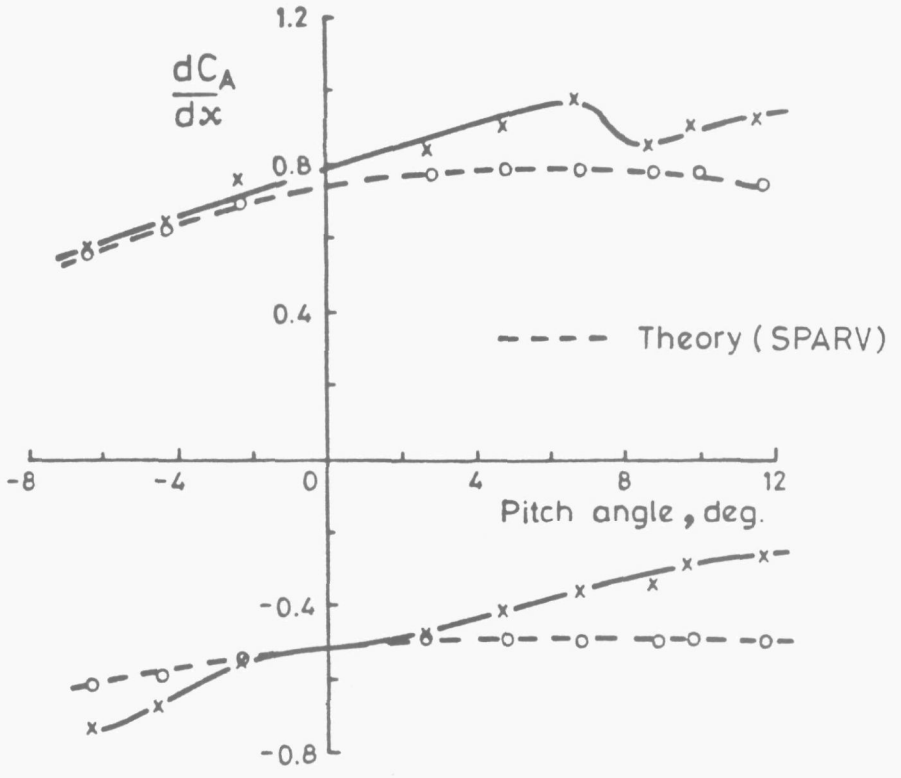

Figure 15. Variation of maximum and minimum values of $\frac{dC_A}{dx}$ with pitch angle.

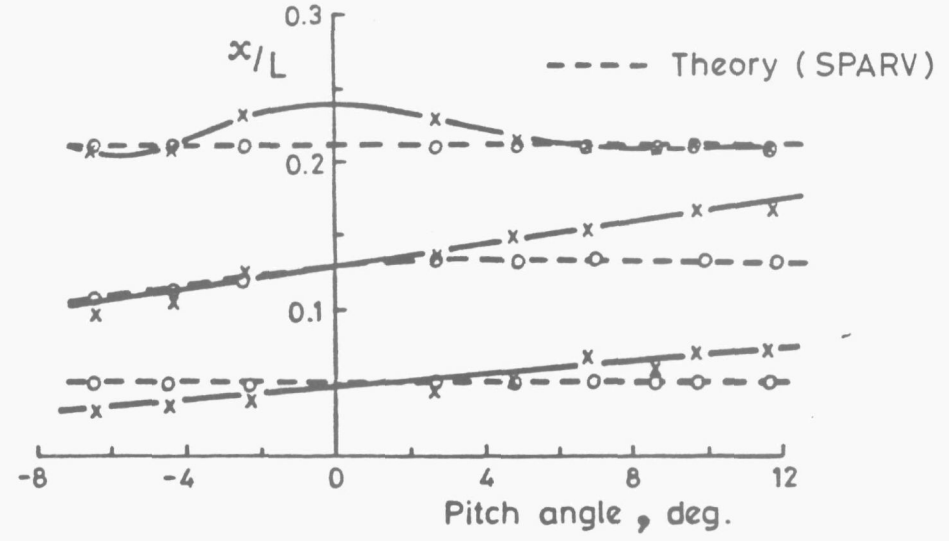

Figure 16. Variation of position of $\left(\frac{dC_A}{dx}\right)_{max}$, $\left(\frac{dC_A}{dx}\right)_{min}$ and $\left(\frac{dC_A}{dx}\right)_0$ with pitch angle.

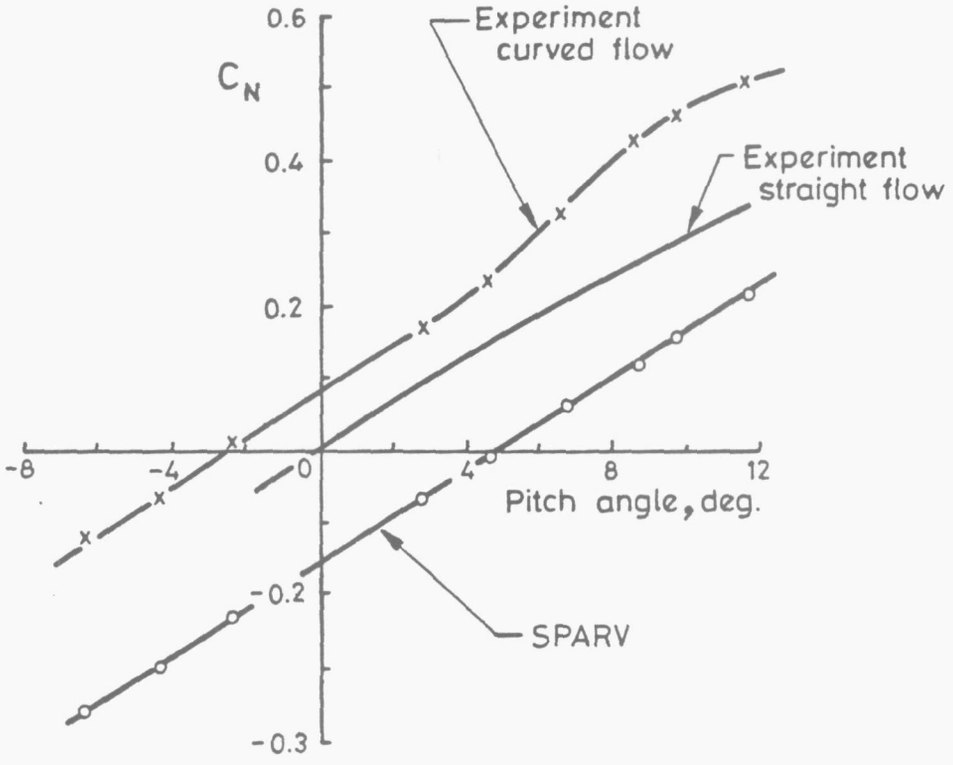

Figure 17. Variation of C_N with pitch angle.

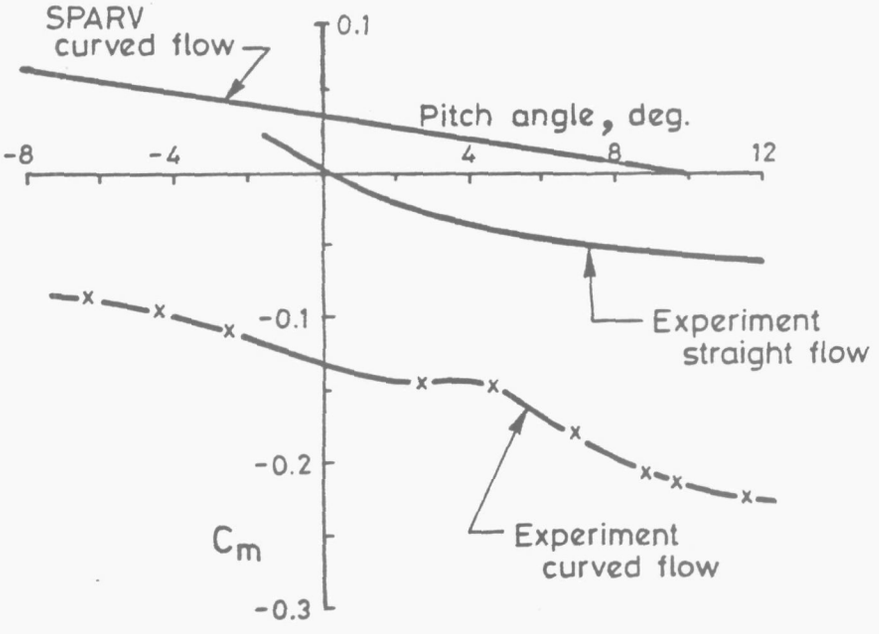

Figure 18. Variation of C_m with pitch angle.

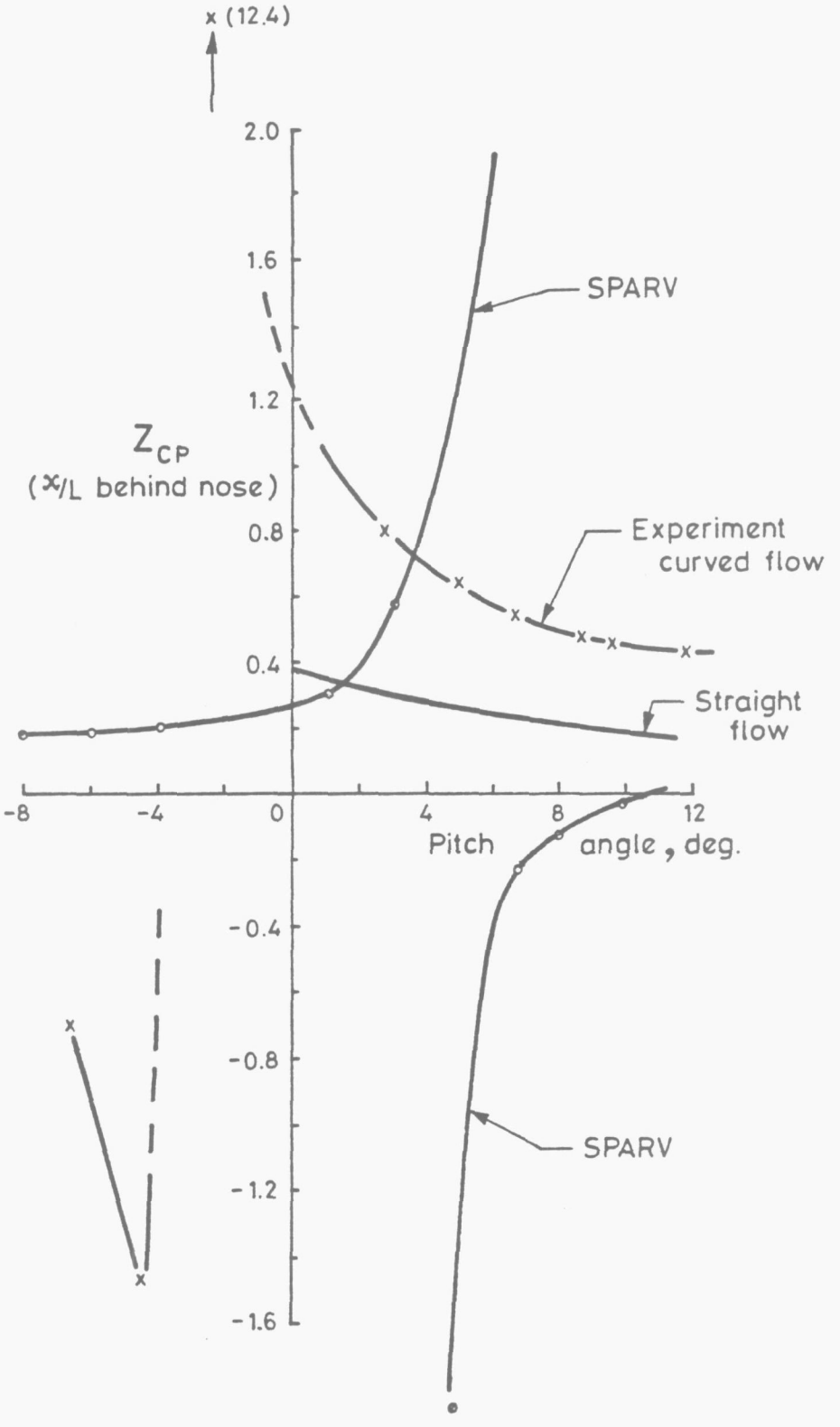

Figure 19. Variation of centre of pressure with pitch angle.

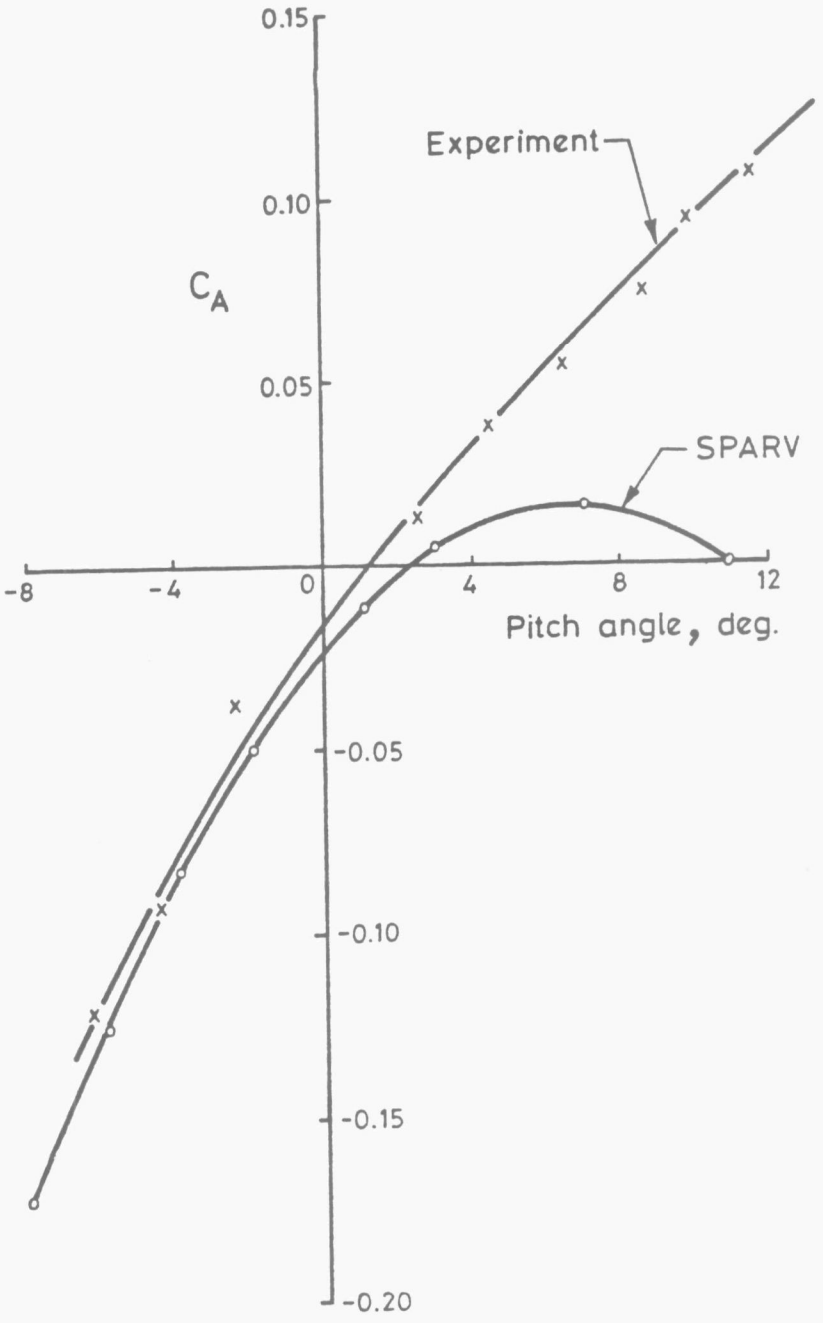

Figure 20. Variation of C_A with pitch angle.

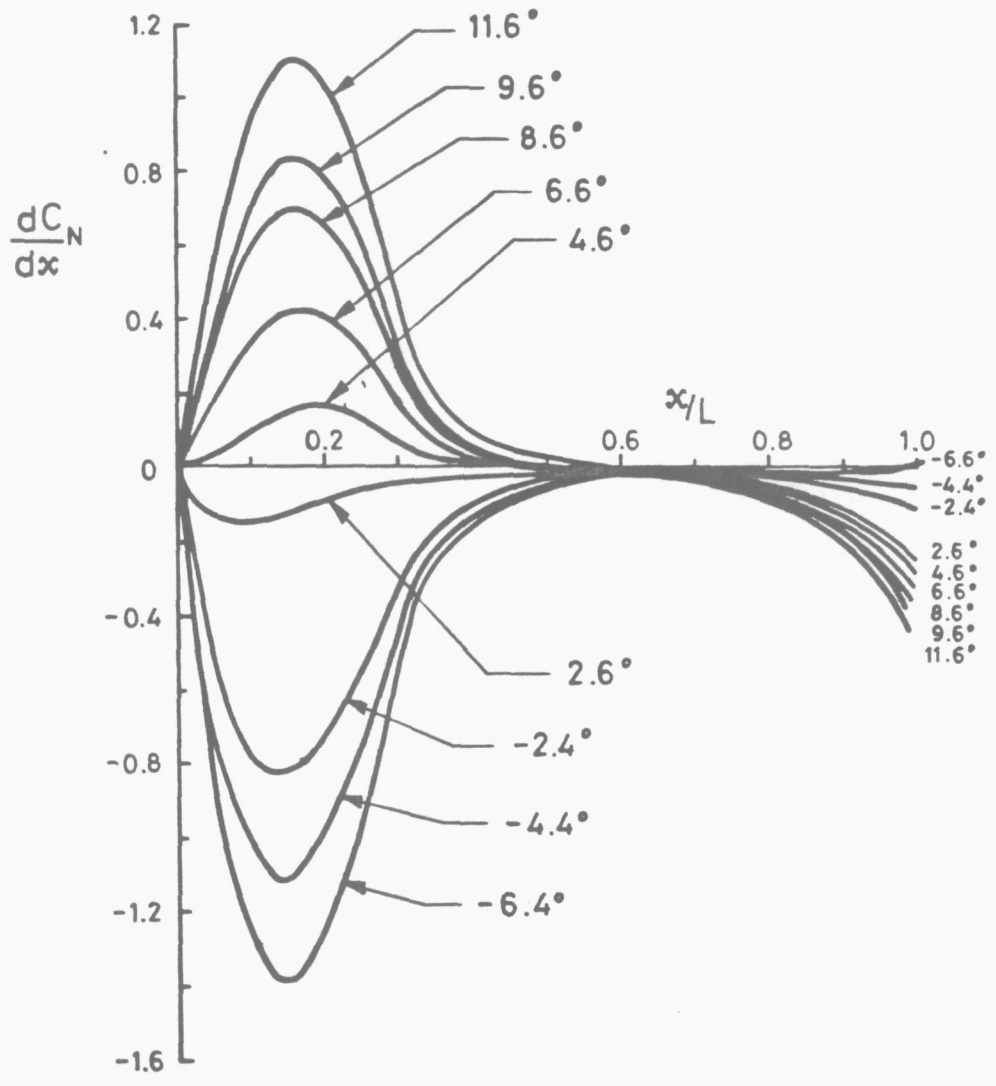

Figure 21. Theoretical estimate :- variation of normal force loading with pitch angle.

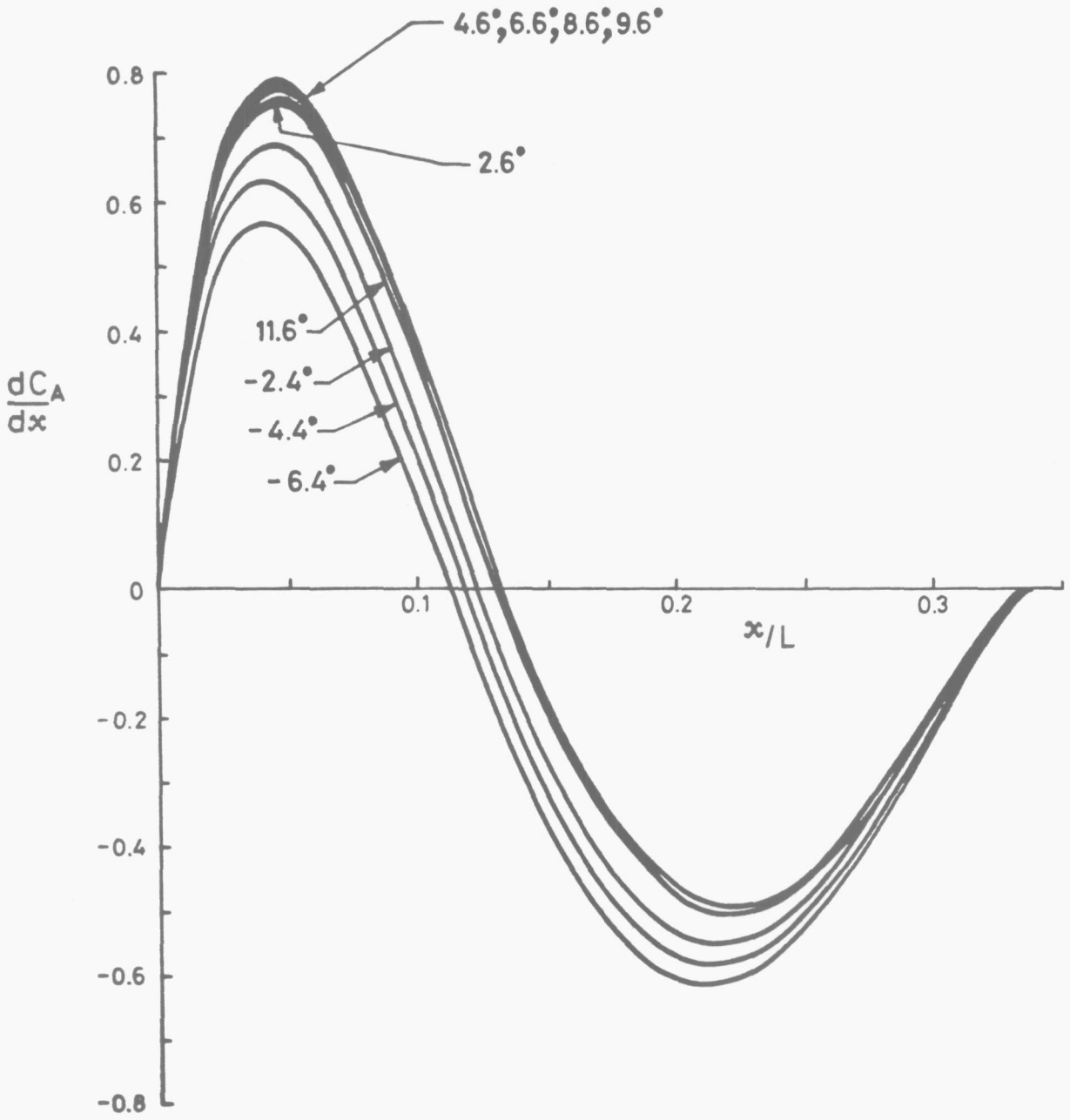

Figure 22. Theoretical estimates :- variation of axial loading with pitch angle.

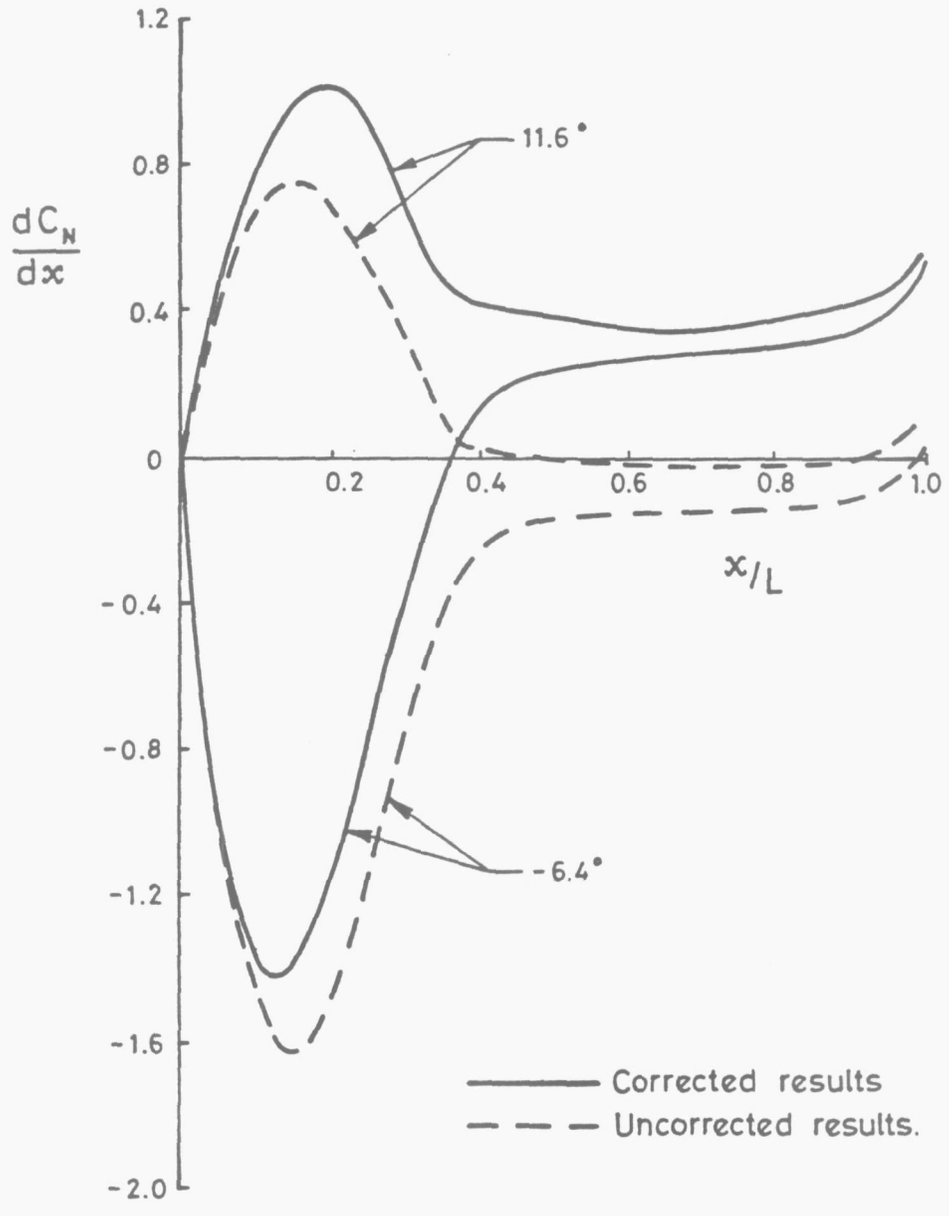

Figure 23. Effect of centrifugal correction on $\frac{dC_N}{dx}$ loading distribution.

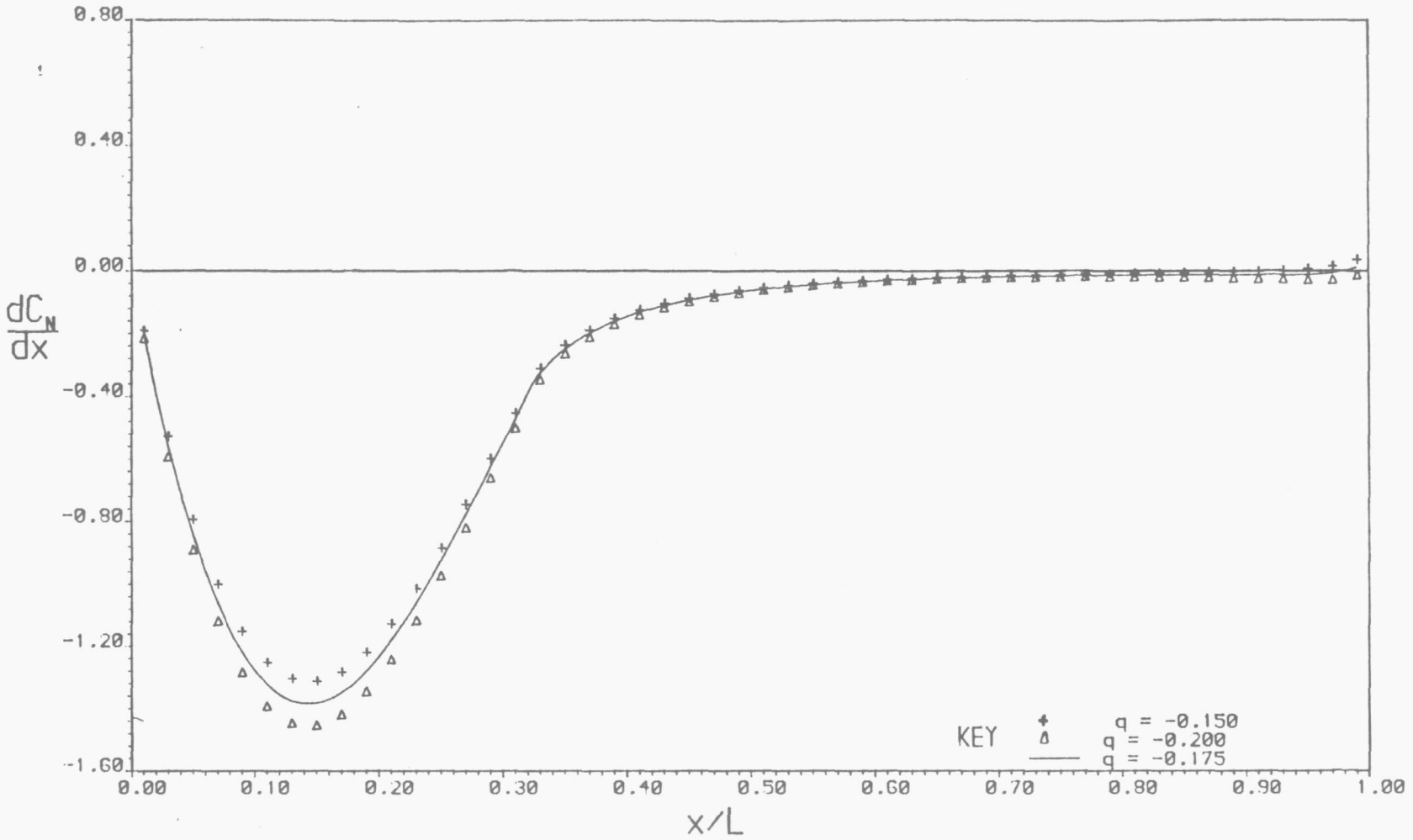

Figure 24. Variation of dC_N/dx with x/L. Pitch = -6.4 degrees
Effect of altering flow curvature.
Ogive-cylinder body in curved flow

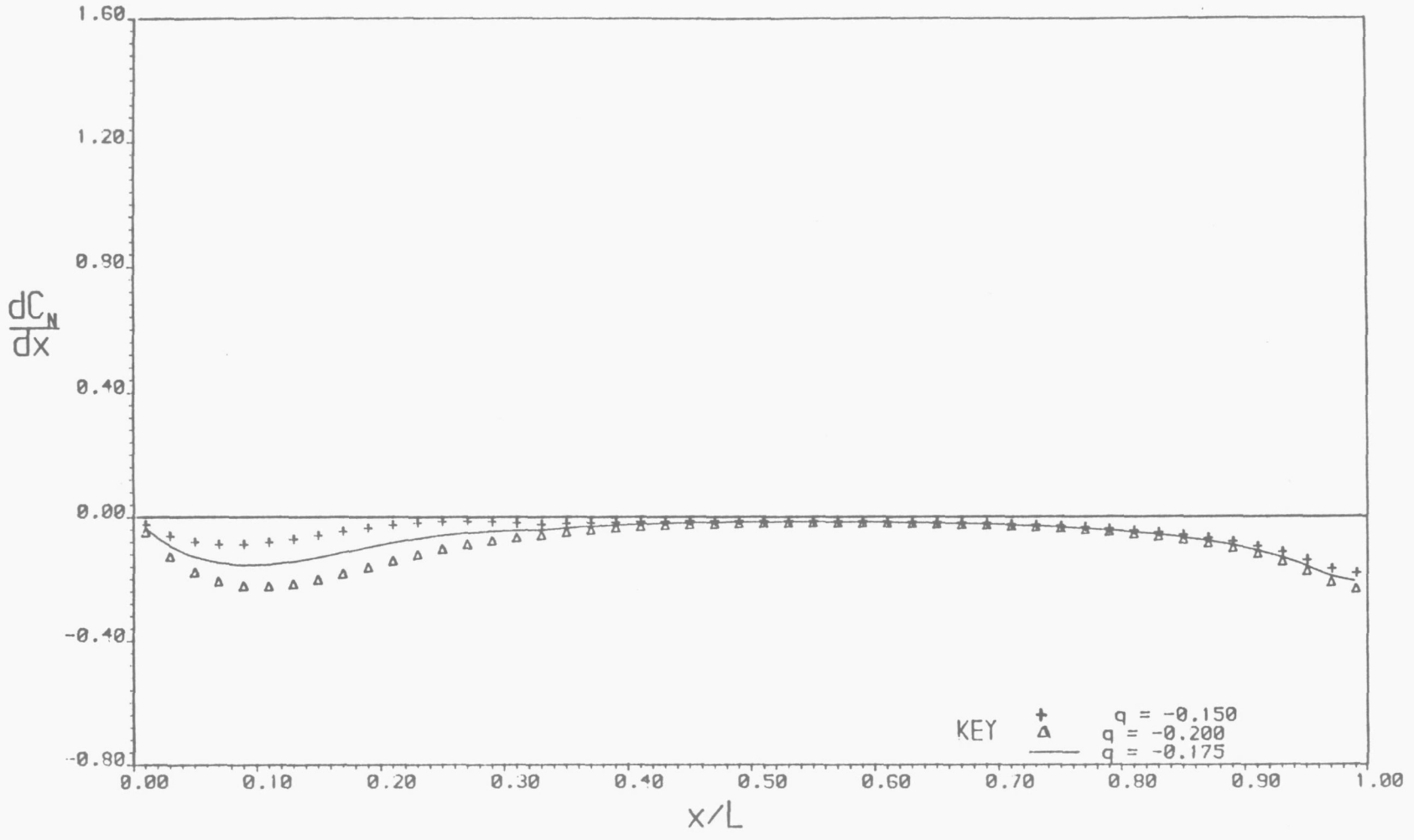

Figure 25. Variation of dC_N/dx with x/L. Pitch = 2.6 degrees
Effect of altering flow curvature.
Ogive-cylinder body in curved flow

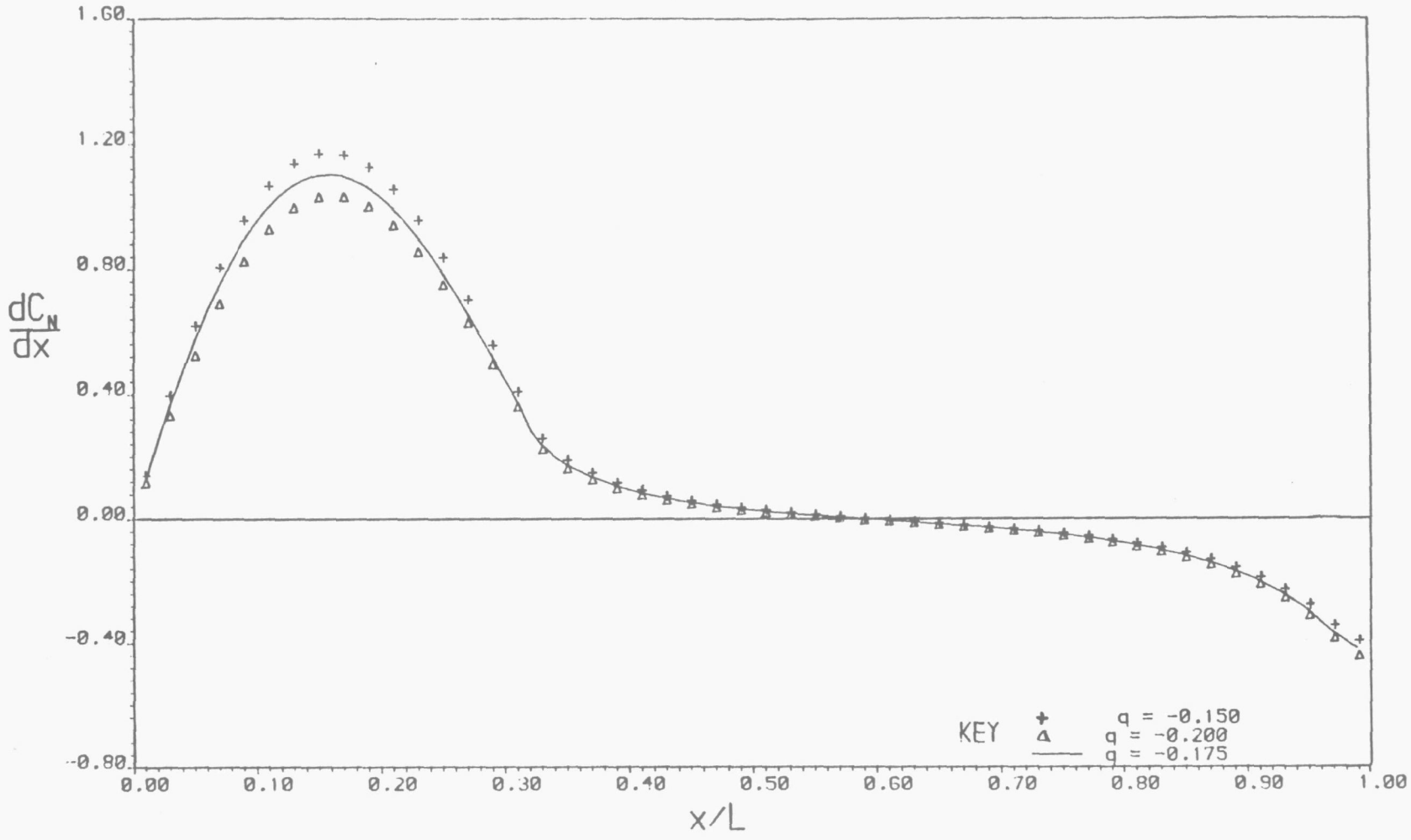

Figure 26. Variation of dC_N/dx with x/L. Pitch = 11.6 degrees
Effect of altering flow curvature.
Ogive-cylinder body in curved flow

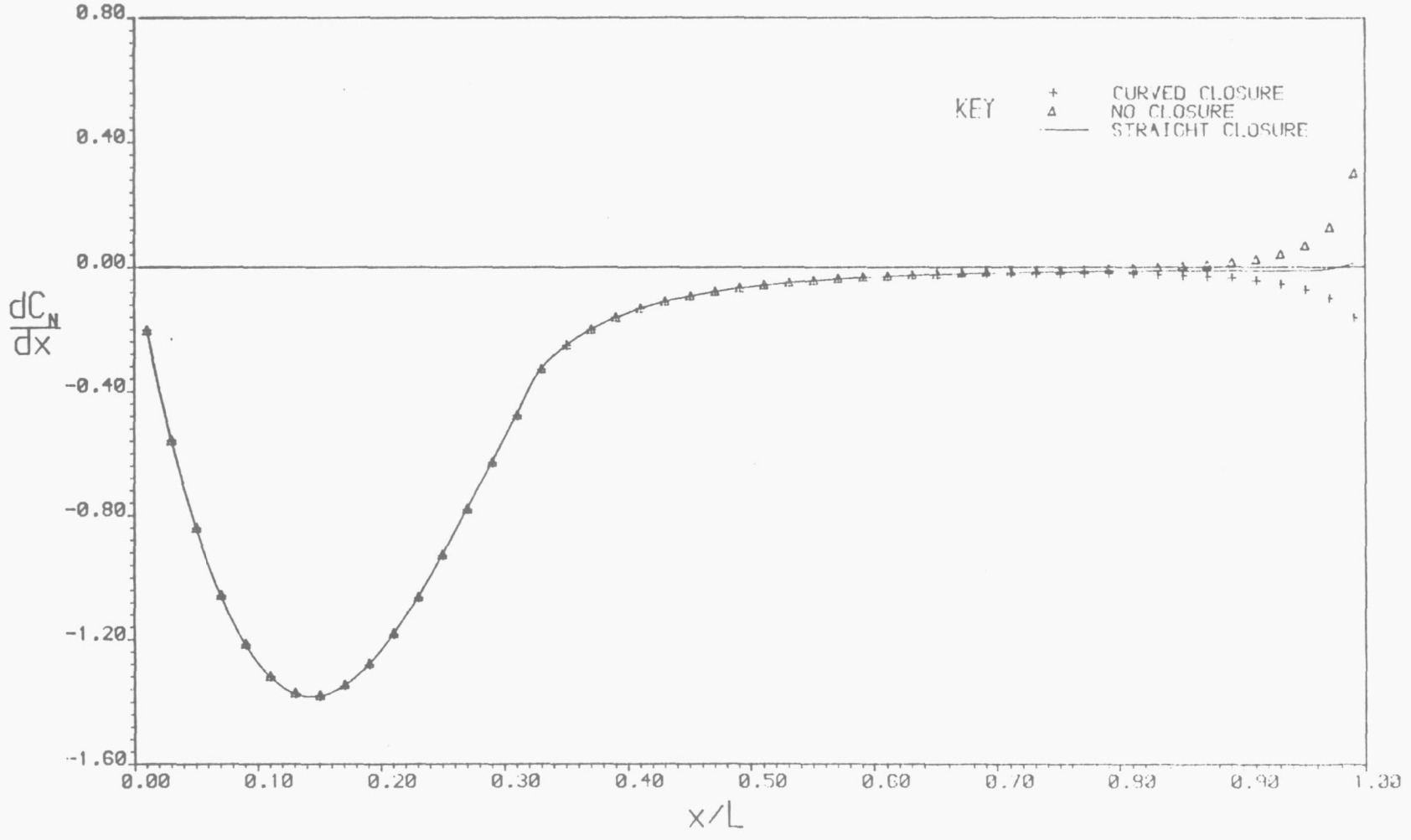

Figure 27. Variation of dC_N/dx with x/L. Pitch = -6.4 degrees
Effect of altering base closure.
Ogive-cylinder body in curved flow

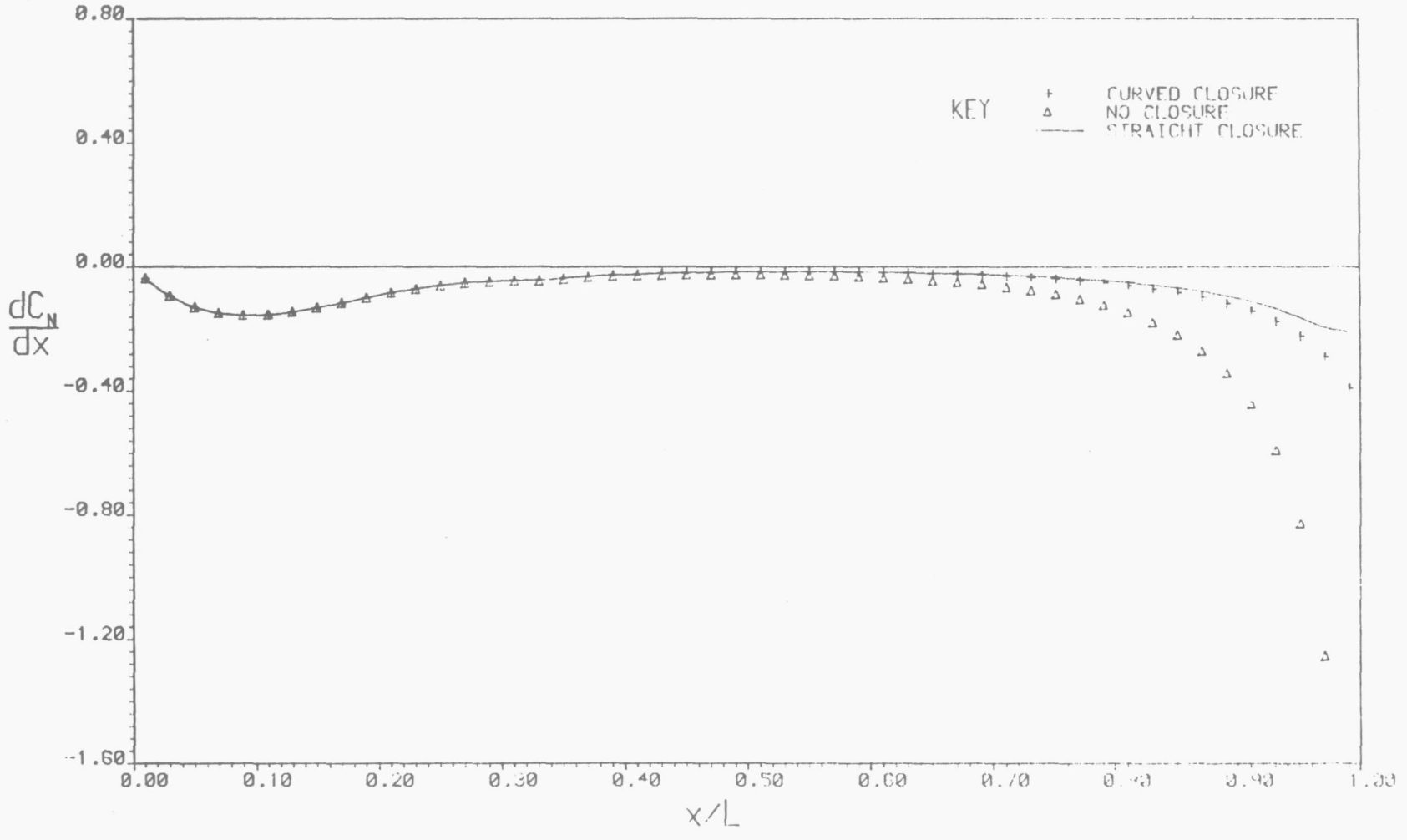

Figure 28. Variation of dC_N/dx with x/L. Pitch = 2.6 degrees
Effect of altering base closure.
Ogive-cylinder body in curved flow

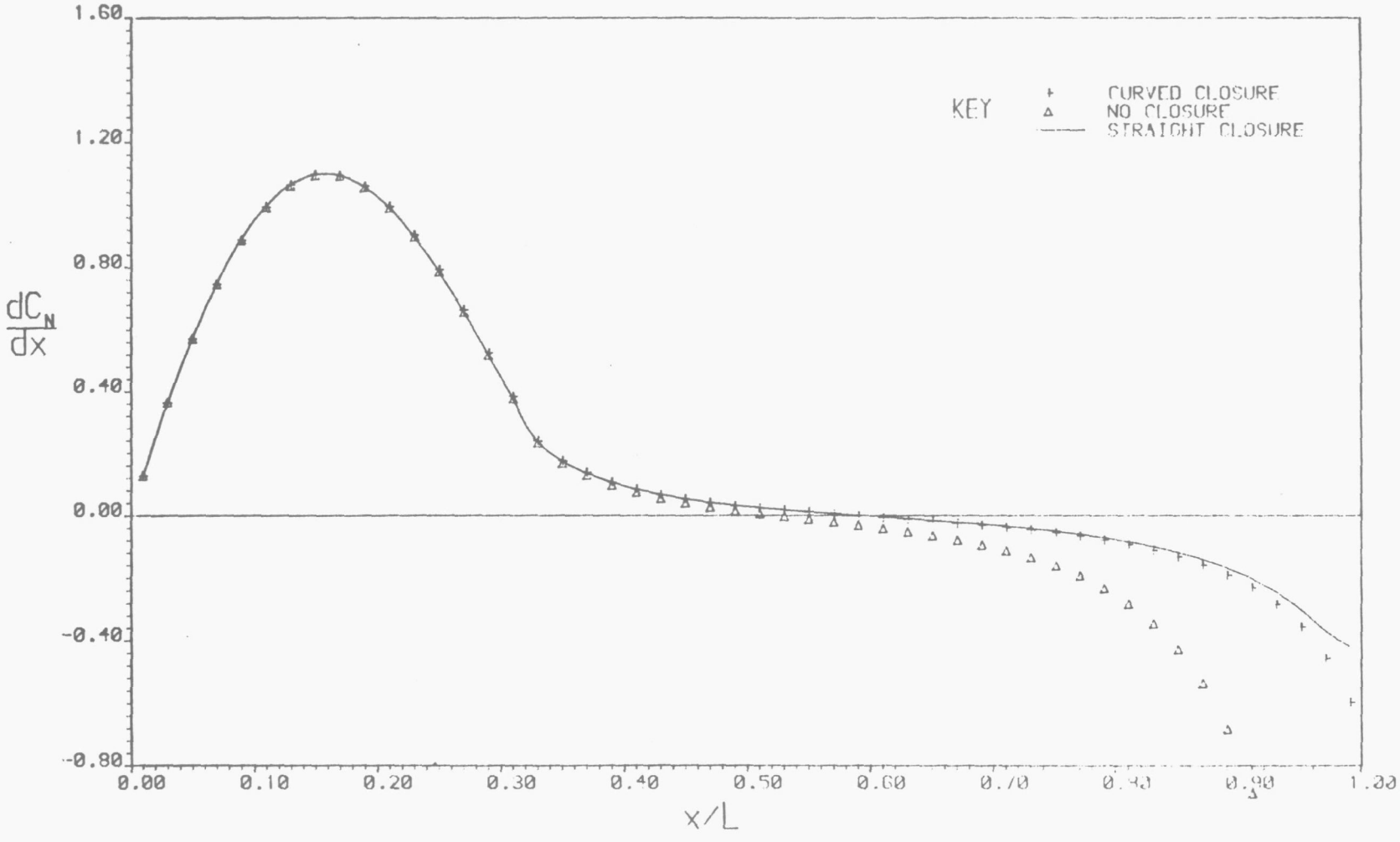

Figure 29. Variation of dC_N/dx with x/L. Pitch = 11.6 degrees
Effect of altering base closure.
Ogive-cylinder body in curved flow

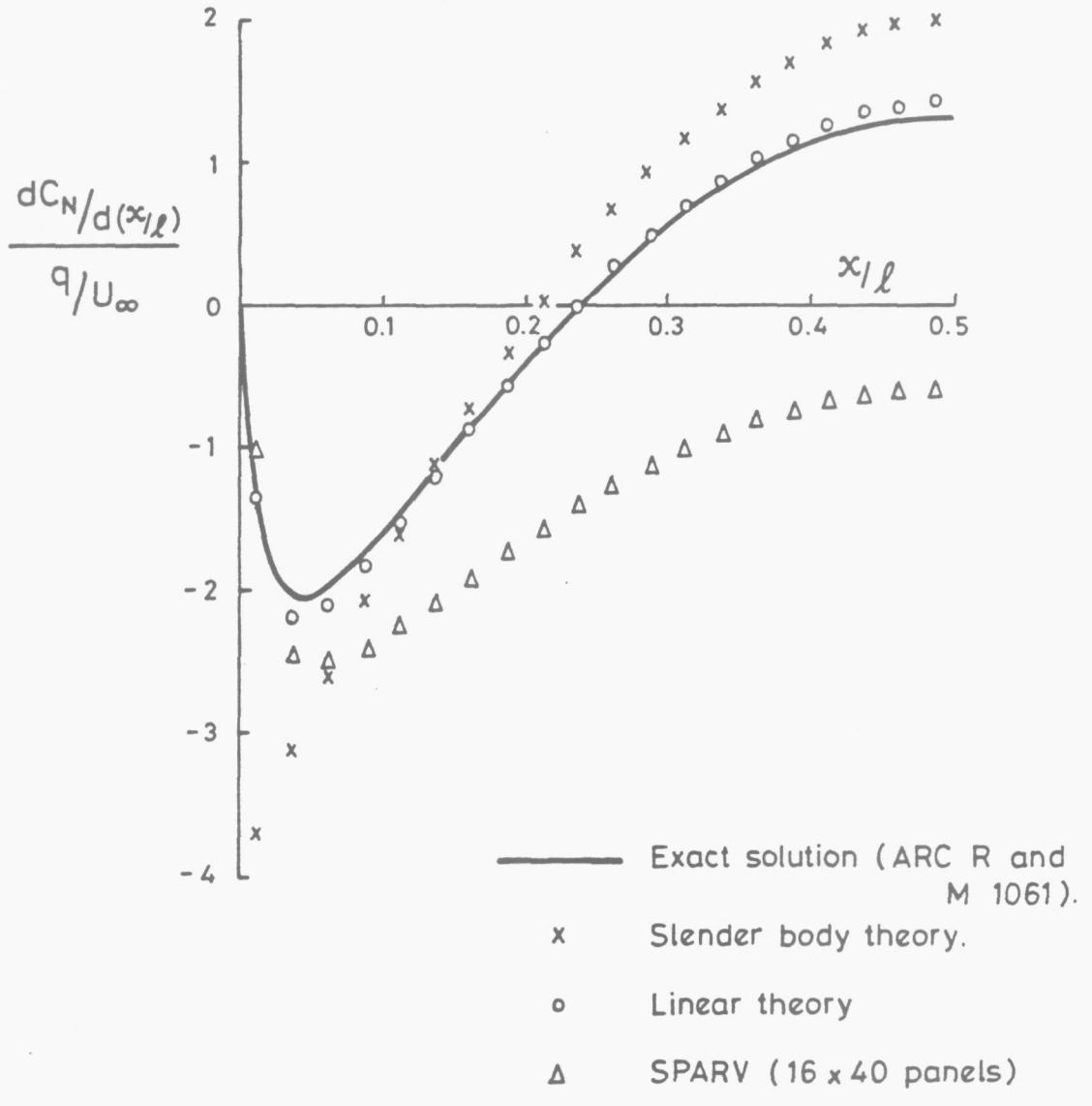

Figure 30. Comparison of various theoretical methods of calculating the load distribution over a 4:1 fineness ratio prolate spheroid.

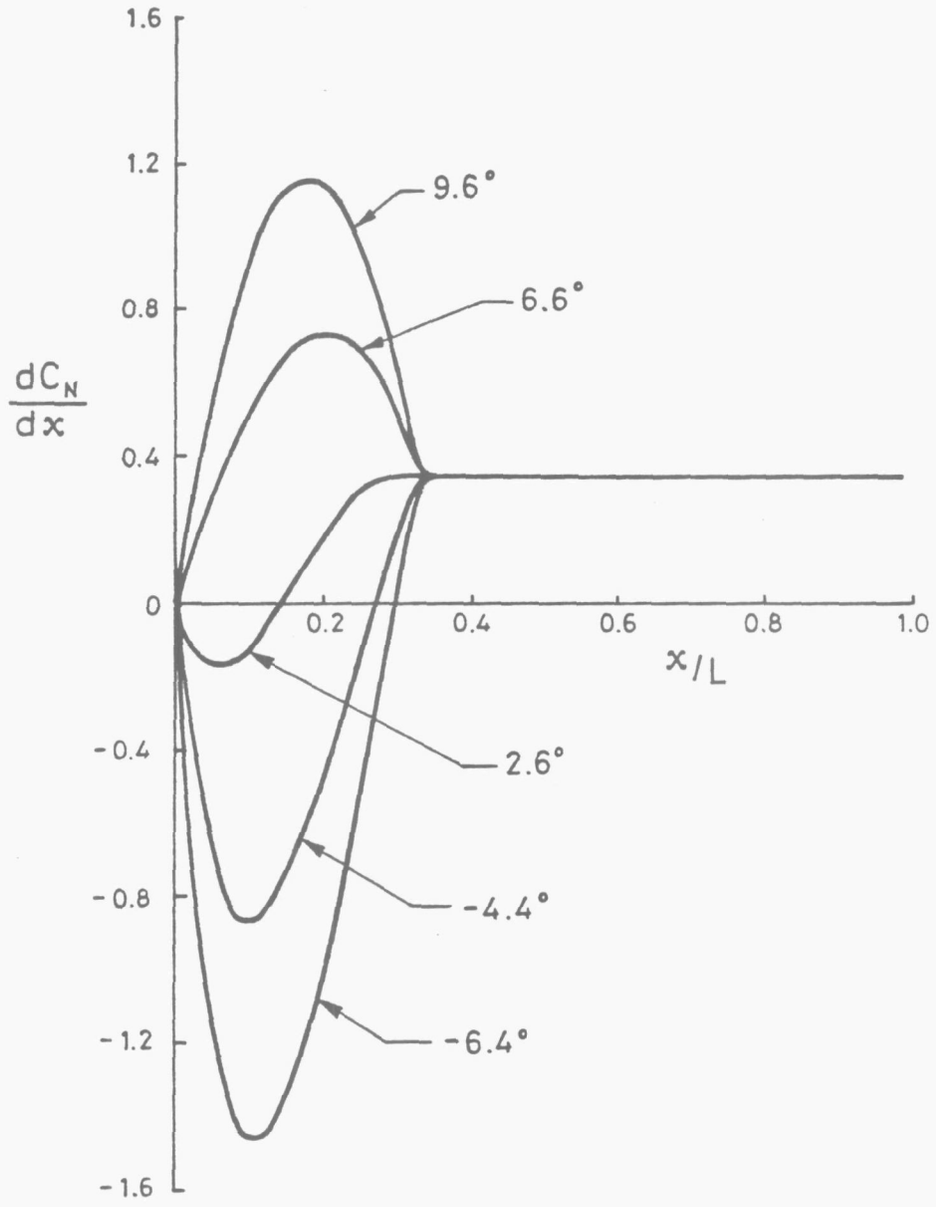

Figure 31. Slender body theory. Variation of normal-force loading with pitch angle.

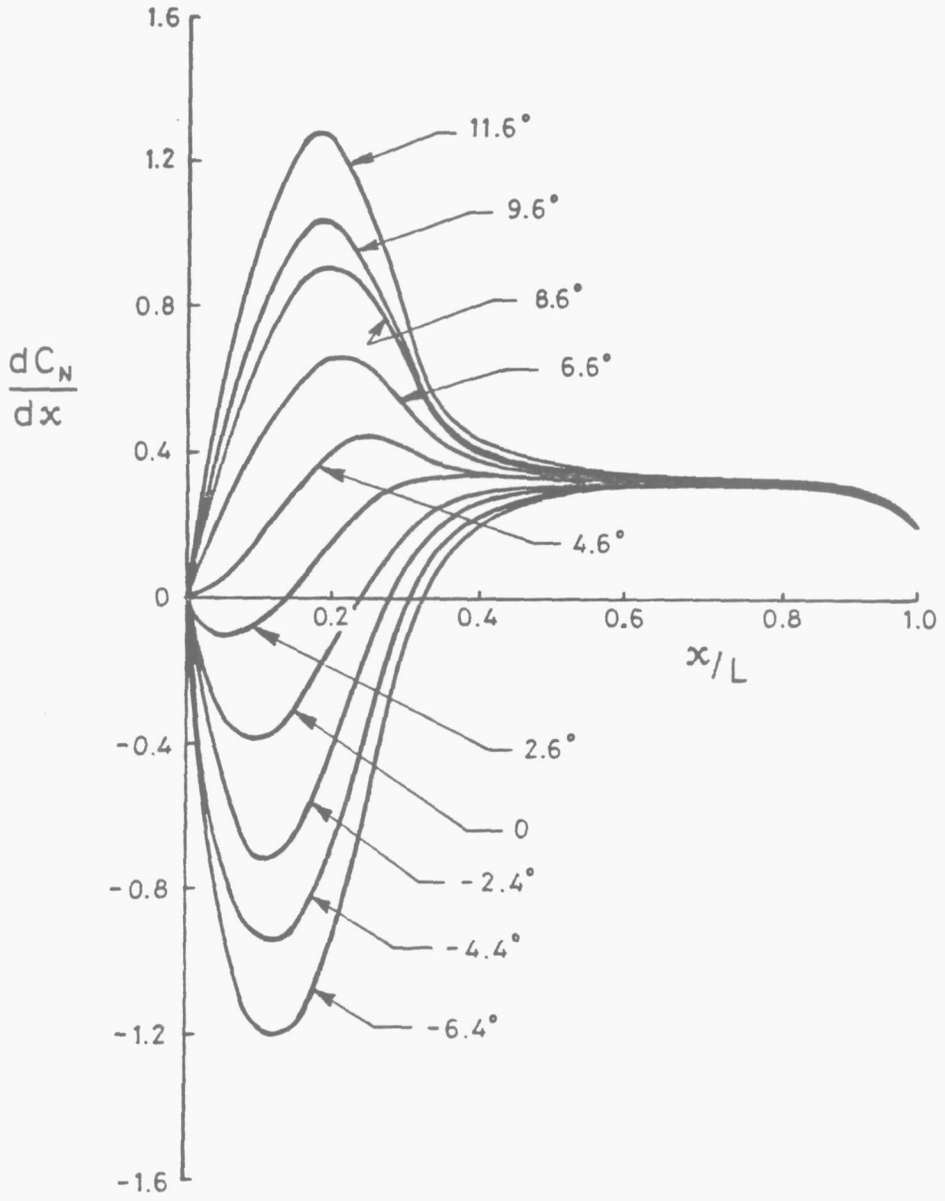

Figure 32. Linear theory. Variation of normal-force loading distribution with pitch angle.

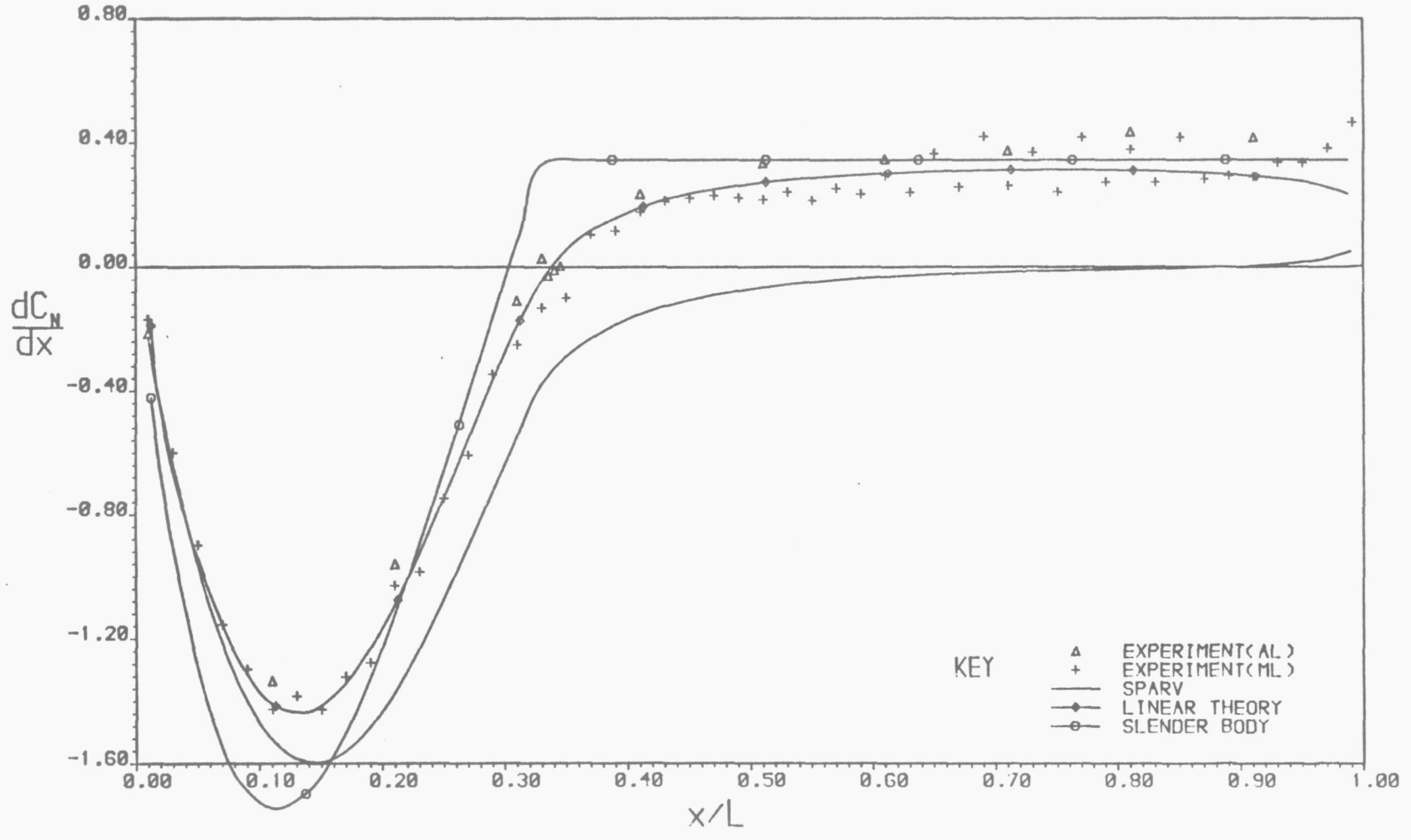

Figure 33. Ogive-cylinder body in curved flow
Comparison of experiment with theory.
Variation of dC_N/dx with x/L. Pitch = -8.0 degrees

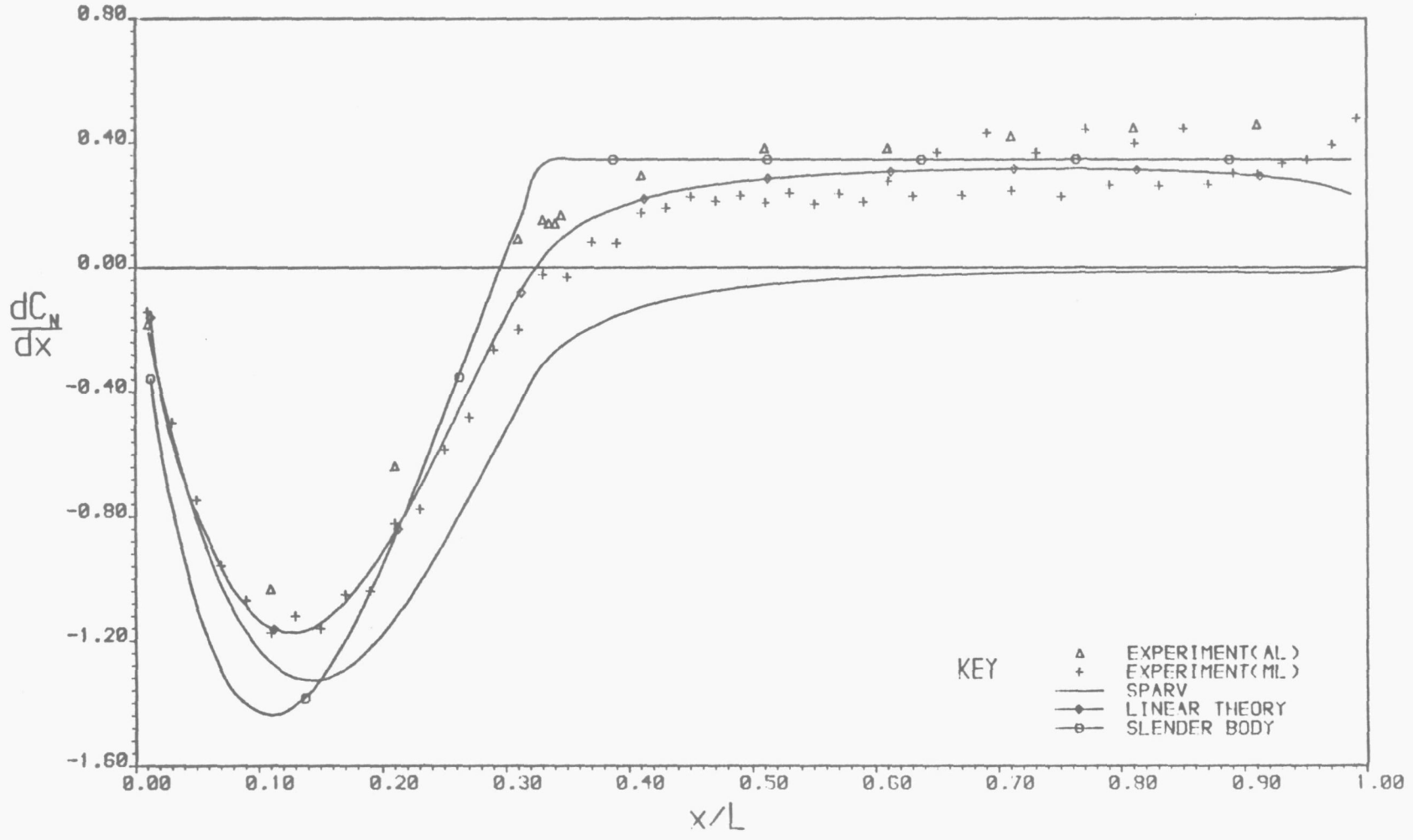

Figure 34. Ogive-cylinder body in curved flow
Comparison of experiment with theory.
Variation of dC_N/dx with x/L. Pitch = -6.0 degrees

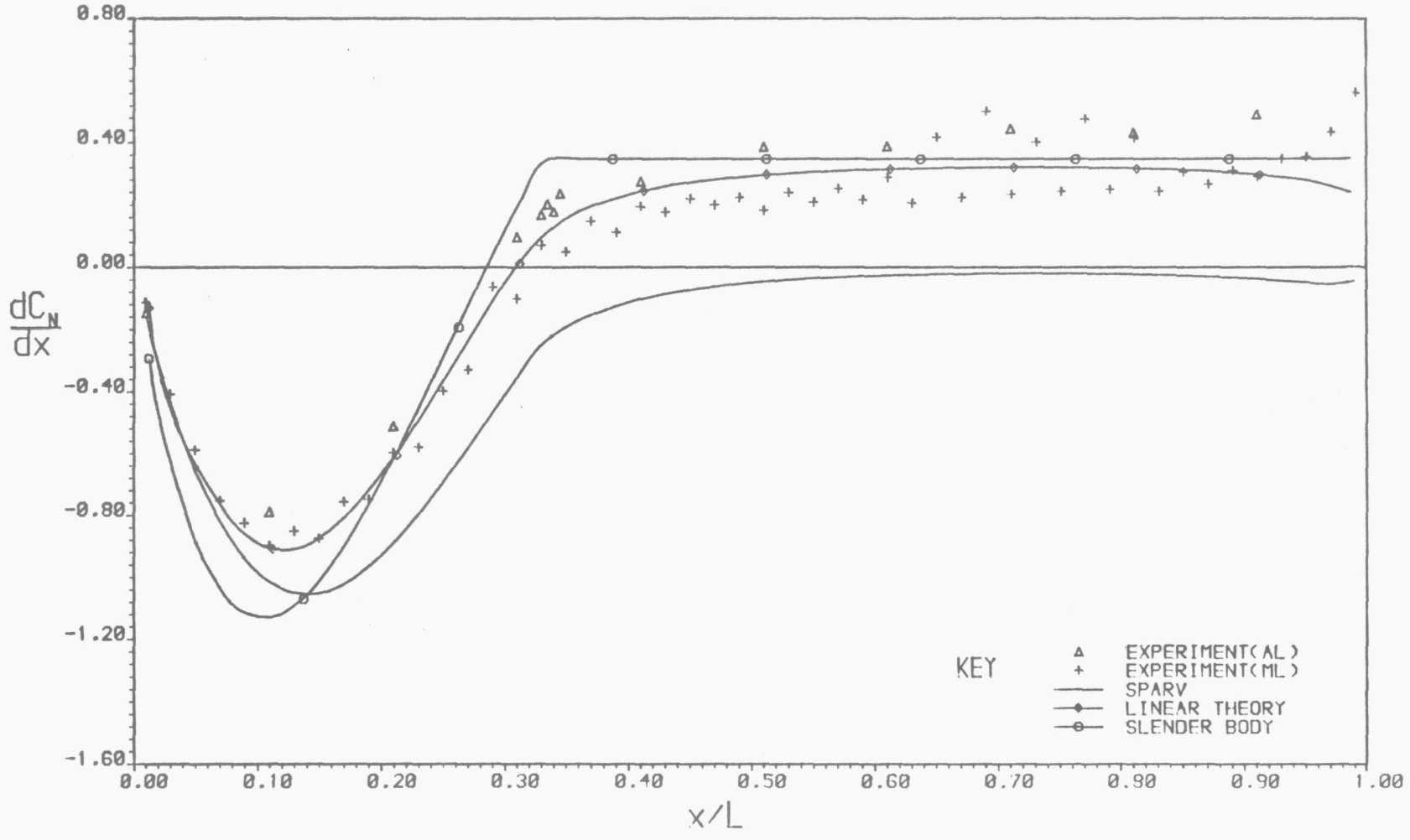

Figure 35. Ogive-cylinder body in curved flow
Comparison of experiment with theory.
Variation of dC_N/dx with x/L. Pitch = -4.0 degrees

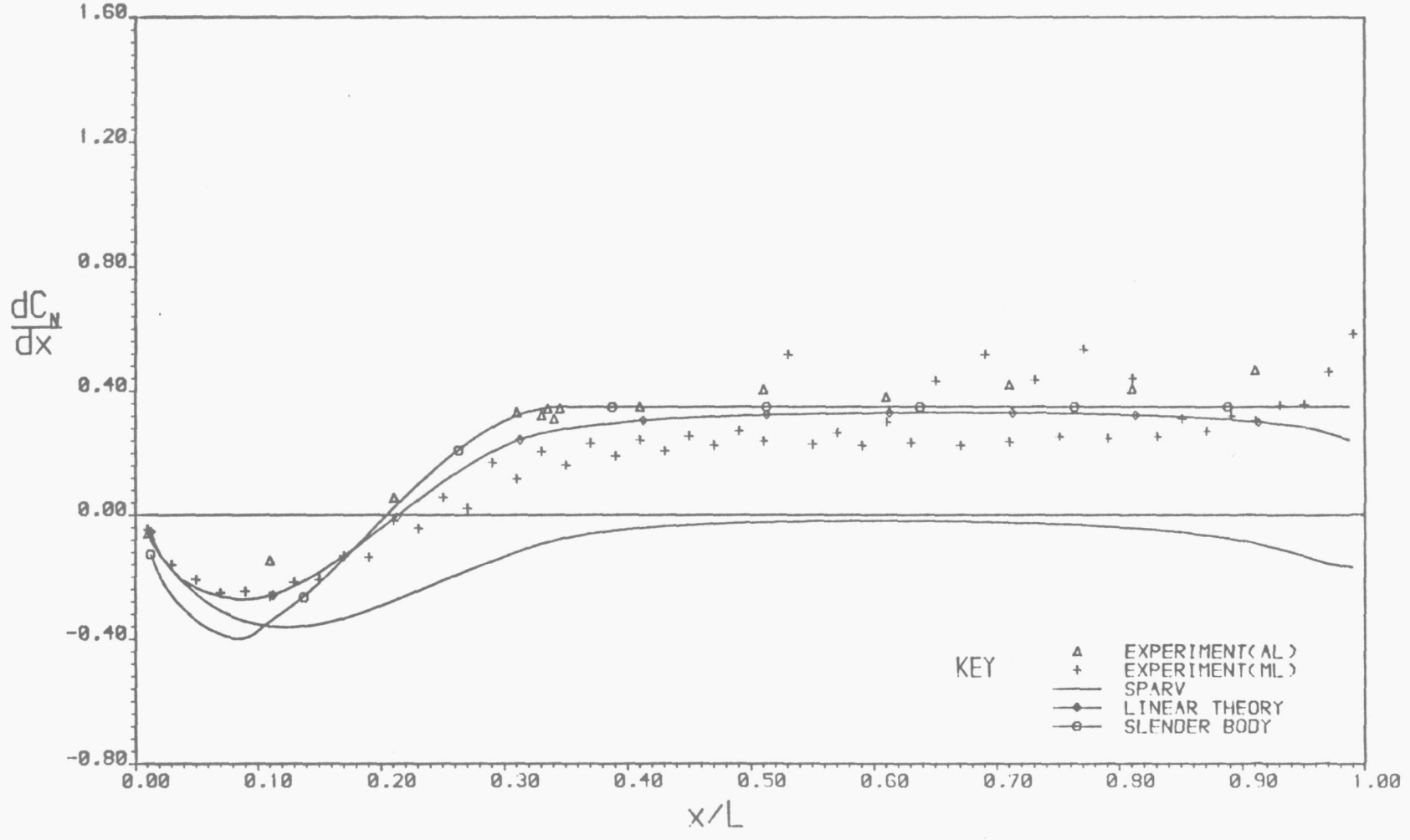

Figure 36. Ogive-cylinder body in curved flow
Comparison of experiment with theory.
Variation of dC_N/dx with x/L. Pitch = 1.0 degrees

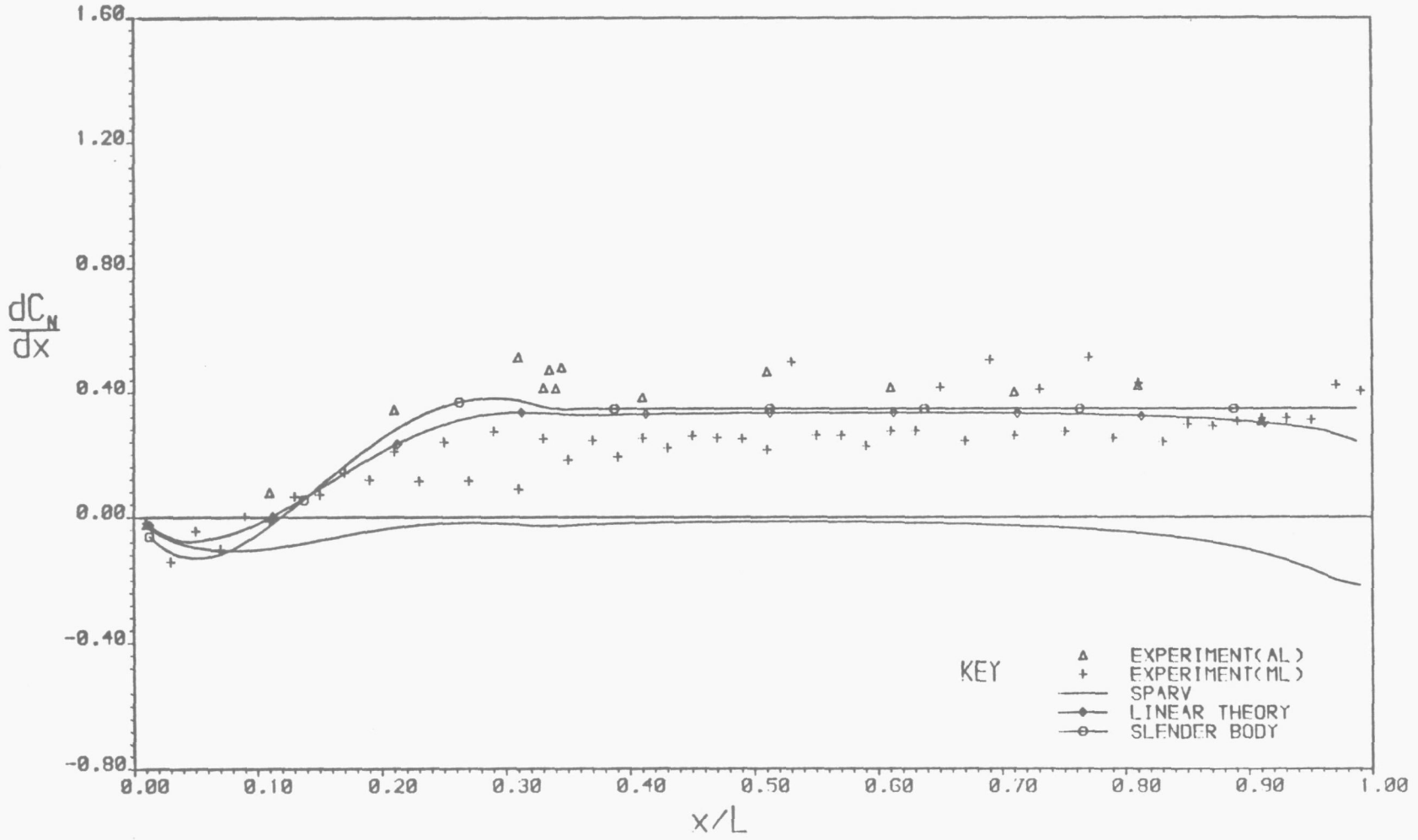

Figure 37. Ogive-cylinder body in curved flow
Comparison of experiment with theory.
Variation of dC_N/dx with x/L. Pitch = 3.0 degrees

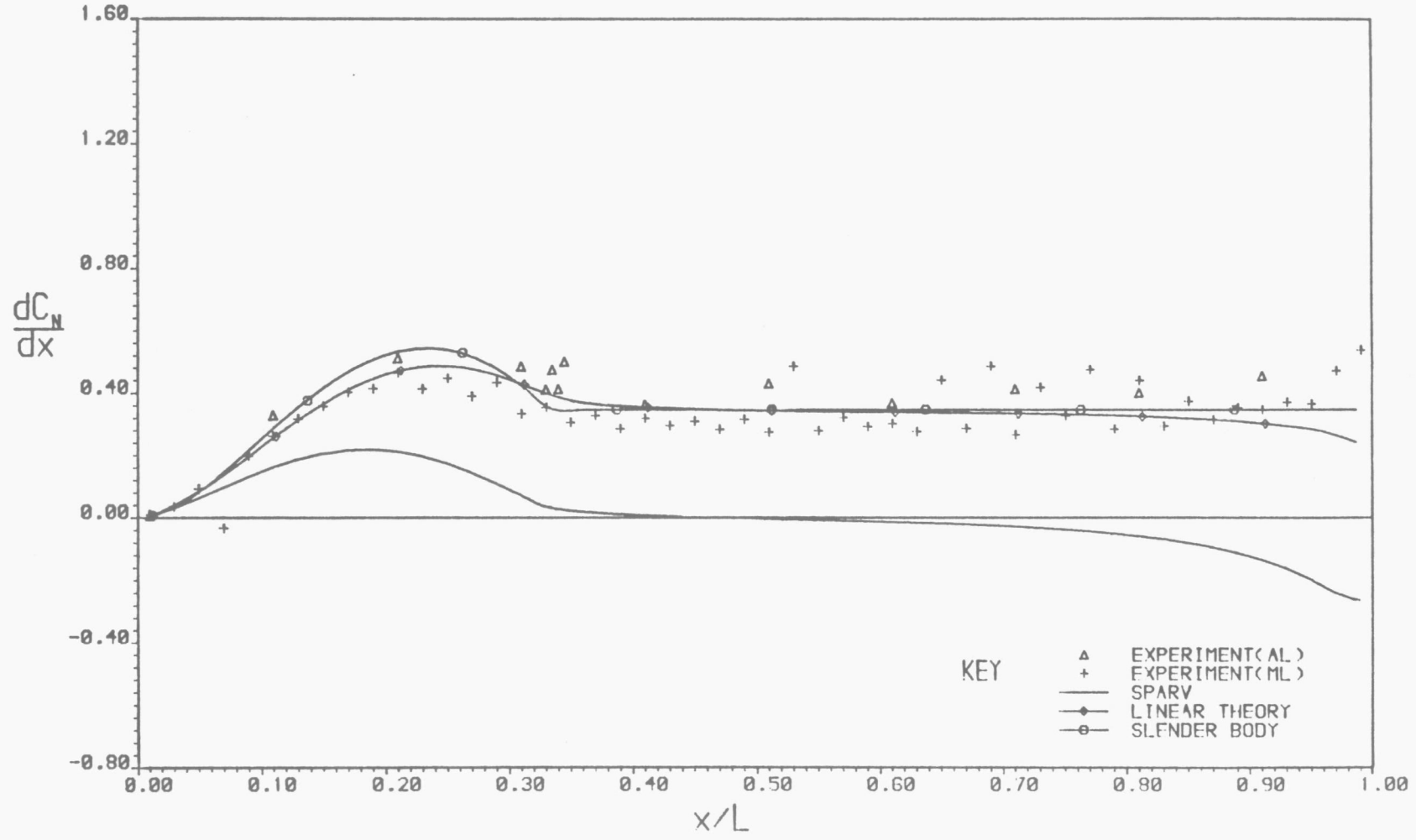

Figure 38. Ogive-cylinder body in curved flow
Comparison of experiment with theory.
Variation of dC_N/dx with x/L. Pitch = 5.0 degrees

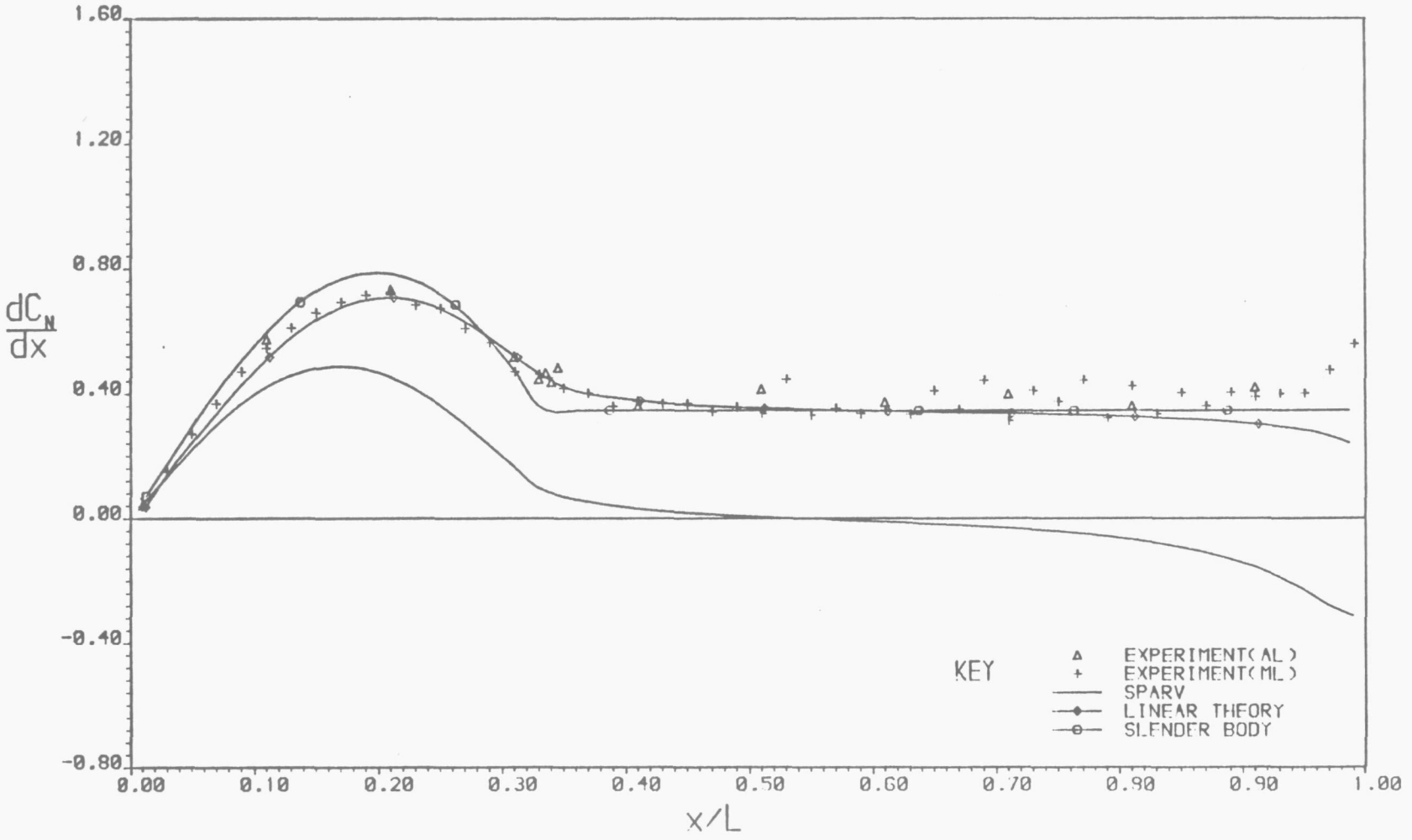

Figure 39. Ogive-cylinder body in curved flow
Comparison of experiment with theory.
Variation of dC_N/dx with x/L. Pitch = 7.0 degrees

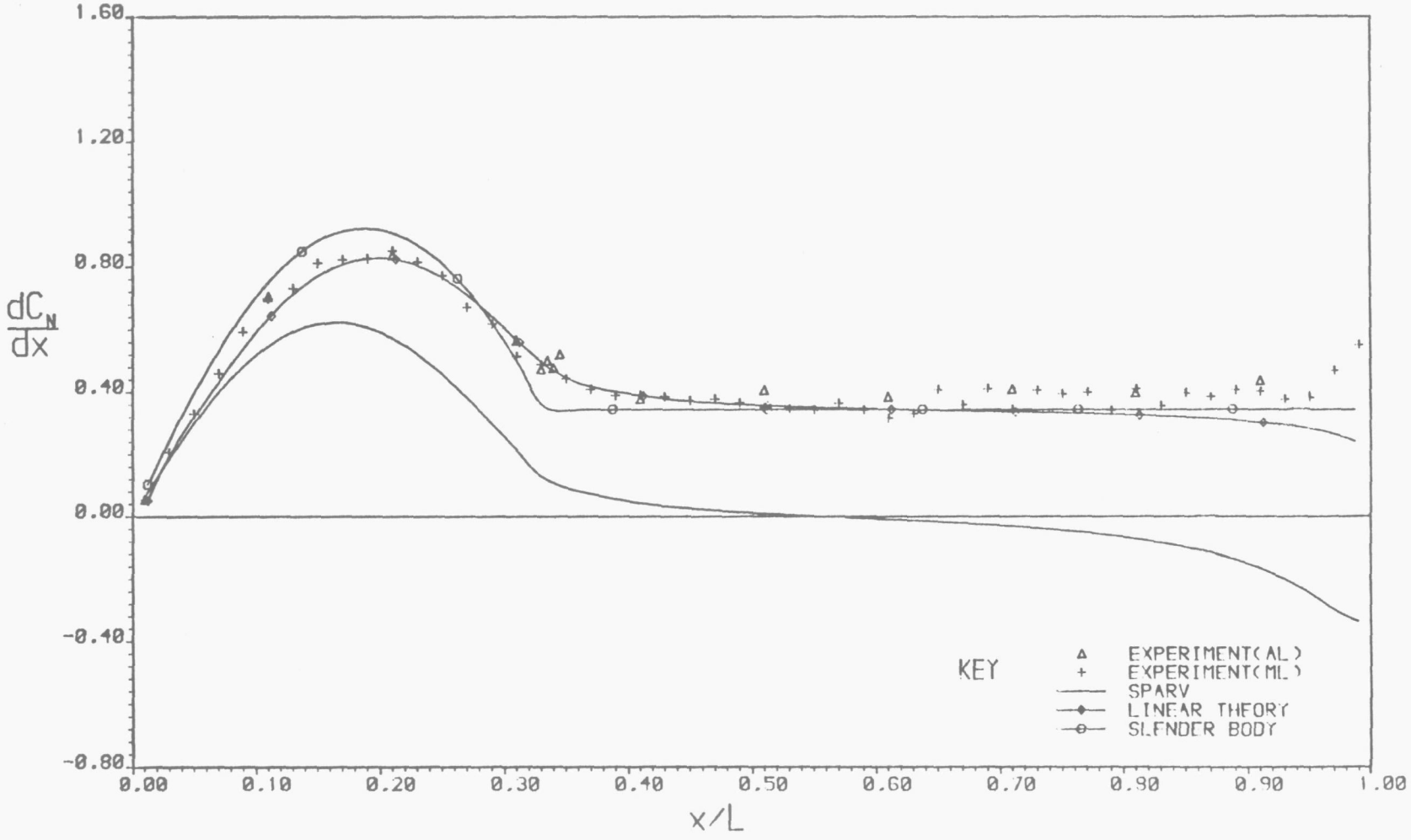

Figure 40. Ogive-cylinder body in curved flow
Comparison of experiment with theory.
Variation of dC_N/dx with x/L. Pitch = 8.0 degrees

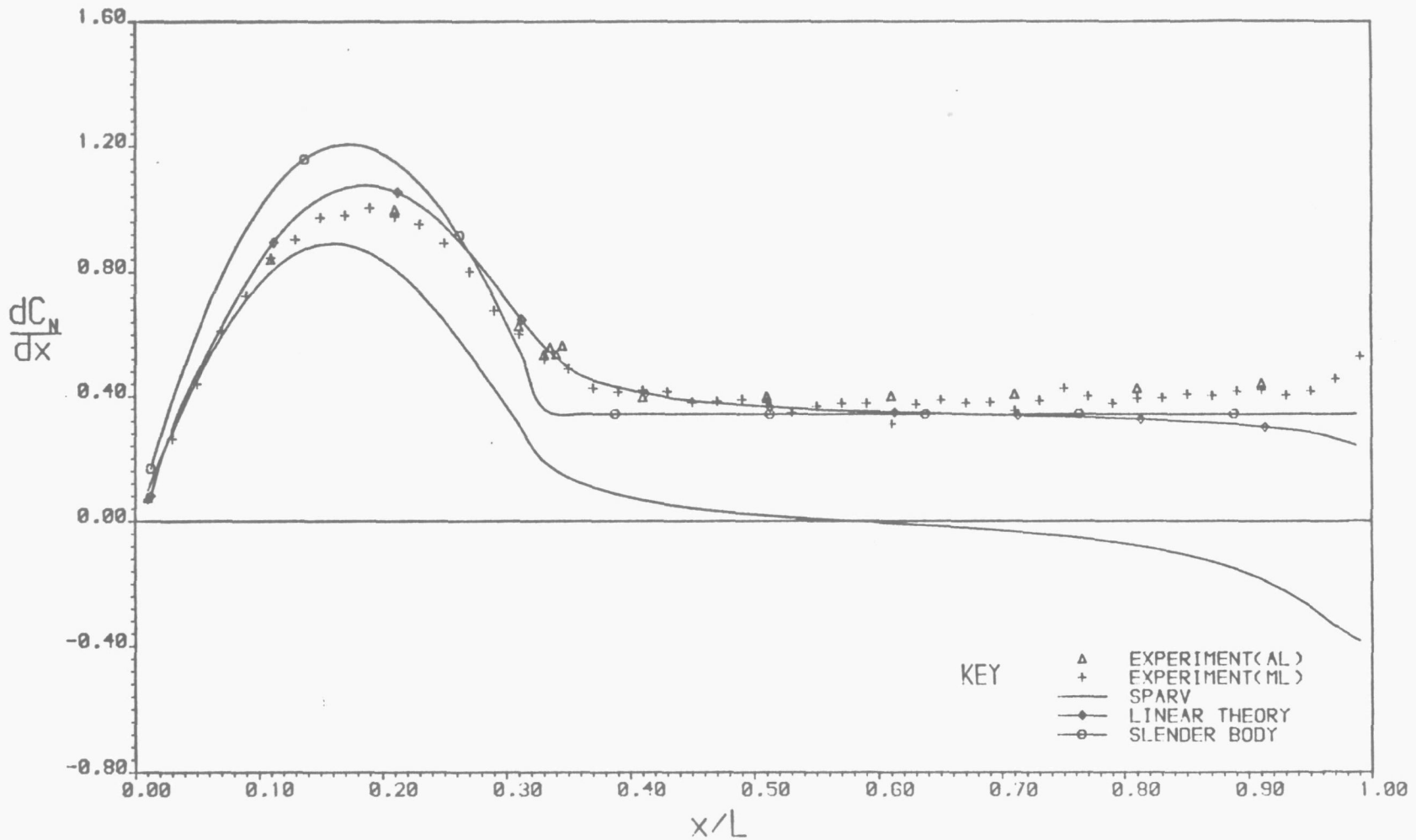

Figure 41. Ogive-cylinder body in curved flow
Comparison of experiment with theory.
Variation of dC_N/dx with x/L. Pitch = 10.0 degrees

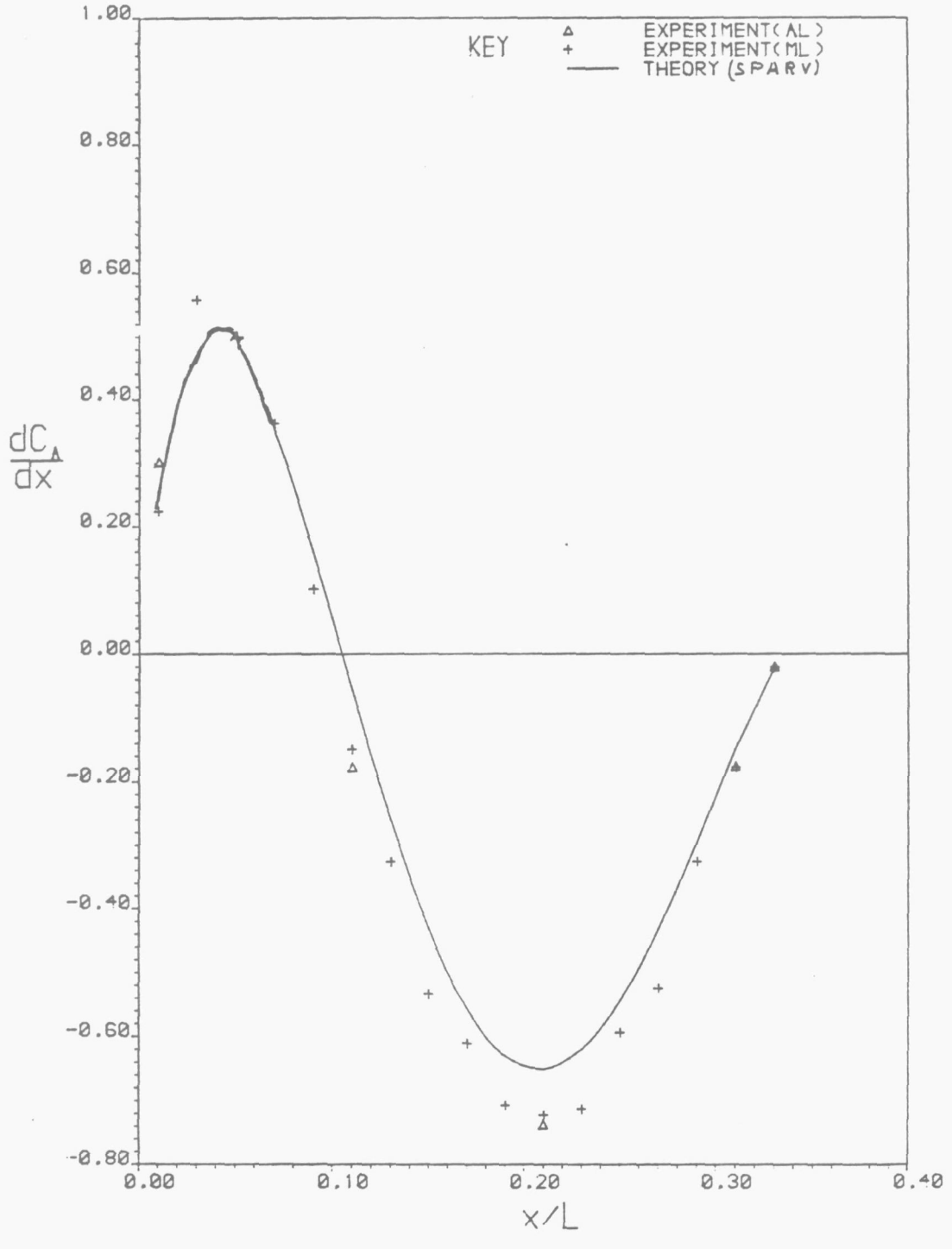

Figure 42. Variation of dC_A/dx with x/L.
Pitch = -8.0 degrees
Comparison of experiment with theory.
Ogive-cylinder body in curved flow

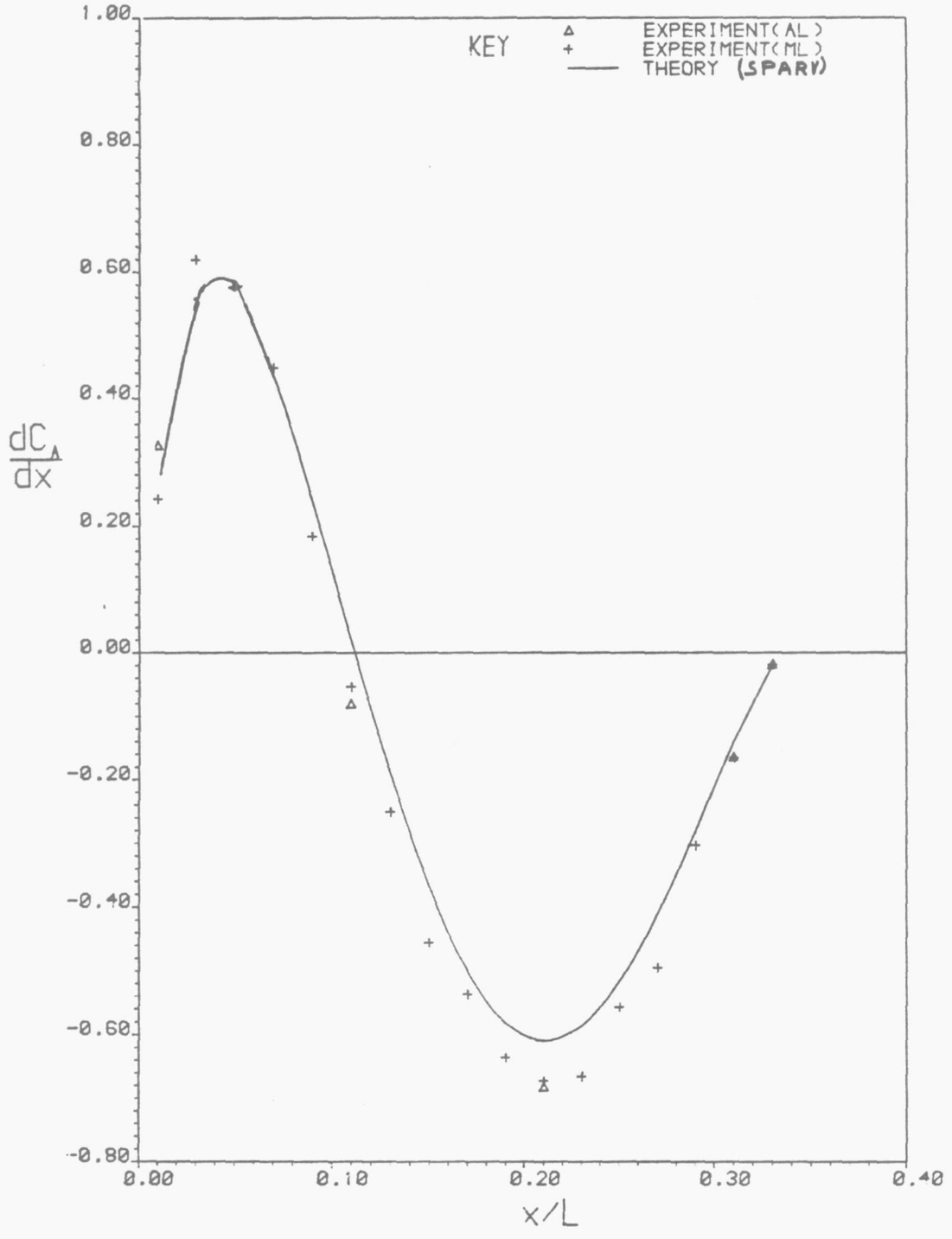

Figure 43. Variation of dC_A/dx with x/L.
Pitch = -6.0 degrees
Comparison of experiment with theory.
Ogive-cylinder body in curved flow

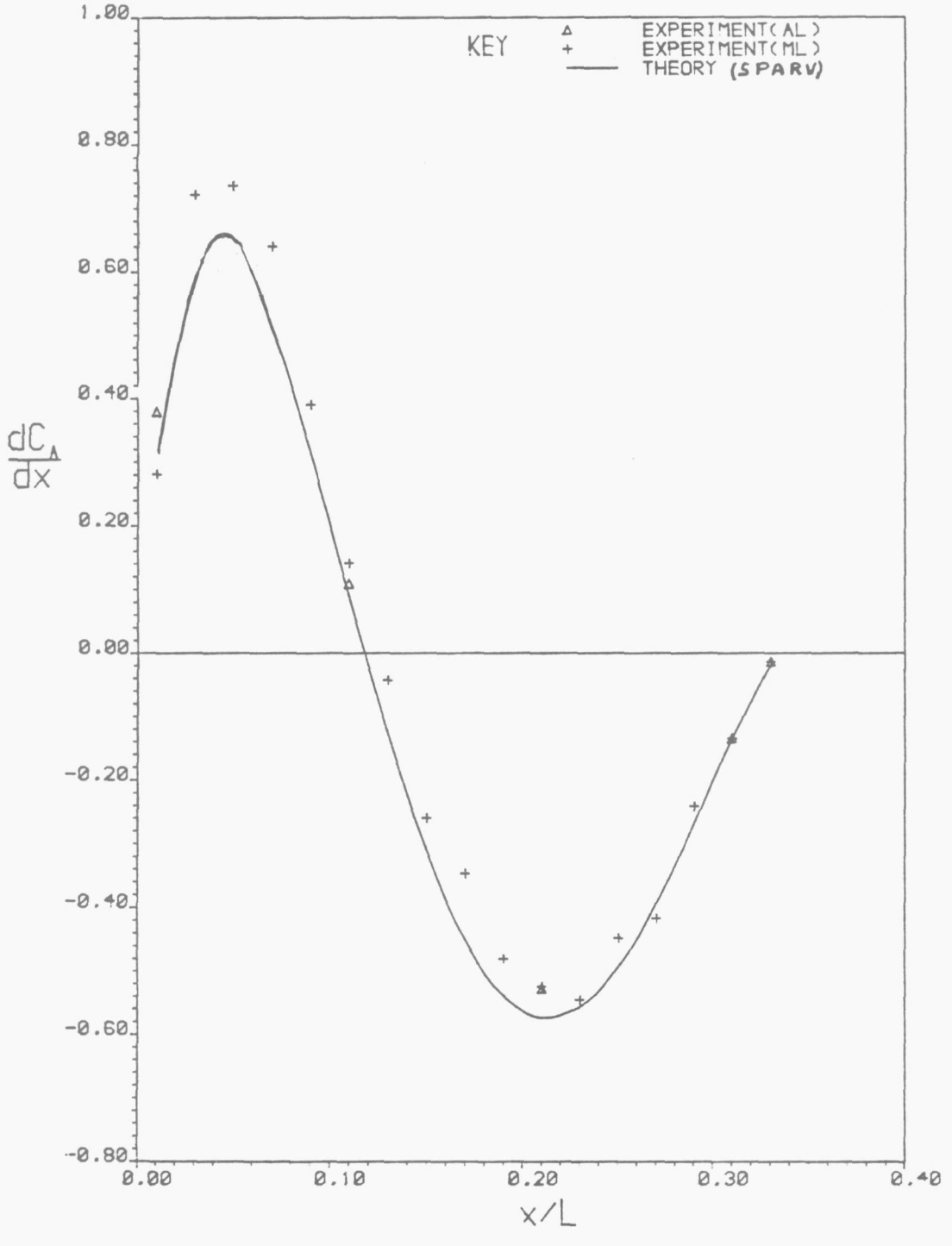

Figure 44. Variation of dC_A/dx with x/L.
Pitch = -4.0 degrees
Comparison of experiment with theory.
Ogive-cylinder body in curved flow

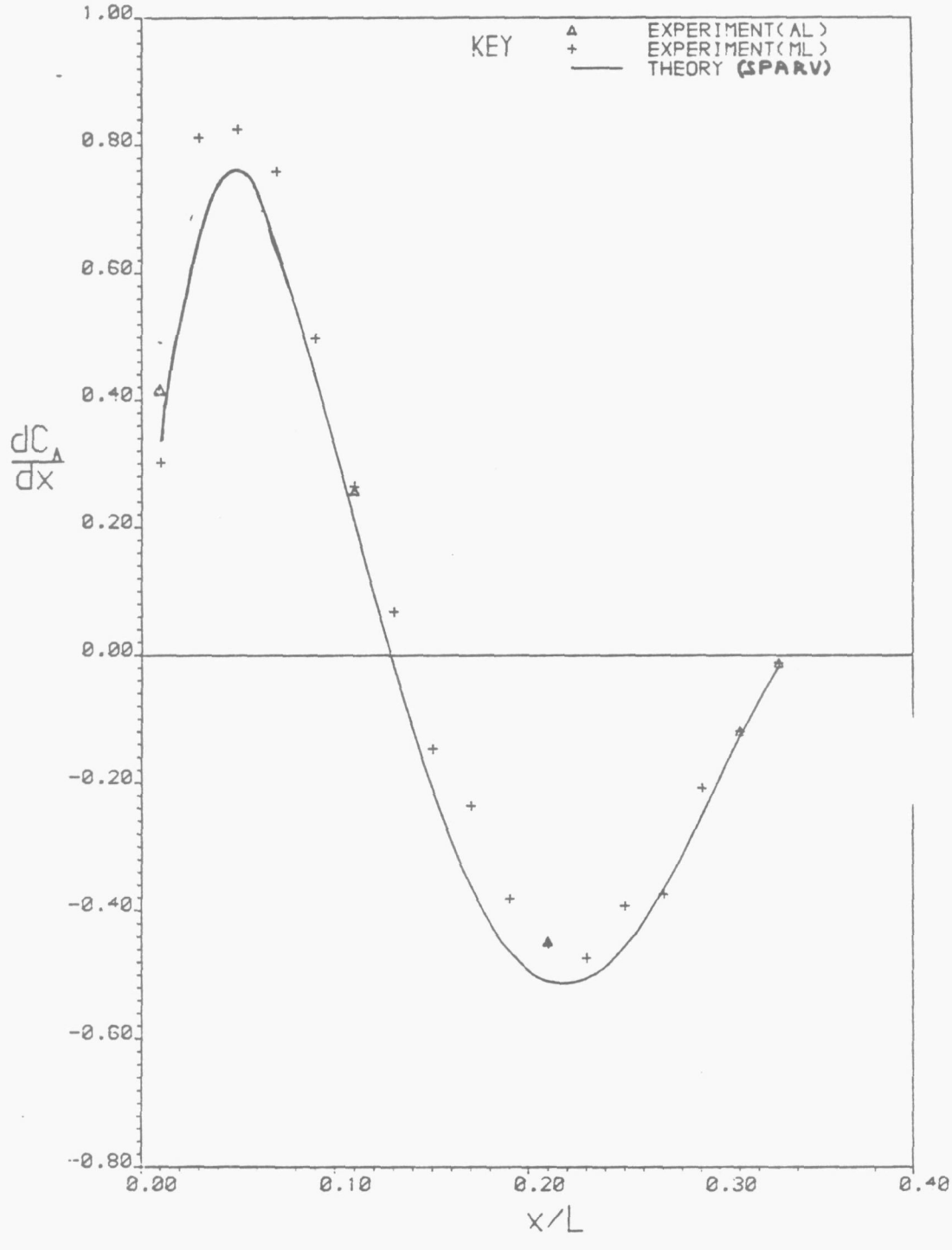

Figure 45. Variation of dC_{A}/dx with x/L.
Pitch = 1.0 degrees
Comparison of experiment with theory.
Ogive-cylinder body in curved flow

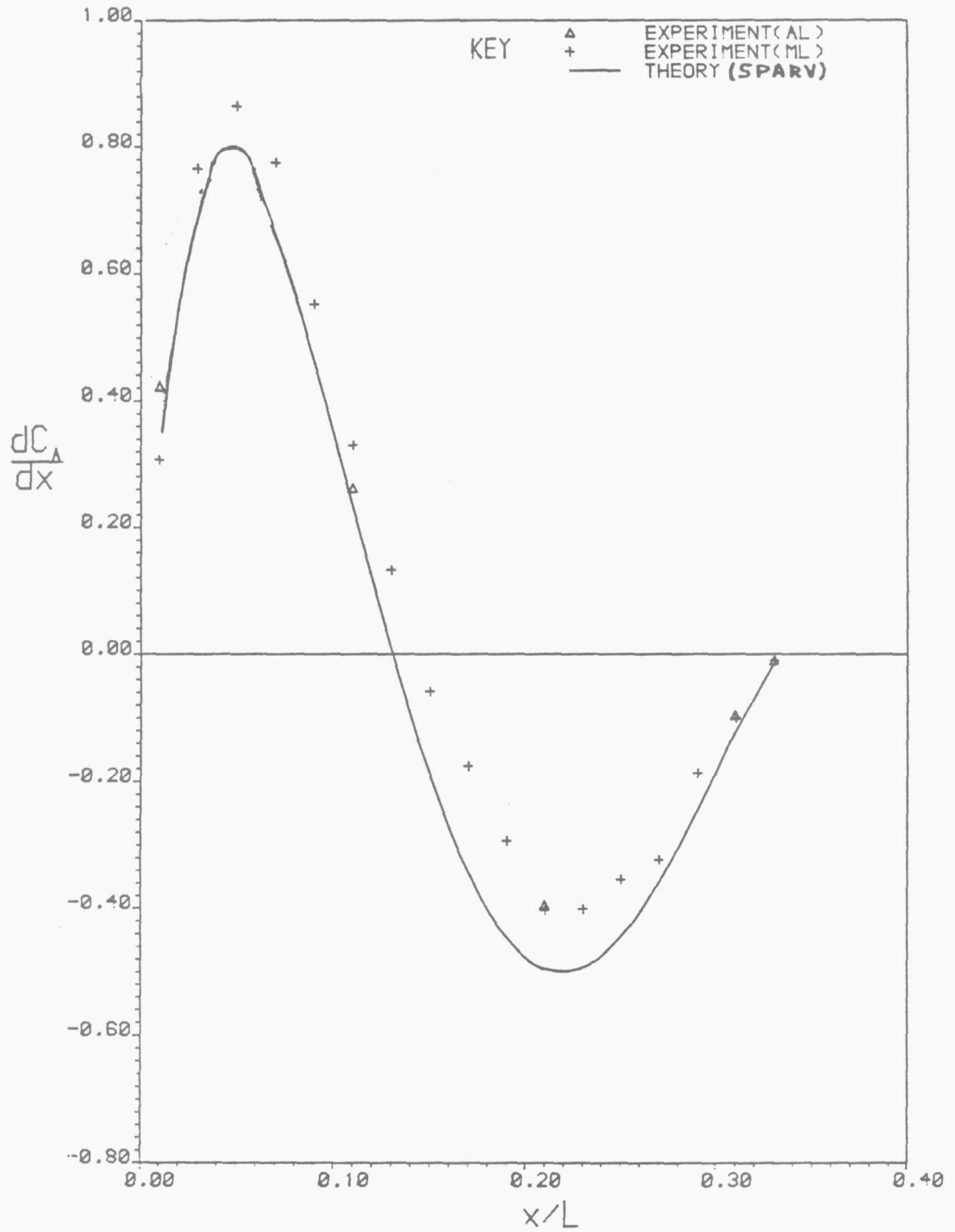

Figure 46. Variation of dC_A/dx with x/L.
Pitch = 3.0 degrees
Comparison of experiment with theory.
Ogive-cylinder body in curved flow

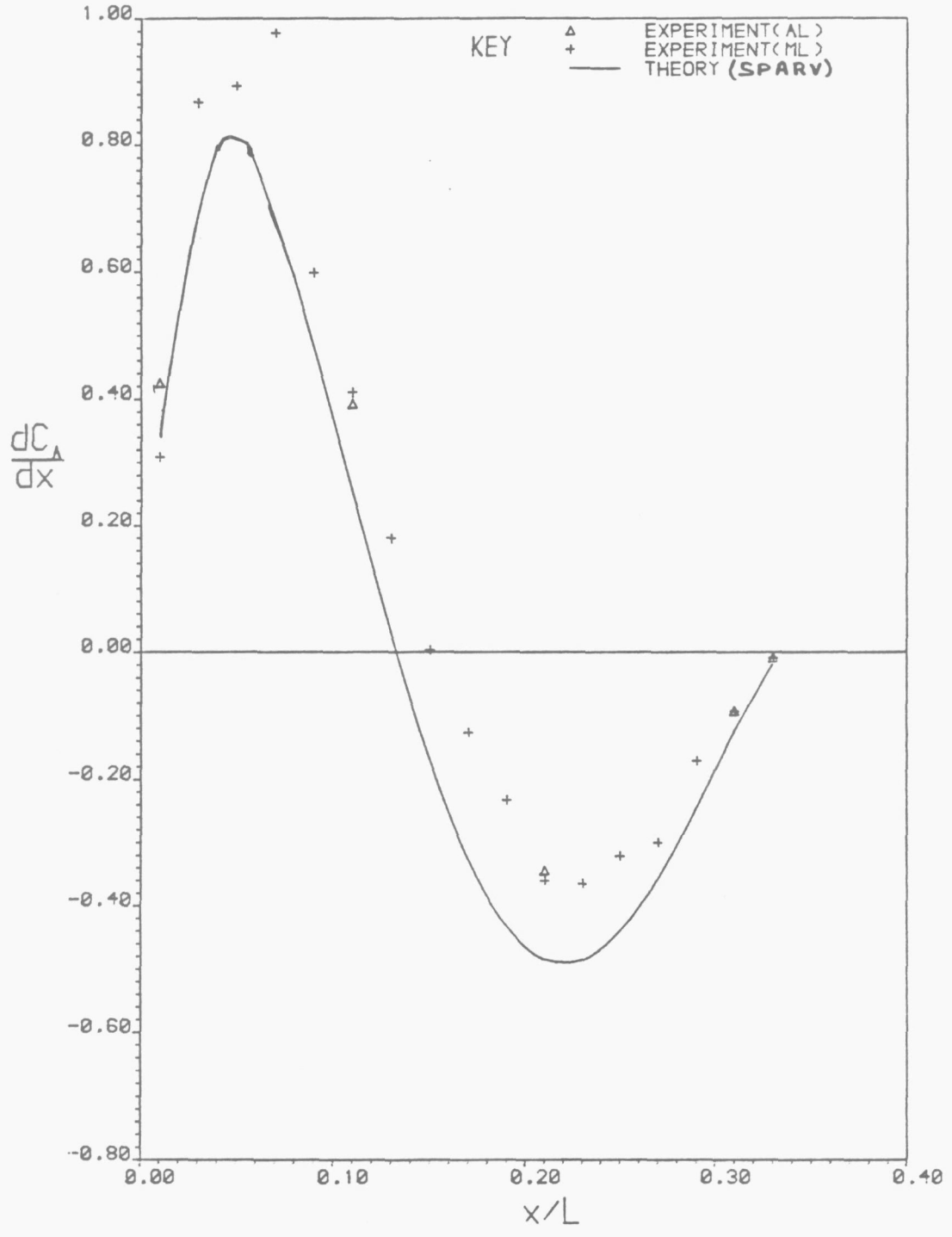

Figure 47. Variation of dC_{A}/dx with x/L.
Pitch = 5.0 degrees
Comparison of experiment with theory.
Ogive-cylinder body in curved flow

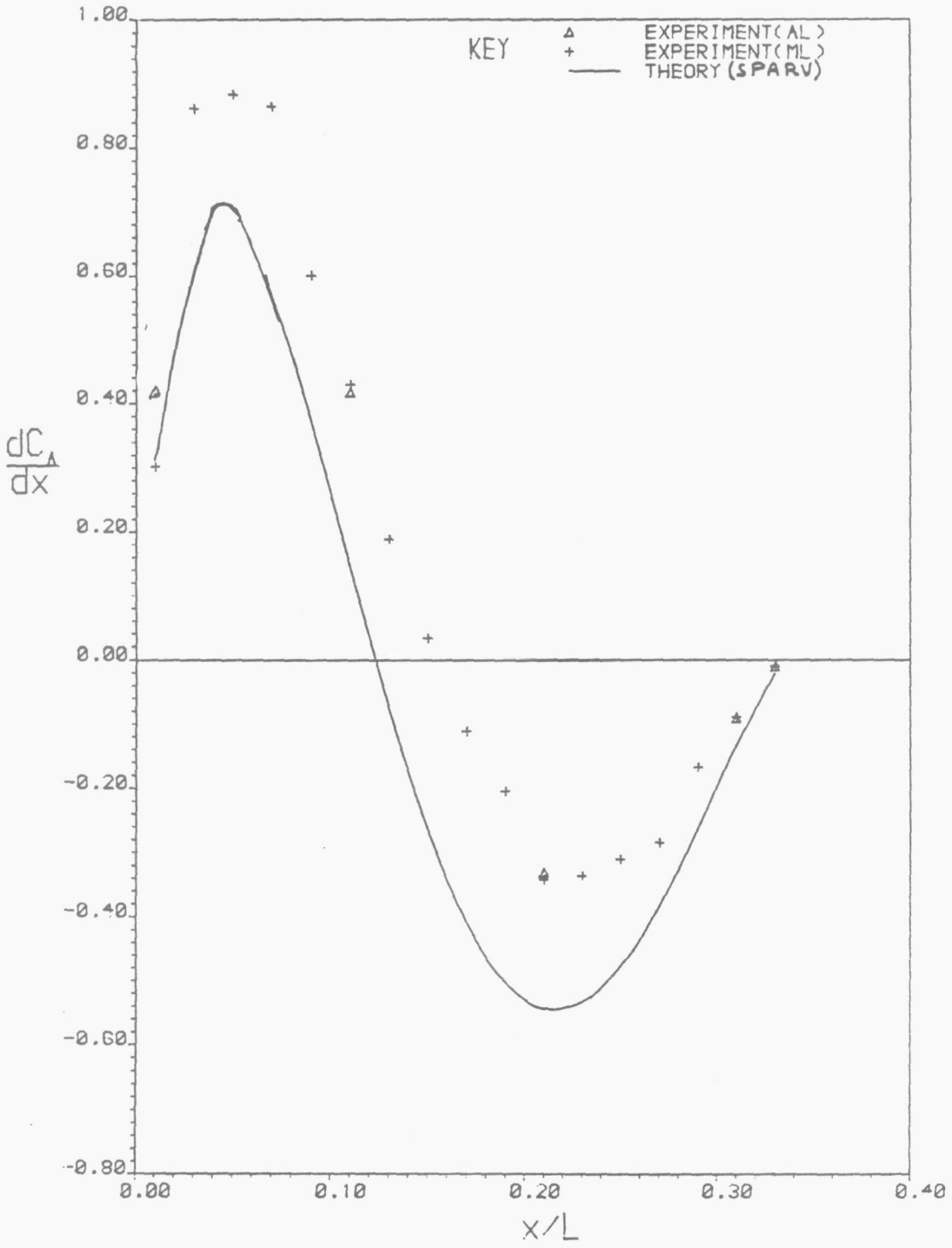

Figure 48. Variation of dC_A/dx with x/L.
Pitch = 7.0 degrees
Comparison of experiment with theory.
Ogive-cylinder body in curved flow

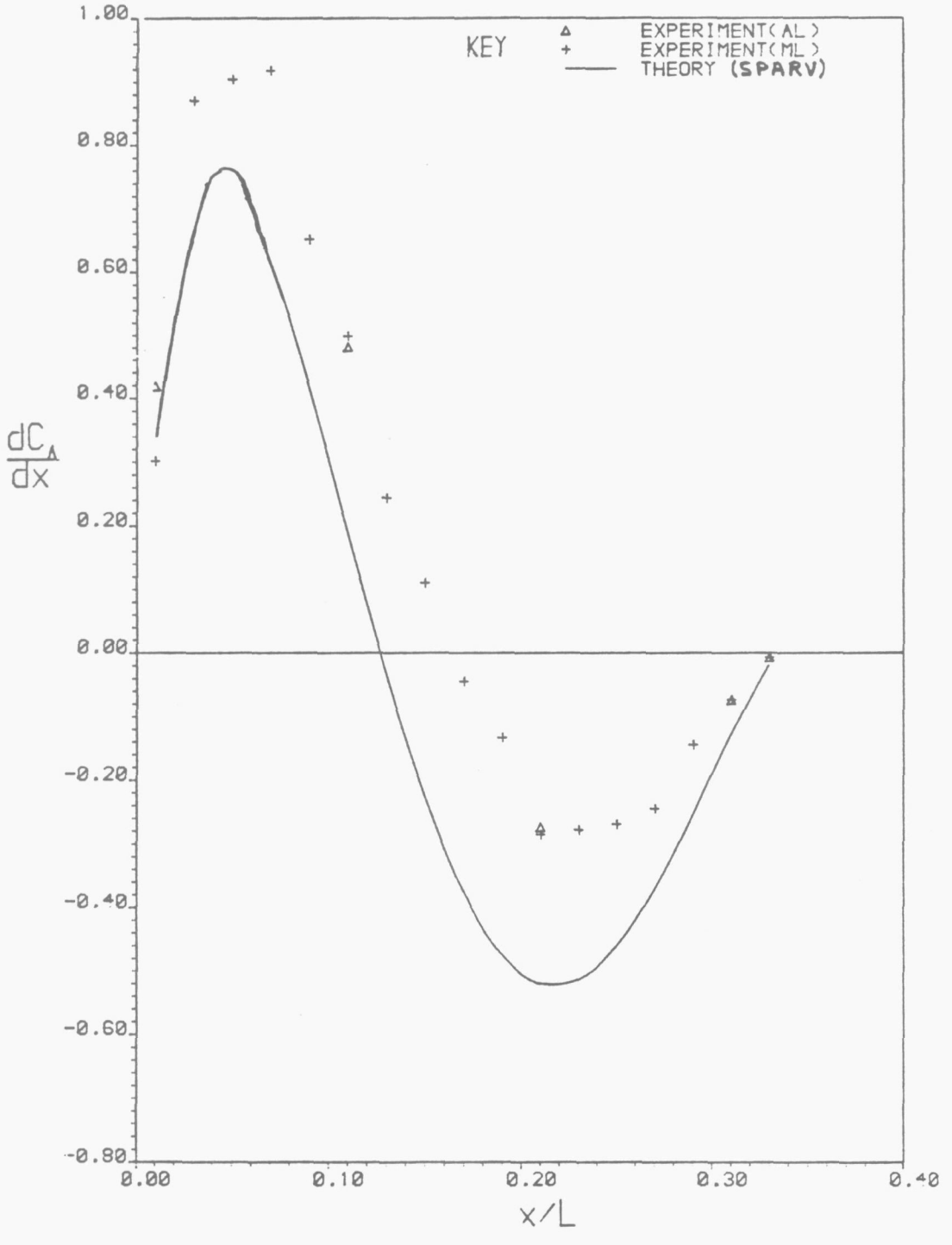

Figure 49. Variation of dC_{A}/dx with x/L.
Pitch = 8.0 degrees
Comparison of experiment with theory.
Ogive-cylinder body in curved flow

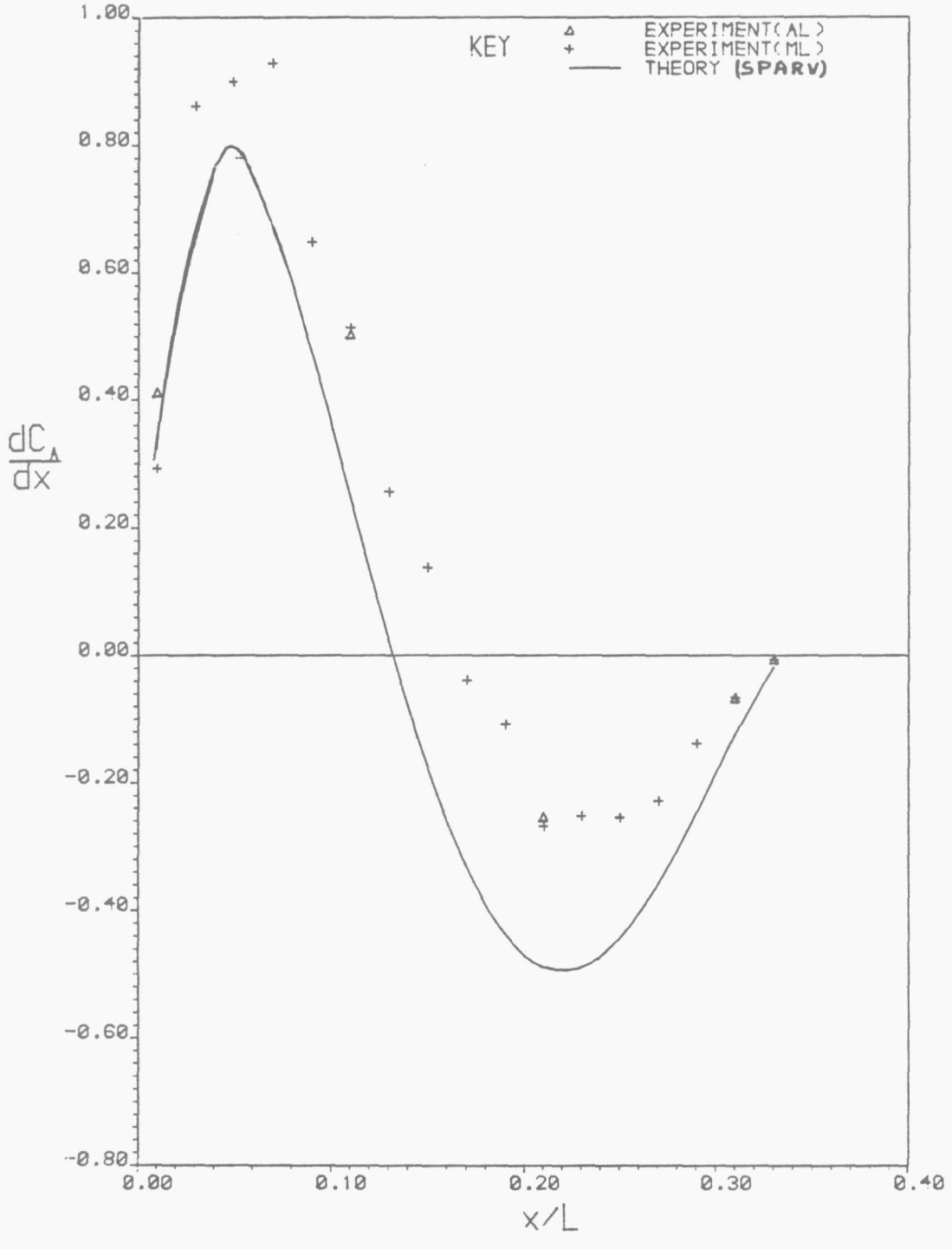

Figure 50. Variation of dC_A/dx with x/L.
Pitch = 10.0 degrees
Comparison of experiment with theory.
Ogive-cylinder body in curved flow

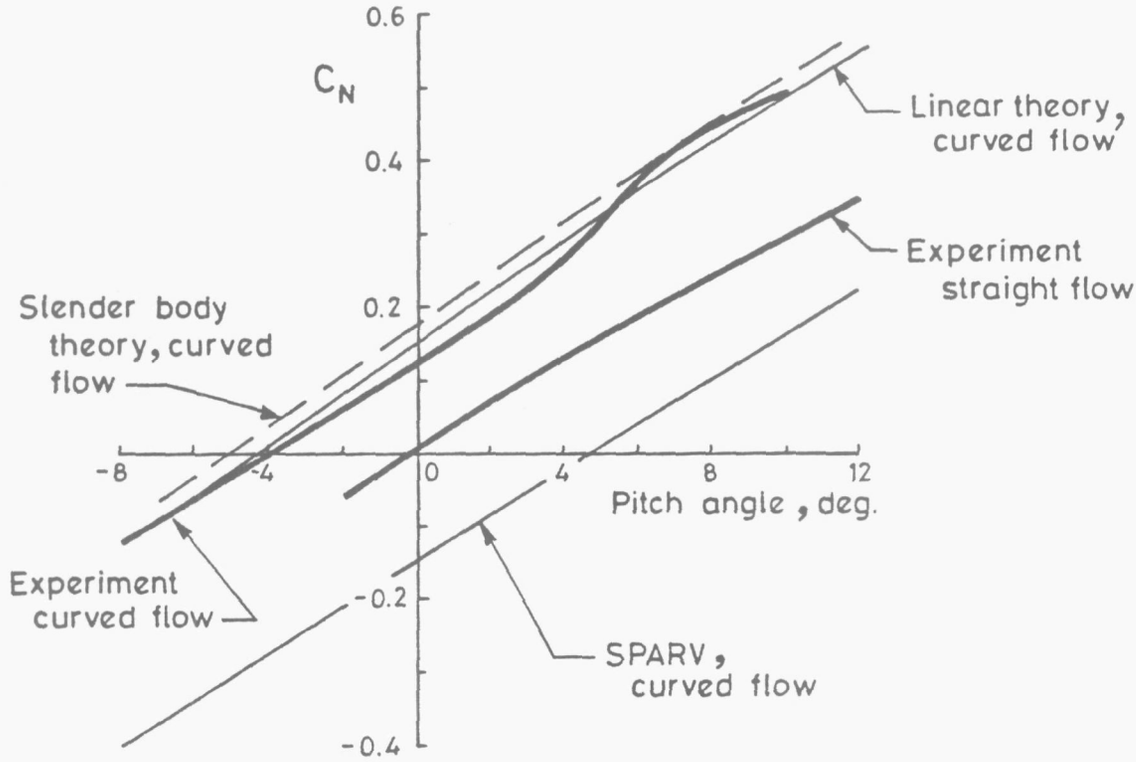

Figure 51. Variation of C_N with adjusted pitch angle.

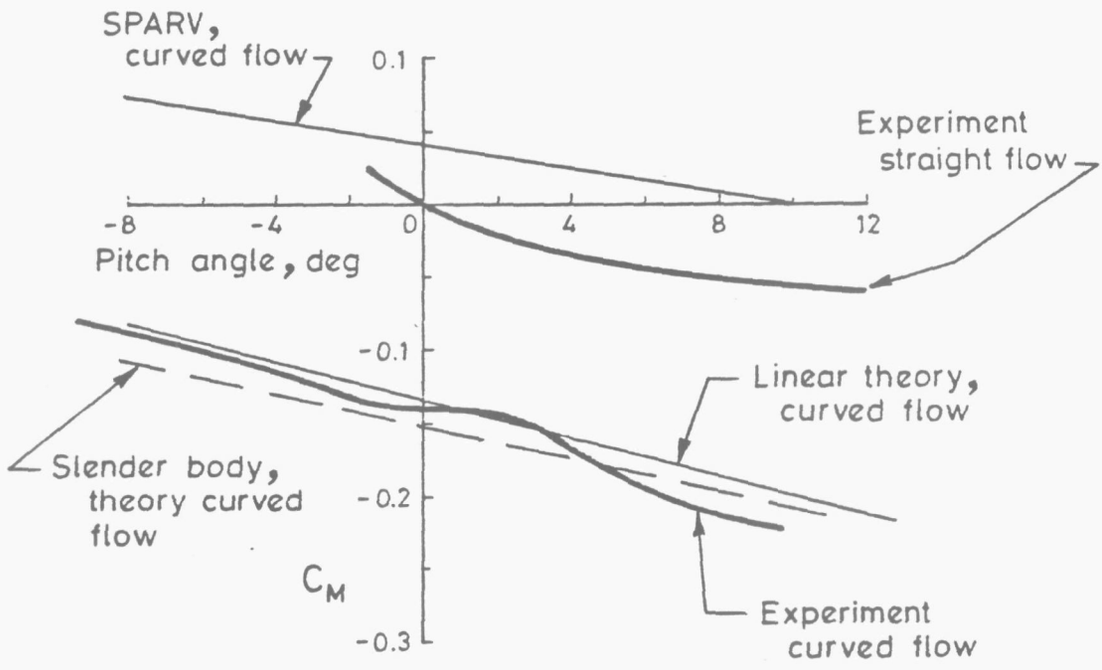

Figure 52. Variation of C_M with adjusted pitch angle.

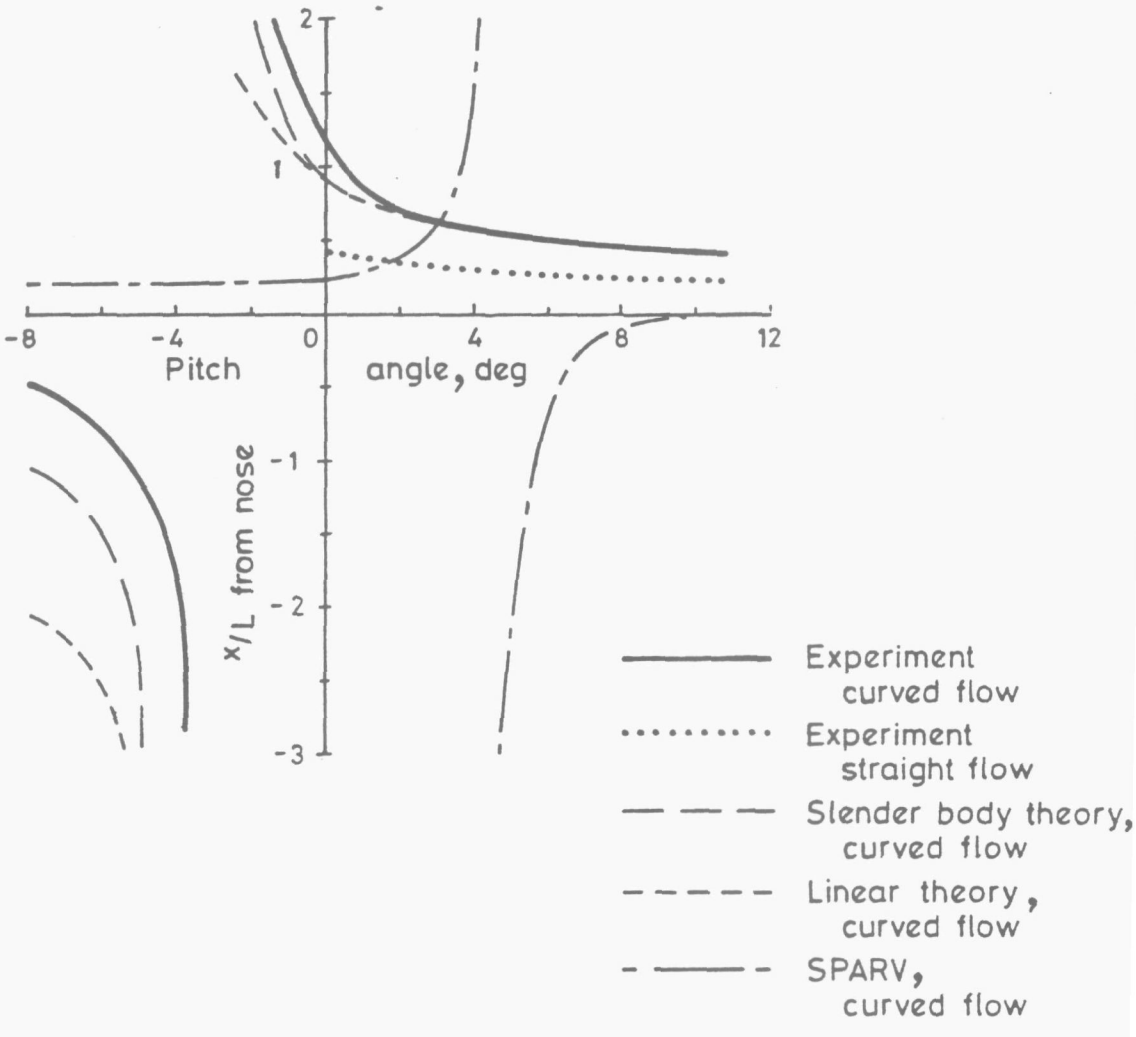

Figure 53. Variation of centre of normal force with adjusted pitch angle.

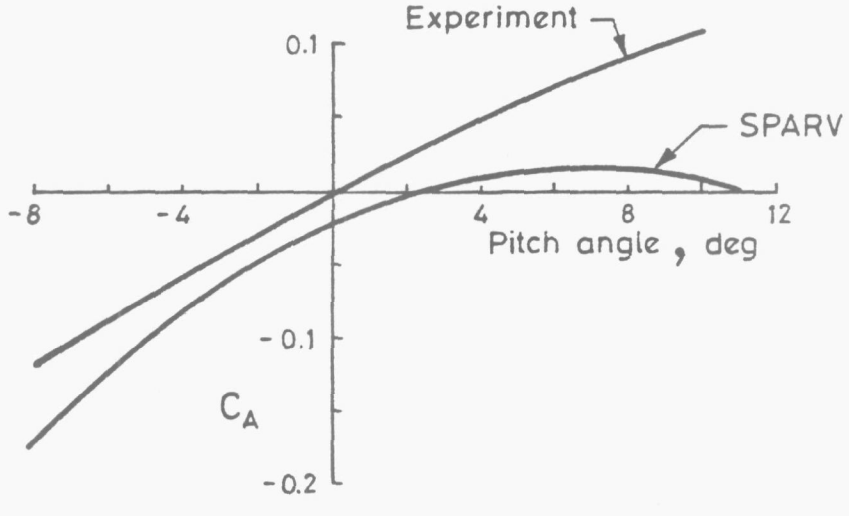

Figure 54. Variation of forebody axial force with pitch angle.